Improving Sensitivities in $0\nu\beta\beta$ Decay Searches by Utilizing PEN as a Structural Scintillating Material

A Dissertation Presented for the

Doctor of Philosophy

Degree

The University of Tennessee, Knoxville

Brennan Theresa Hackett

August 2022

© by Brennan Theresa Hackett, 2022
All Rights Reserved.

To the centuries of female scientists who overcame so much, who participated in research because it was right and because they could make a difference, and in return experienced so much scrutiny, thank you for paving the way for me to have this opportunity, so I could have the privilege of being a researcher and make my own impact on the world.

"Whatever you choose to do, leave tracks. That means don't do it just for yourself. You will want to leave the world a little better for you having lived."

- Ruth Bader Ginsburg

Acknowledgments

Looking back on my journey of completing my dissertation, there are many people I want to thank for their unwavering support.

Yuri Efremenko - Though I did not start this journey with you as my advisor, I am confident in saying I would not have had the success I have had without your consistent support. Your confidence in me has motivated me to be a better researcher, and your kindness to your students has inspired me to be a better person.

Michael Febbraro - I am deeply indebted to the research mentorship I have received from you over the last 4 years. Your creativity and drive to make better science and scientists is something I hope to exemplify in the future. Thank you for taking me under your wing when I didn't have many options and looking out for me.

Christine Nattress - Your candid advice has been a breath of fresh air, helping guide me through my research. Your fearless support of me and your students is truly an inspiration, and I can see how you have directly impacted the next generation of scientist for the better. Thank you for being the kind of mentor I hope to be for others.

ORNL Physics Division - Over the last six years, you all have been there to answer my many questions, help me when I am lost and watched me grow from a confused undergraduate to a confident researcher. Thank you for everything, ORNL Physics Division will always hold a special place in my heart.

Dissertation Writing Group - I truly can say I would not have written as well or as consistently if it hadn't been for my wonderful writing group, meeting up weekly and holding me accountable. Not often does writing a dissertation feel enjoyable, but I can honestly say

with you all it was a blast. Thank you for being there and I am very excited to see us all succeed.

Rushabh Gala - Thank you for answering my many questions and helping me work through my simulations. Your kindness and patience truly had such an impact, and gave me the reassurance that I would make it through what felt like an impossible task.

Matt Green - I am extremely grateful for all of your help and support while working on MaGe and GAT. Thank you for finding time when you were already overbooked, and finding the humor in me sitting outside your office.

Knoxville Friends - Never did I imagine when I moved to Knoxville in 2017, that I would find a second family here. I have truly enjoyed my time with you all and it is bittersweet that life is moving on. Thank you to my weightlifting team for giving me a physical outlet for all the ups and downs. Thank you to my Craft Bastard running crew for providing all the laughs and excellent brews, helping me find the lighter side in life.

Rebecca Toomey - Its hard to believe that it has been 6 years already, and we have found a way to enjoy all of it. Thank you for reading every word of this dissertation, for listening to every presentation, checking every abstract, every paper, listening to my complaints and celebrating my successes. This journey into research would have been lonely and daunting without you by my side. I don't know where I will end up in life, but I can say for certainty my life is better because you were in it. Thank you.

DOE Office of Nuclear Physics - Thank you for funding this project, and providing the resources which allowed for this research to be completed and for me to experience a high level of research.

Finally, I want to express my profound gratitude for my wonderful husband *Quincy Clare-King*, my parents, my sister *Alina Hackett* and all of my extended family. Thank you for the unfailing support and continuous encouragement. This accomplishment would not have been possible without all of you.

"Kind words can be short and easy to speak, but their echoes are truly endless."

- Mother Teresa

Abstract

Neutrinoless double beta decay, $0\nu\beta\beta$ is currently the only experimental test to unambiguously determine the majorana nature of the neutrino. There is a large international effort to measure $0\nu\beta\beta$ decay, with a number of detector technologies being pursued. This dissertation will consider the LEGEND experiment (Large Enriched Germanium Experiment for Neutrinoless $\beta\beta$ Decay), an international effort to measure $0\nu\beta\beta$ decay with ^{76}Ge as both the target isotope and the detecting material.

LEGEND has a 200 kg stage and a 1000 kg stage, each requiring extremely low levels of background radiation at $Q_{\beta\beta}$ ($E = 2.039$ MeV). These ultra low background levels are reached partially by active veto systems such as the large liquid argon (LAr) cryostat, acting as a cryogenic for the ^{76}Ge crystal, a passive volume attenuating gamma-rays from the experimental hall and as an active volume, producing scintillation light at $\lambda = 128$ nm. This dissertation will look to further support the LAr active veto system by investigating the material poly(ethylene 2,6 -naphthalate) (PEN).

For PEN to be used as an active material in LEGEND, it is necessary to understand its radioactivity, its optical properties and its radioluminescent properties. In this dissertation I detail the measurements I led to determine the optical attenuation length, surface reflectivity and light response to neutrons.

PEN baseplates were then installed in the LEGEND R&D effort, the post Gerda test (PGT). The PGT included 18 kg of ^{76}Ge crystals, with 40% PEN baseplates, and 60% silicon baseplates. A description of data collected from the PGT is included, and how the detectors performed with PEN versus silicon baseplates. Using simulations of the PGT, it was possible

to place limits of ^{232}Th contamination in the PEN baseplates as well as predict the improved veto efficiency with the active PEN material versus the passive silicon material.

This dissertation will evaluate PEN as a scintillating material for structural components in the $0\nu\beta\beta$ decay experiment, LEGEND by evaluating the PGT and compare simulations to experimental results. This comparison will provide insight on how PEN components can impact veto efficiency and further suppress background for future $0\nu\beta\beta$ experiments.

Table of Contents

1 Introduction **1**

2 Theory **6**

2.1 The Neutrino 6

2.1.1 Neutrino Flavor 7

2.1.2 Neutrino Oscillations 8

2.1.3 Determining the Neutrino's Mass 13

2.1.4 The Nature of the Neutrino and the Seesaw Mechanism 14

2.2 Double Beta Decay 17

2.3 $0\nu\beta\beta$ and its Implications 20

2.4 Measuring $0\nu\beta\beta$ 22

2.4.1 International Effort to Measure $0\nu\beta\beta$ 23

3 The LEGEND Experiment **27**

3.1 $0\nu\beta\beta$ Experiments Using ^{76}Ge 27

3.2 Overview of the LEGEND Experiment 30

3.2.1 LEGEND-200 30

3.2.2 LEGEND-1000 32

3.3 Achieving a Quasi-Background-Free Measurement 35

3.3.1 Sources of Background Radiation in LEGEND 35

3.3.2 Active veto System in LEGEND 38

4 PEN as a Low Background Material **42**
4.1 Poly(ethylene 2,6-naphthalte) . . . 42
4.1.1 Scintillation Characteristics of PEN . . . 44
4.1.2 Wavelength Shifting VUV Light with PEN . . . 45
4.2 Production of PEN Components . . . 47
4.2.1 Radio-Clean Procedure . . . 49
4.3 Radiopurity of PEN Components . . . 50
4.3.1 HPGe Counting . . . 51
4.3.2 ICP-MS Measurement . . . 51
4.3.3 Radon Emanation . . . 55
4.4 Synthesis of PEN . . . 55
4.4.1 Experimental Methods . . . 57
4.4.2 Reagents . . . 62
4.4.3 Experimental Procedure . . . 62
4.4.4 Properties of Synthesized PEN . . . 63
4.4.5 Radiopurity of PEN Reagents . . . 66
4.4.6 Conclusions of Synthesized PEN . . . 68

5 Studies of PEN as an Active Veto Material **70**
5.1 Structural Properties of PEN . . . 70
5.2 Optical Properties of PEN . . . 73
5.2.1 Surface Reflectivity . . . 73
5.2.2 Attenuation Length Measurements . . . 74
5.3 Wavelength Shifting Properties of PEN . . . 80
5.3.1 WLS Effects of Cleaning PEN Components . . . 83
5.4 Light Response of PEN to Neutrons . . . 85
5.4.1 PEN scintillation detector . . . 88
5.4.2 Experimental Method . . . 88
5.4.3 Error Analysis . . . 100

5.4.4 Results of Light Response 102

6 PEN in the Post Gerda Test **106**

6.1 The Post Gerda Test (PGT) 106

6.1.1 Geometry of the PGT 107

6.1.2 Preparation of PEN Plates for the PGT 107

6.2 Experimental and Simulated Data for the PGT 114

6.2.1 Simulated Data of the PGT 114

6.2.2 Experimental Data for the PGT 120

6.2.3 Placing ^{232}Th Limits in PEN Baseplates 124

6.2.4 Predicted Veto Efficiency with PEN Baseplates 129

7 Conclusion **131**

Bibliography **135**

Appendix **145**

A Details of PEN Machining for PGT 146

Vita **147**

List of Tables

2.1 Table of leading $0\nu\beta\beta$ decay experiments internationally. 24

4.1 The radiopurity results achieved for PEN material using HPGe counting at GeMPI and at OBELIX. The limits shown here are given with 90% confidence level. 52

4.2 The radiopurity results achieved for PEN material using ICP-MS for ^{232}Th and ^{238}U. The absolute detection limits were calculated as three times the standard deviation of the process blanks and the instrumental precision for a given measurement as the error. 54

4.3 The specific activity of different radio-impurities in PEN reagents. The ^{79}Br content is listed in nanograms per gram, providing an example of a measurable organic and inorganic salt that was removed from the DMN sample. The sample brackets describe whether the material is stock material or has been recrystallized in solvent. The radio-impurity brackets describe the method of measuring the sample. 67

5.1 This table shows the tensile strength, σ_{el} and the Young's modulus, E, for structural materials used in the LEGEND experiment. 72

5.2 Table of fraction values, determined by observing the transparency of a cuvette filled with PEN and ethanol versus a cuvette filled with only ethanol, using a Geant4 optical simulation. 81

6.1 Simulated detector efficiencies for $E_\gamma = 2.614$ MeV simulated using the MaGe and GAT software packages. 122
6.2 Background measurements conducted at the PGT were used to place limits on the content of the ^{232}Th levels inside the PEN baseplates. 128
6.3 Simulation of artificially contaminated baseplates in string 4, S4, to predict the veto efficiency of PEN baseplates in a PGT geometry. 130

List of Figures

1.1 Sensitivity of $0\nu\beta\beta$ decay in ^{76}Ge. 3

2.1 Diagram of the standard model. 9
2.2 Two possible mass hierarchy schemes for the neutrino. 12
2.3 Level scheme for ^{76}Ge by $\beta\beta$ decay. 19
2.4 Feynman diagram for $\beta\beta$ decay. 21
2.5 Distributions for $m_{\beta\beta}$ for the two neutrino mass hierarchies. 26

3.1 Diagram of GERDA experiment. 29
3.2 Diagram of MAJORANA DEMONSTRATOR experiment. 29
3.3 Diagram of LEGEND-200 experiment. 31
3.4 Baseline design for LEGEND-1000 experiment. 33
3.5 Design for detector unit for LEGEND-1000. 34
3.6 Decay chains for ^{238}U, ^{235}U and ^{232}Th. 36
3.7 Heat map for LAr in GERDA test setup LArGe. 39
3.8 Spectrum of events in atmospheric argon and underground argon. 39

4.1 Skeletal formula of PET and PEN. 43
4.2 Absorption spectrum of DMN in ethanol. 46
4.3 Ratio of wavelength shifted light from TPB and PEN. 46
4.4 Image of injection molding machine with PEN plate inside. 48
4.5 Images of synthesized PEN and PEN reaction setup. 56
4.6 Image of commercial PEN molded into caps. 60

4.7 Image of synthesized PEN samples with varying levels of CHDM. 61
4.8 Image of reaction flask with synthesized PEN inside. 64
4.9 Image of synthesized PEN sample. 65
4.10 Spectrum of light yield of PEN samples. 65
4.11 Thermogram of commercial and synthesized PEN. 67

5.1 Image of reflectivity tool used to measure σ_α. 75
5.2 Diagram of reflectivity tool. 75
5.3 Plot of reflectivity measurements. 76
5.4 Diagram of dual beam Shimadzu UV-2700i UV-Vis Spectrophotometer. . . 78
5.5 Image of PEN pieces and jog for absorption measurements. 79
5.6 Rendering of optical simulation for absorption measurements. 79
5.7 Image of PEN tile A. 81
5.8 Image of PEN tile B. 81
5.9 Spectrum of attenuation length for different samples. 82
5.10 Spectrum of excitation and emission for wavelength shifting measurements. 84
5.11 Spectrum of relative intensity for wavelength shifted light. 84
5.12 Spectrum of average light pulses in PEN for proton and electron recoils. . . . 87
5.13 Image of PEN component used in radioluminescence measurements. 89
5.14 Spectrum of ^{137}Cs source with $E_\gamma = 0.661 MeV$ on PEN. 91
5.15 Spectrum of energy resolution of PEN detector. 91
5.16 Schematic of ^{252}Cf fission chamber. 94
5.17 Spectrum of time of flight with ^{252}Cf chamber. 94
5.18 Spectrum of PSD verse light for PEN detector. 96
5.19 Spectrum of data and simulation reconstruction of DD neutron measurement. 98
5.20 Diagram and image of University of Notre Dame experimental setup. 99
5.21 [Spectrum of energy depostion from neutrons, $E_n = 1.724$ MeV, in data and simulation. 101
5.22 Spectrum of PSD gates for PEN detector. 101

5.23 Spectrum of quenching factors for different neutron sources. 103
5.24 Spectrum of light response of PEN fit with Birk's function. 104
5.25 Spectrum of energy deposition of neutrons, E_n = 4.906 MeV, both data and simulation reconstruction. 105

6.1 Image of post Gerda test geometry. 108
6.2 Schematic of post Gerda test setup. 109
6.3 Schematic of jig used to machine PEN baseplates. 111
6.4 Images of washing components for machining PEN baseplates. 111
6.5 Image of PEN baseplates being CNC machined. 113
6.6 Images of PEN baseplates after machining. 113
6.7 Image of PEN baseplate rendering in MaGe. 116
6.8 Rendering of PGT geometry in MaGe. 116
6.9 Spectrum of light propagation probability map for PGT. 118
6.10 Spectrum of light propagation probability map for PEN baseplate in PGT. . 118
6.11 Simulated data of detector S4.2 in the PGT. 121
6.12 Simulated data of detector S4.3 in the PGT. 121
6.13 Simulated data of detector S4.4 in the PGT. 122
6.14 Spectra of baseline studies for PGT. 123
6.15 Spectrum of detector S4.2 in the PGT. 125
6.16 Spectrum of detector S4.3 in the PGT. 125
6.17 Spectrum of detector S4.4 in the PGT. 126

Nomenclature

E_γ Energy of gamma-ray

$m_{\beta\beta}$ Effective neutrino mass from $0\nu\beta\beta$ decay

$0\nu\beta\beta$ neutrinoless double beta decay

$Q_{\beta\beta}$ Q value for the double beta decay in ^{76}Ge

$T_{1/2}^{0\nu\beta\beta}$ Half life for neutrinoless double beta decay

GAT Germanium Analysis Toolkit

ICPC Inverted Coaxial Point Contact detector

LAr liquid argon

LEGEND large enriched germanium experiment for neutrinoless double beta decay

LNGS Laboratori Nazionali del Gran Sasso

MaGe Simulation package developed by the MAJORANA and Gerda collaborations

PEN poly(ethylene 2,6 naphthalate)

PGT post Gerda Test

PMT photo-multiplier tube

PPC p-type point contact detector

PSD pulse shape discrimination

SiPM silicon photo-multiplier

TPB tetra-phenyl butadiene

Chapter 1

Introduction

It is said that yesterday's discovery is today's calibration, and tomorrow's background. This reality of experimental particle physics is motivation to continually improve detection mechanisms, addressing problems before they become realities. Low-background physics experiments continue to push the boundaries of what is known of the universe. To obtain data from rare interactions, one must build larger experiments with a larger sensitive mass and/or remove background interactions from clouding the data.

It is difficult to conceive just how rare some interactions are in low-background physics experiments. An example is the search for WIMPs, or Weakly Interacting Massive Particles. WIMPs are theorized dark matter particles that only interact via the weak force with matter[1]. The XENON1t experiment is a liquid xenon-based experiment that has not seen any evidence of WIMP interactions with 0.83-tonne year exposure[2]. However, as the detector is so quiet, it is sensitive to other incredibly rare interactions. One example was the first observation of two-neutrino double electron capture in ^{124}Xe with XENON1T[3]. This process occurs when two protons in a nucleus simultaneously absorb two electrons from an atomic shell and convert into two neutrons, resulting in the emission of two electron neutrinos (ν_e). This capture has the longest ever directly measured half-life of $T_{1/2}^{2\nu EC} = 1.8 \pm 0.5_{stat} \pm 0.1_{sys}) \times 10^{22}$ years[3], which is 12 orders of magnitude longer than the age of the universe. This means that if the age of the universe was equivalent to one

grain of rice, this half life is equivalent to 20 megatons of rice. This incredible measurement is still far from the sensitivities needed to measure the pursued WIMPs.

Another rare interaction that is being pursued in low background physics is neutrinoless double beta decay or $0\nu\beta\beta$. This decay has far reaching implications for the understanding of how the universe was formed and the fundamental properties of the neutrino. However, the limits for the half lives of this decay in the permissible isotopes is incredibly long. One isotope where $0\nu\beta\beta$ is theorized to occur is in ^{76}Ge . The current limit on the $0\nu\beta\beta$ decay half life in ^{76}Ge is $T_{1/2}^{0\nu\beta\beta} > 1.8 \times 10^{26}$ years[4]. As the next generation of experiments attempts to measure this decay, it has been demonstrated how a small number of counts in the measurement's region of interest can have a strong impact on the experiment's sensitivity. This is shown strongly in Fig. 1.1, where less than 1 count in the region of interest per ton of material over ten years will improve the sensitivity by a factor of two. Therefore, in the next generation detector development, ultimately both increased sensitive mass and improved background suppression must be utilized.

One technology being developed to improve background suppression is the use of scintillators as secondary detectors, which can be used in coincidence with the primary detectors to detect and remove background events - these detectors are known as active vetoes. Scintillators as a technology are far from novel, with the first scintillating detector being developed over 100 years ago [5]. However, as physics moves to the next generation of large scale detector systems, scintillators are often relied upon for their scalability, stability, and relatively low cost. Because of their relatively low cost, it is not prohibitively expensive to expand detectors by orders of magnitude. Tonne-scale experiments that use scintillators include solar neutrino searches (SNO [6]), reactor neutrino measurements (KamLAND [7]) and accelerator neutrino experiments (DUNE [8]). Organic scintillating materials in particular can be synthesized in a controlled environment, introducing minimal radio-impurities [9]. Improved radiopurity of the organic scintillators reduces the number of background counts and improves the signal to background ratio.

Scintillators are also used in the search for neutrinoless double beta decay. $0\nu\beta\beta$ decay experiments have used scintillators as both a detection mechanism and as a background

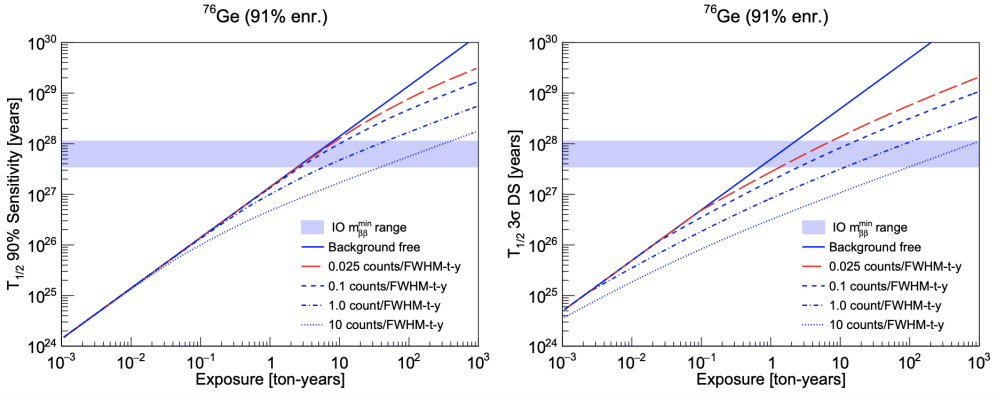


Figure 1.1: Sensitivity for setting a limit (left) or a signal discovery (right) for $0\nu\beta\beta$ decay in ^{76}Ge. From these plots it can be seen how how even small background contributions in the region of interest for $0\nu\beta\beta$ decay can strongly effect the sensitivity of both the $0\nu\beta\beta$ decay half life, $T_{1/2}^{0\nu\beta\beta}$ and the discovery potential [11].

suppression mechanism. For example, EXO is a 200 kg detector that uses scintillation light from liquid ^{136}Xe both as an active veto to suppress background, and as the detection method itself [10]. GERDA, another neutrinoless double beta decay experiment, uses the isotope ^{76}Ge as the detection volume and surrounds the ^{76}Ge detectors with liquid argon (LAr) to both cool the detectors and to provide an active veto via scintillation light [4]. The background suppression, possible by using the scintillating active veto, has allowed GERDA to become the world's first background-free experiment in the search for $0\nu\beta\beta$ decay [4].

Dark matter searches have also utilized the benefits of scintillators in their detectors. For example, XENON1T is a 2000 kg liquid xenon detector located in the Laboratori Nazionali del Gran Sasso in Italy [1], previously described in its pursuit of measuring WIMPs. This large scale time projection chamber was one of the first of its kind to expand to tonne-scale. Interactions of charged particles in the target nucleus xenon produces both scintillation light and ionized electrons. The electrons drift in the electric field towards the liquid-gas interface at the top of the time-projection-chamber (TPC) and are detected via electroluminescence. At this point the electrons produce another proportional scintillation signal. The time difference between the fluorescence and the electroluminescence signal allows for position reconstruction, effectively fiducializing the detector volume and providing further background reduction.

KamLAND-Zen is another example of a large scale detector utilizing scintillators. The detector contains multiple layers to improve background reduction in the experiment. The inner most layer or "Inner Balloon" contains 13 tons of enriched ^{136}Xe-loaded liquid scintillator. The outer ballon surrounds this, with 1 kton of liquid scintillator acting as an active shield. The liquid is also very pure, reducing radio-impurities in the detecting medium furthering the sensitivity. KamLAND-Zen has successfully placed a limit on $0\nu\beta\beta$ decay with $T_{1/2}^{0\nu\beta\beta} > 2.310^{26}$ yrs[12].

Scintillators have been successfully used in large experiments, not only as a detection mechanism, but as a method to identify background signals. In an extrapolated case, if every component in a low background experiment had the capability to identify background

radiation events in and on the surface of the component, then a background-free measurement would be possible.

This dissertation will evaluate the use of PEN as a novel scintillating material for structural components in the low background neutrinoless double beta decay experiment, LEGEND by evaluating the LEGEND R&D effort the PGT. This evaluation will include an extensive characterization of the material and will compare simulation data to experimental results of the PGT. This comparison will provide insight on how PEN components can impact veto efficiency and therefore background suppression for current and future $0\nu\beta\beta$ experiments.

The organization of this thesis is as follows; Chapter 2 will provide an overview on the neutrino and $0\nu\beta\beta$ decay. Chapter 3 will outline the design of the LEGEND experiment and the active veto capabilities of the experiment, including polyethylene naphthalate or PEN. PEN as a low background material will be explained and detailed in Chapter 4 and details of its structural, fluorescent and optical properties will be described in Chapter 5. Finally, Chapter 6 will describe efforts of PEN installation in the LEGEND experiment and Chapter 7 will summarize the efforts and results of this research.

Chapter 2

Theory

Neutrinos are the second most common elementary particle in the universe, following closely behind the photon [13]. Despite their prevalent nature, describing their properties has proven to be a formidable challenge for experimental physics. Understanding the fundamental details of these abundant particles has direct implications on our understanding of the standard model of elementary particles and in particular the evolution of the observable universe.

2.1 The Neutrino

The neutrino was first theorized by Wolfgang Pauli in 1930 to explain the energy spectrum measured in beta decay. Beta decay is a type of radioactive decay, in which a beta particle is emitted from a nucleus, transforming the nuclide into an isobar of that nuclide, or an atom with the same number of nucleons but a different chemical element. The measured energy spectrum of the emitted beta particle was first measured by Lise Meitner and Otto Hahn in 1911, and shown to be continuous [14]. This did not support the previous assumption that the beta decay resulted in the emission of a single particle, but instead as Pauli postulated, resulted in the emission of at least two. This second particle in the decay became known as the neutrino or "the little neutral one" in Italian. The beta decay, as it is currently known, is described in Eq. 2.1.

$$n^0 \rightarrow p^+ + e^- + \overline{\nu_e} \tag{2.1}$$

It wouldn't be until the Cowan-Reines neutrino experiment in 1956 that the existence of the neutrino would be confirmed [15]. This experiment used inverse beta decay to detect electron antineutrinos, $\overline{\nu_e}$ from a nuclear reactor by measuring the gamma-rays emitted as a result of electron-position annihilation and the flash of light in the scintillator from the neutron capture. Inverse beta decay is described in Eq. 2.2.

$$\overline{\nu_e} + p^+ \rightarrow n^0 + e^+ \tag{2.2}$$

After the confirmation of the neutrino's existence, the particle's story evolved to include the puzzle of its flavor, oscillatory behaviour, mass and finally its nature.

2.1.1 Neutrino Flavor

After the detection of the electron antineutrino by Cowan and Reines, Lederman, Schwartz and Steinberger demonstrated the existence of the muon neutrino in 1962 [16]. Using the Alternating Gradient Synchotron at the Brookhaven National Laboratory, energetic protons produced a shower of pi mesons that decayed into muons and neutrinos over 70 ft. The beam passed through a 5,000 ton steel wall, where only neutrinos could reach the other side into a neon-filled spark chamber. The neutrino's interactions with shielding upstream from the detector created muons, which were in turn detected in a spark chamber creating trails that could be photographed, proving their existence.

Finally the third flavor of neutrino measured was the tau neutrino. The tau particle was discovered in 1975 at the Stanford Linear Accelerator, and a corresponding tau neutrino was postulated to exist. It was finally measured in 2000 by the DONUT collaboration [17].

This determination of the neutrino's nature was well reflected by the predictions made by the Standard Model. The Standard Model is a theory describing the fundamental particles of the universe and how they interact with three of the fundamental forces of the

universe (electromagnetic, weak and strong)[18]. A diagram of the fundamental particles and exchange particles is shown in Fig. 2.1. Though the Standard Model has done well to describe the three flavors of the neutrino, it has fallen short on the subject of the neutrino's mass. The revelation that the neutrino oscillates flavor has demonstrated that the neutrino does indeed have mass, and therefore breaks the standard model where the neutrino is massless[11].

2.1.2 Neutrino Oscillations

In the 1960's, the Homestake Experiment was attempting to count electron neutrinos emitted from the sun[19]. The experiment was a large tank of perchloroethylene, which is rich in chlorine. The detection method was to capture neutrinos on ^{37}Cl and then collect and measure ^{37}Ar produced by bubbling He in the tank.

$$\nu_e + {}^{37}Cl \rightarrow {}^{37}Ar + e^- \tag{2.3}$$

To the shock of the collaboration pursuing this measurement, there was a large discrepancy between the number of measured neutrinos and the predicted number. Many questioned the basic understandings of the solar model and blamed the predicted flux on this disagreement [19]. However it would be shown and confirmed in the 2000's by the SNO and Super-Kamiokande experiment that the deficit was in fact due to neutrinos oscillating in lepton flavor [6, 20].

Neutrinos only interact via the weak interaction, neutrinos are produced and often detected as the flavor eigenstate in neutrino experiment [21]. Therefore, charged current weak interactions will transform neutrinos ν_e, ν_μ or ν_τ into e^-, μ^- or τ^- respectively, and their antiparticle forms $\overline{\nu_e}$, $\overline{\nu_\mu}$ or $\overline{\nu_\tau}$ into e^+, μ^+ or τ^+ respectively. Neutrino oscillations are a quantum physical phenomenon where a neutrino's flavor changes spontaneously into another flavor, analogous to quark flavor oscillations. As there are three flavors, there are three kinds of flavor oscillations. The theory to quantitatively articulate neutrino oscillations

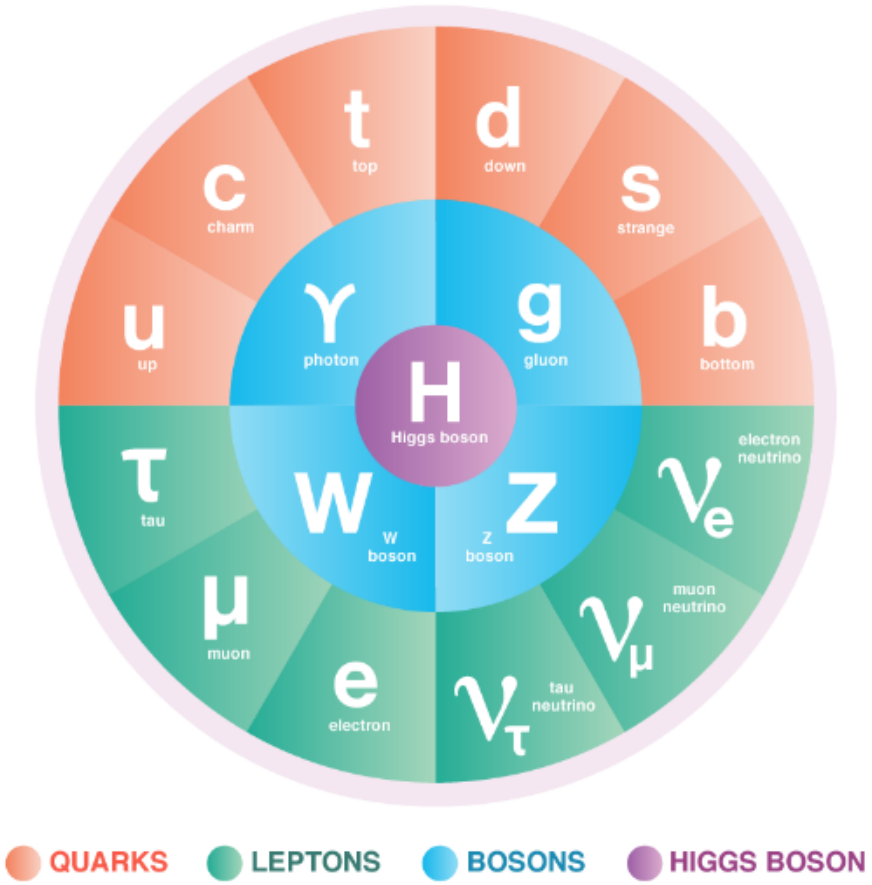


Figure 2.1: A diagram of the standard model, describing the fundamental particles of the universe, as well as the force carrying particles, as well as the Higgs boson [24].

between flavors was first developed for two flavor neutrino mixing by Ziro Maki, Masami Nakagawa and Shoichi Sakata[22] and later extended by Bruno Pontecorvo in 1967 [23].

In the analogous flavor change for quark oscillation, it is required that the particle must be massive to couple with the Higgs field. Neutrinos must also be massive for there to be oscillations, but do not couple to the Higgs field in the same way. The mass of the neutrino is formed into three mass eigenstates, and the flavor oscillations demonstrate coupling to these mass eigenstates. The general neutrino wave function with three mass states are described in Eq. 2.4.

$$\begin{pmatrix} |\nu_1\rangle \\ |\nu_2\rangle \\ |\nu_3\rangle \end{pmatrix} = \begin{pmatrix} U_{e1} & U_{\mu 1} & U_{\tau 1} \\ U_{e2} & U_{\mu 2} & U_{\tau 2} \\ U_{e3} & U_{\mu 3} & U_{\tau 3} \end{pmatrix} \begin{pmatrix} |\nu_e\rangle \\ |\nu_\mu\rangle \\ |\nu_\tau\rangle \end{pmatrix} = U_\nu^T \begin{pmatrix} |\nu_e\rangle \\ |\nu_\mu\rangle \\ |\nu_\tau\rangle \end{pmatrix} \tag{2.4}$$

The mixing matrix, U_ν, is called the Pontecorvo-Maki-Nakagawa-Sakata (PMNS) matrix [21]. This is an analogue to the CKM matrix, describing the mixing of quarks. There are, in general, nine degrees of freedom in a three by three matrix. However in the case of the PMNS matrix it is possible to remove some of the imaginary parameters of U_ν without changing the oscillation probability and the mixing matrix can be parameterized [21]. The mixing matrix can therefore be expressed as Eq. 2.5, where s_{ij} and c_{ij} correspond to $sin(\theta_{ij})$ and $cos(\theta_{ij})$ respectively. In this mixing matrix there is the addition of two physical phases, α_1 and α_2 [25], associated with the possibility that the neutrino is Majorana in nature, or its particle is the same as its antiparticle. If the particle is Dirac in nature, or is distinct from its antiparticle, these physical phases will not exist.

$$U_\nu = \begin{pmatrix} 1 & 0 & 0 \\ 0 & c_{23} & s_{23} \\ 0 & -s_{23} & c_{23} \end{pmatrix} \begin{pmatrix} c_{13} & 0 & s_{13}e^{-i\delta_{CP}} \\ 0 & 1 & 0 \\ -s_{13}e^{i\delta_{CP}} & 0 & c_{13} \end{pmatrix} \begin{pmatrix} c_{12} & s_{12} & 0 \\ -s_{12} & c_{12} & 0 \\ 0 & 0 & 1 \end{pmatrix} \begin{pmatrix} e^{i\alpha_1} & 0 & 0 \\ 0 & e^{i\alpha_2} & 0 \\ 0 & 0 & 1 \end{pmatrix} \tag{2.5}$$

The mixing angles, θ_{ij} have been determined through a series of experimental efforts [25]. As a result it has been possible to generate a magnitude of the PMNS matrix, $|U|$ [26].

$$|U|_{3\sigma} = \begin{pmatrix} 0.801 \rightarrow 0.845 & 0.513 \rightarrow 0.579 & 0.143 \rightarrow 0.156 \\ 0.232 \rightarrow 0.507 & 0.459 \rightarrow 0.694 & 0.629 \rightarrow 0.779 \\ 0.260 \rightarrow 0.526 & 0.470 \rightarrow 0.702 & 0.609 \rightarrow 0.763 \end{pmatrix} \tag{2.6}$$

However, neutrino oscillation experiments are only sensitive to the difference of the masses squared, i.e. $|\Delta m^2_{ij}|$ [21]. This can be demonstrated using the simpler two flavor mixing case, where the PMNS mixing matrix would be Eq 2.7.

$$U = \begin{pmatrix} cos\theta & sin\theta \\ -sin\theta & cos\theta \end{pmatrix} \tag{2.7}$$

The probability of a neutrino changing flavor would be defined by Eq.2.8 [21], where $\alpha \neq \beta$.

$$P_{\nu_\alpha \rightarrow \nu_\beta} = sin^2 2\theta \cdot sin^2 \frac{\Delta m^2}{4E} L \tag{2.8}$$

Oscillation experiments only allow the measurement of the mass difference between mass eigenstates, therefore cannot determine the absolute mass of the neutrino. It is not possible to know the ordering of the mass states m_1, m_2 and m_3. There are two potential orderings for the neutrino mass, the normal hierarchy (NH) and the inverted hierarchy (IH)[21]. This is demonstrated in Fig. 2.2 [27]. The so-called solar mass splitting; $|\Delta m^2_{21}| \approx 7.6 \times 10^{-5}\text{eV}^2$ is approximately 2 orders of magnitude smaller than the mass splitting $|\Delta m^2_{31}| \approx 2.5 \times 10^{-3}\text{eV}^2$[28]. The NH predicts a mass ordering $m_1 \leq m_2 < m_3$, whereas the IH predicts a mass ordering $m_3 < m_1 \leq m_2$. The hierarchy has implications on $\sum m_\nu$, and sensitivity of future experiments attempting to determine the neutrino mass.

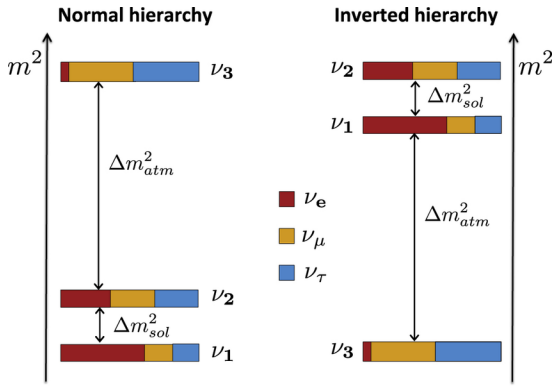


Figure 2.2: The two possible mass hierarchy schemes for the neutrino are shown, the inverse hierarchy (IH) and the normal hierarchy (NH). The fractions of the neutrino flavors ν_e, ν_τ and ν_μ are shown.

2.1.3 Determining the Neutrino's Mass

It has been proven from neutrino oscillations that the neutrino has mass. However, the absolute value of that mass is unknown as neutrino oscillations are not sensitive to the absolute mass value [21].

So what is known about the absolute mass of the neutrino? There are two usual approaches: direct mass measurement by study of endpoint energy for beta decay and cosmological limits. Cosmological observations place an upper limit on the neutrino mass by observing the expansion of the universe [29]. As there are almost as many neutrinos as there are photons, even small changes in the neutrino mass will have an impact on the overall mass density of the universe. The neutrino mass density in the universe is approximately:

$$\rho_\nu \approx 2 \times 10^{-31} m_\nu \ gcm^{-3} \tag{2.9}$$

where m_ν is in units eV/c^2. In this example, the universe would be closed, or the universe would be collapsing instead of expanding, if $m_\nu \geq 25 \ eV$. A more stringent limit on the neutrino mass has been placed using a series of measurements of galaxy clustering. In 2018, Ref. [30] placed a limit of $\sum m_\nu < 0.12$ eV, where $\sum m_\nu$ is the sum of the three neutrino mass states. This indirect method of placing limits on the neutrino mass uses the fact that massive neutrinos would have a strong suppression of the cluster of galaxies [31]. Charged current processes involving ν_e and $\bar{\nu_e}$ and nucleons also play a relevant role in cosmology [32].

Another method to determine the neutrino mass is the direct mass measurement of the endpoint energy of a β decay. In a β decay, the energy released in the decay is shared between the $\bar{\nu_e}$, the β^- particle and the recoiling nucleus. If the recoil energy from the nucleus is neglected, then the maximum energy the β^- particle can obtain is the total decay energy with a reduction equivalent to the mass of the neutrino. The KATRIN experiment is one example of an effort to measure the neutrino mass by measuring the end point of the tritium β decay spectrum [33]. The benefit of using the endpoint energy of β decay is that there is no use of a cosmological model and it is not dependent on the neutrino being majorana or

dirac. There are some limitations in the uncertainty of end point measurements including the accuracy of the total decay energy, and whether it is possible to experimentally observe a decay where m_ν is incredibly small [34]. To adjust for these limitations, the total decay energy is left to be a free parameter and the limits of the neutrino mass are deduced by looking at the shape of the decay spectrum. Recently the KATRIN experiment has placed a new limit on the neutrino mass of $m_\nu < 0.8$ eV c^{-2} at a 90% confidence limit where $m_\nu = \sum_i |U_{ei}|^2 m_i^2$ [33].

2.1.4 The Nature of the Neutrino and the Seesaw Mechanism

With an understanding of neutrino oscillations, implications of how it interacts with other fermions, and the distinction of it being massive, we now encroach on the neutrino's nature. It is well understood that the neutrino is elusive and weakly-interacting. Every second, 6×10^{10} solar neutrinos flow through one cm^2 on earth, mostly completely unnoticed [29]. Therefore with a particle as unobtrusive as the neutrino, it is far from surprising that many of its mysteries remain unsolved.

The mystery that this thesis will suport is answering the question; what is the neutrino's nature? Are they Dirac particles or Majorana particles? First, it is worth discussing what has been observed about the neutrino. The Dirac equation for a free field ψ is written in terms of its Weyl components ψ_L and ψ_R to define chirality.

$$i\not{\partial}\psi_L = m\psi_L$$
$$i\not{\partial}\psi_R = m\psi_R$$

If $m = 0$, then the equations can be treated separately. Therefore if the neutrino is massless there is a need to introduce both chiral components. However as the neutrino is massive, the two components become intertwined as they propagate in time [32].

What has been observed is left-handed, chiral neutrinos which are weakly interacting. By left-handed it is meant that the neutrino's spin is opposite to the linear momentum, whereas the antineutrino is right handed, or the spin is in the same direction as its linear momentum. There are different explanations as to why only left-handed neutrinos have been observed, which rely on whether the neutrino is Dirac or Majorana.

Dirac Neutrino

The term Dirac neutrinos defines the neutrino as being distinctly different from its antiparticle. The Dirac mass term is in the standard model for quarks and charged leptons, which have been proven to be distinctly different from their antiparticle form[32]. In this vain, it is possible to introduce a Dirac mass term for neutrinos. With a Dirac neutrino, the U_ν matrix will not conserve lepton flavor numbers, as seen with neutrino oscillations. However, the total leptonic charge, $L = L_e + L_\mu + L_\tau$ is a global symmetry and conserved.

As described in the previous section, a non-zero Dirac mass required the particle to have both right-handed and left handed-chiral states. For a Dirac neutrino it would require that the neutrino has a right-handed chiral state that does not interact via the weak force and therefore cannot be observed. This undetected, estranged neutrino is sometimes referred to as a sterile neutrino.

Majorana Neutrino

The term Majorana neutrino defines the neutrino to coincide with its antiparticle . [32]. Only massive fermions with no charge can have a Majorana nature, and only massive particles will have an observable difference between a Dirac or Majorana nature. In fact, with the exception of the neutrino, all other fermions in the standard model have been defined to be Dirac fermions. If neutrinos are Majorana particles, they will not conserve leptonic charge, as there is no conserved quantum number to distinguish between the neutrino and antineutrino. This also means that there is no requirement for right handed neutrino fields and the number of neutrino degrees of freedom is minimized[32].

For small neutrino mass, the Majorana mass term can be treated as a perturbation for the electroweak standard model[32]. The total lepton number therefore would be conserved for all processes where the Majorana mass term would not be involved. An event where the Majorana mass term would be involved is in neutrinoless double beta decay, or $0\nu\beta\beta$. This will be discussed in the next in Section 2.3. The limits placed on the neutrino mass demonstrates that $\sum m_\nu$ is orders of magnitude smaller than that of leptons and quarks. One possible explanation for the discrepancy in mass is the seesaw mechanism.

Seesaw Mechanism

The seesaw mechanism is a model used to describe why the neutrino mass is 10^{-10} of the proton mass[35]. This model connects the tiny left-handed neutrino mass to a very heavy right-handed neutrino mass. As the mass of the left-handed neutrino becomes smaller, the right-handed neutrino must be heavier. This is analogous to considering the eigenstates of a 2x2 matrix [36]. Consider the matrix shown in Eq. 2.10. In this matrix, $\mathcal{M}_{\nu,N}$ is described as the mass matrix for the neutrino, B is the Majorana mass component on the GUT scale ($\sim 10^{25}$ eV), and m_D is the Dirac mass component on the electroweak scale ($\sim 10^{11}$ eV). The GUT scale, or the grand unified theory energy scale is the energy level where it is believed that the electromagnetic force, the weak force and strong force become equal in strength and unify into one force [37]. By inspection, it is clear that the eigenvalues would be λ_+ and λ_-, corresponding to neutrino mass states.

$$\mathcal{M}_{\nu,N} = \begin{pmatrix} 0 & m_D \\ m_D & B \end{pmatrix} \tag{2.10}$$

$$\lambda_\pm = \frac{B \pm \sqrt{B^2 + 4m_D^2}}{2} \tag{2.11}$$

Assuming that $B >> m_D$, then the simplification can be made that $\lambda_+ \approx B$ and $\lambda_- \approx -\frac{m_D^2}{B}$. Using this mechanism, $\lambda_- \approx 1$ eV which agrees with experimental limits. The seesaw mechanism not only sheds light on the small mass of the neutrino, but could also provide an

explanation for the baryon asymmetry in the universe[38]. The baryon asymmetry points out the unequal number of baryons (protons and neutrons) from antibaryons (antiprotons and antineutrons). Various considerations of how the universe was created suggests that the universe started in a state with an equal number of baryons and anti-baryons, so the asymmetry is thought to have been a dynamic result through a method called baryogenisis. The standard model does not provide any insight into how this baryogenisis could have occurred, so physics beyond the standard model is required. One possible physics mechanism to form baryogenisis is leptogenisis, which provides the departure from thermal equilibrium. The seesaw mechanism, which requires a Majorana mass, implies the existence of a singlet neutrino. As a result the lepton number is violated and conversion of lepton asymmetry to baryon asymmetry is possible through standard model processes [39].

2.2 Double Beta Decay

Beta decay is a weakly-interacting process where a nucleus transitions through the interaction with a W boson, and a quark in the nucleus changes its flavor[40]. This change results in the creation of either an electron/antineutrino or positron/neutrino pair, depending on whether the nucleus that transitioned was a neutron or proton respectively. β^- decay and β^+ decay are given by:

$$(Z, A) \rightarrow (Z+1, A) + e^- + \bar{\nu}_e \qquad (Z, A) \rightarrow (Z-1, A) + e^+ + \nu_e \tag{2.12}$$

As the neutrino and the electron are created as a result of the β^- decay, they are defined to have been created at $r = 0$ and therefore carry no orbital angular momentum, $(l = 0)$ [40]. If the neutrino and the electron carry no orbital angular momentum, then the parity, π, of the initial and final states should be the same, as parity is defined by $\pi = (-1)^l$. Hence, the parameters of allowed beta decay are:

$$\Delta I = 0, 1 \qquad \Delta\pi = 0 \tag{2.13}$$

Forbidden β decays, where either one or both of these parameters are changed, occur in nature, but become increasingly less likely as they deviate more from the allowed transitions. The Q-value of the decay will also affect the lifetime of the decay. If the Q-value is large, there will be an increased likelihood of the decay occurring. The Q-value is given by:

$$Q_\beta = [m(Z, A) - m(Z + 1, A)]c^2 \tag{2.14}$$

Where the mass of the isotope with a proton number Z and a mass number A is given by:

$$m(Z, A) = Z \times m_p + N \times m_n - B/c^2 \tag{2.15}$$

From Eq. 2.15, the binding energy, B, has an affect on the effective mass of a nucleus. The binding energy can be parameterized using five terms; a volume term, a surface term, a Coloumb term, an asymmetry term and a pairing term. The pairing term only has an effect on even-even nuclei resulting in some even-even nuclei being more bound than their (Z+1,A) neighbor, but less bound than the (Z+2,A) nuclide. Due to the effect of the pairing term, it becomes energetically more favorable to β decay twice rather than once. An example of the effects of the a pairing term is the decay of ^{76}Ge shown in Fig. 2.3. In ^{76}Ge, the isobar one atomic number higher (^{76}As) has a smaller binding energy, therefore it is energetically impossible to beta decay once. However, the isobar with atomic number two higher, ^{76}Se, has a larger binding energy, so $\beta\beta$ decay is possible for this nucleus.

$\beta\beta$ decay was first proposed by Maria Goeppert-Mayer in 1935 [41]. $\beta\beta$ decay, though energetically possible, is a second order process and the decay is greatly suppressed. This results in large lifetimes for the decay, spanning $10^{18} - 10^{22}$ years. The increasingly long lifetimes of $\beta\beta$ decay has made it difficult to measure directly, with $\beta\beta$ decay yet to be observed in many candidate isotopes. The half life of ^{76}Ge for example is $T_{\beta\beta} = 1.78 \times 10^{21}$ yrs [42]. Directly measuring $\beta\beta$ decay, however provides a rare opportunity to answer the critical question of lepton number conservation through the observation of $0\nu\beta\beta$.

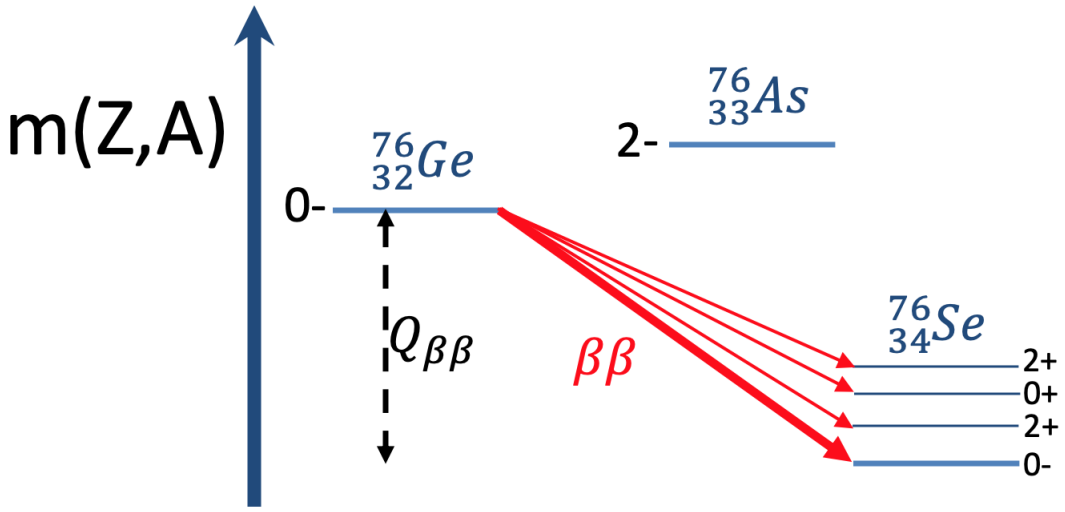


Figure 2.3: The level scheme diagram for the decay of ^{76}Ge by $\beta\beta$ decay [40].

2.3 $0\nu\beta\beta$ and its Implications

In $\beta\beta$ decay, two electrons and two $\bar{\nu}$ are released from the nucleus. The theorized process of neutrinoless double beta decay or $0\nu\beta\beta$ decay, is where during the decay the neutrinos produced are absorbed in two vertices, making it possible only if neutrinos and antineutrinos are of Majorana nature. Because no neutrinos are emitted, the energy of the two electrons should be equal exactly to $Q_{\beta\beta}$ and therefore easy to identify. This is described by the Feynman diagram in Fig. 2.4.

If $0\nu\beta\beta$ decay were observed, it would violate lepton number conservation, i.e. the number of leptons would not be the same before and after the decay. It would also demonstrate that the neutrino has a Majorana nature, and therefore its own antiparticle. As previously described, the nature of the neutrino has strong implications on models addressing interactions in our universe [43]. The existence of $0\nu\beta\beta$ decay and degree of lepton violation can be used to derive parameters for leptogenesis and further our understanding of the matter-antimatter asymmetry in the universe.

It is possible to deduce other physical properties of the neutrino by measuring $T_{1/2}^{0\nu\beta\beta}$, such as the neutrino mass [9]. As previously mentioned, it was presumed that the neutrino was a massless particle until the discovery of neutrino oscillations. These oscillations were not able to measure the absolute mass of the neutrino, but did demonstrate a three neutrino mixing framework. In this three neutrino framework, the mass is generated by the neutrino mass matrix, where $m_\nu = U m_{ii} U^T$ [9]. Here m_{ii} corresponds to the diagonal matrix of the three massive states $(m_{ii}, i = 1, 2, 3)$ and U is the Pontecorvo-Maki-Nakagawa-Sakata (PMNS) matrix, shown in Eq. 2.4.

Under the assumptions that the neutrino is a massive Majorana particle, and there are no other non-neutrino processes in the $0\nu\beta\beta$ decay, it is possible to relate the $0\nu\beta\beta$ decay half life to the effective neutrino mass, $m_{\beta\beta}$ [44]:

$$T_{1/2}^{0\nu} = (G|M|^2\langle m_{\beta\beta}\rangle^2)^{-1} \backsimeq 10^{27-28}\left[\frac{0.01eV}{\langle m_{\beta\beta}\rangle}\right]^2 yrs \tag{2.16}$$

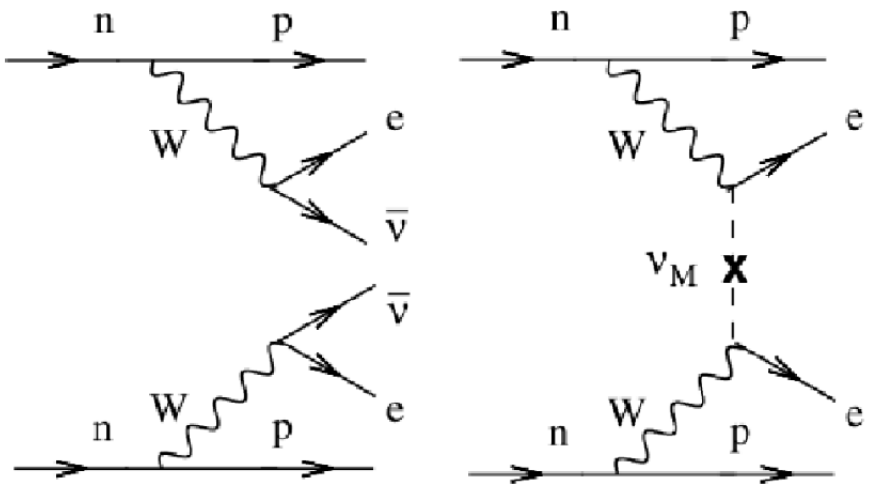


Figure 2.4: Feynman diagrams for $\beta\beta$ decay. The left diagram illustrates the observed $2\nu\beta\beta$ decay and the right diagram illustrates the theorized $0\nu\beta\beta$ decay for the Majorana neutrino [45].

In Eq. 2.16, G is the phase space factor and is on the order of $10^{-25}y^{-1}eV^{-2}$ [44] and M is the nuclear matrix element which can be approximated to $|M| \sim 10$. From this it is clear that the mass scale of the neutrino, $m_{\beta\beta}$, has a direct effect on the $T_{1/2}^{0\nu\beta\beta}$. The neutrino mass ordering will have a direct implication on $\langle m_{\beta\beta}\rangle$, whether it be NH or IH. If the hierarchy is IH, there would be an overall larger $\sum m_\nu$ as two of the neutrino masses would be “heavy" and one would be “light". If the hierarchy is NH, there would be an overall smaller $\sum m_\nu$ as two of the neutrino masses would be ”light" and one would be “heavy".

2.4 Measuring $0\nu\beta\beta$

There are a number of contributing factors to the experimental sensitivity of $T_{1/2}^{0\nu\beta\beta}$ including peak detection at the $Q_{\beta\beta}$ value, background suppression and separation of $2\nu\beta\beta$ events from $0\nu\beta\beta$ events. Different technologies are being developed to measure $0\nu\beta\beta$ decay internationally, each playing to different strengths.

Although the technologies for different experiments vary, most have in common that the target isotope is also the detecting material. Each detector measures the sum of the outgoing electron energy released in the $\beta\beta$ decay. The summed energy of the electrons from $2\nu\beta\beta$ decay has a spectrum shape, similar to that of β decay, continuous from zero to some point just short of $Q_{\beta\beta}$. However, the summed energy of the electrons from $0\nu\beta\beta$ decay will form a mono-energetic peak at $Q_{\beta\beta}$ with a width set by the rsolution of the detector [46].

Current limits of $T_{1/2}^{0\nu\beta\beta}$ in common isotopes like ^{76}Ge and ^{136}Xe are $> 10^{26}$ yrs [9]. Future large scale experiments with competing technologies will have to adapt to improve their $0\nu\beta\beta$ decay sensitivity. This sensitivity is defined by two parameters; sensitive exposure and background in the region of interest (ROI) [47].

Sensitive exposure, ε is the product of the isotope mass and the live time of the detector. It is corrected for the active volume of the detector and the signal detection efficiency. As the $0\nu\beta\beta$ decay signal is Gaussian in nature, it is also corrected for the likelihood that $0\nu\beta\beta$ decay falls in the ROI. Background, $\mathcal{B}$ is the rate of the background events in the ROI after all analysis cuts. The dimensions of $\mathcal{B}$ are counts per unit of sensitive exposure [47].

With these two parameters, it is possible to derive the number of signal and background events in the final spectrum.

$$N_{0\nu\beta\beta} = \frac{ln2 \cdot N_A \cdot \varepsilon}{m_a \cdot T^{0\nu}_{1/2}} \qquad N_{bkg} = \mathcal{B} \cdot \varepsilon \tag{2.17}$$

In Eq. 2.17, N_A is Avogadro's number, m_a is the molar mass of the target isotope and $T_{1/2}$ is the half life of the $0\nu\beta\beta$ decay. With these two parameters in mind, it is possible to compare a number of leading detector technologies on their discovery potential, or the probability of being able to absolutely detect a $0\nu\beta\beta$ signal if the neutrino is truly Majorana in nature.

2.4.1 International Effort to Measure $0\nu\beta\beta$

The most popular detection mechanisms in $0\nu\beta\beta$ decay include bolometers (CUORE, CUPID), semiconductors (Gerda, MAJORANA, LEGEND), scintillators (SNO+, KamLAND-ZEN, NEMO-3) and combinations of TPC and scintillators (EXO, nEXO). Bolometers and semiconductors both have excellent energy resolution, however it is increasingly more expensive and non-trivial to progress to large geometries [48]. Scintillators on the other hand can be easily scaled to very large masses, therefore increasing the ratio of isotropically enriched material in the sensitive region of an experiment. Scintillators have poorer energy resolution than other technologies like semiconductors and bolometers, so the signal detection efficiency and background subtraction becomes non-trivial. As the resolution of scintillators gets worse, the Gaussian of the $Q_{\beta\beta}$ overlaps with the $2\nu\beta\beta$ signal. The isotope selection also has an effect on the discovery potential as it defines the natural abundance and hence the cost, as well as the $Q_{\beta\beta}$ value of the decay.

The experiments pursuing the measurement of $0\nu\beta\beta$ are listed in Table 2.1. For an experiment hoping to detect $0\nu\beta\beta$ decay, it is important to consider a number of things. First, is the energy resolution of the experiment, and therefore the ability to separate events from $2\nu\beta\beta$ from $0\nu\beta\beta$ decay. Another to consider is the isotopic abundance of the isotope used to measure $0\nu\beta\beta$, as large masses are required (>ton-scale) to be able to be sensitive

Table 2.1: Table of leading $0\nu\beta\beta$ decay experiments internationally.

Experiment	Isotope	Isotope Mass kg	ϵ $\left[\frac{kg_{iso}yr}{yr}\right]$	$\mathcal{B}$ $\left[\frac{cts}{kg_{iso}ROIyr}\right]$	$T_{1/2}$ 3σ Sensitivity
LEGEND 200	^{76}Ge	175	119	1.7×10^{-3}	8.4×10^{26}
LEGEND 1000	^{76}Ge	873	593	2.8×10^{-4}	4.5×10^{27}
CUORE	^{130}Te	206	141	3.1×10^{-1}	5.4×10^{25}
CUPID	^{130}Te	543	422	3.0×10^{-4}	2.1×10^{27}
SNO+ PHASE I	^{130}Te	1357	164	8.2×10^{-2}	1.1×10^{26}
SNO+ PHASE II	^{130}Te	7960	1326	3.8×10^{-2}	4.8×10^{26}
KamLAND-ZEN	^{136}Xe	750	194	3.6×10^{-2}	4.8×10^{26}
KamLAND2-ZEN	^{136}Xe	1000	325	2.1×10^{-3}	8.0×10^{26}
NEXT 100	^{136}Xe	91	26.5	4.4×10^{-2}	5.3×10^{25}
NEXT 1500	^{136}Xe	1367	398	2.9×10^{-3}	7.9×10^{26}
nEXO	^{136}Xe	4507	1741	4.4×10^{-4}	4.1×10^{27}

to a reasonable $T_{1/2}^{0\nu\beta\beta}$. As well, it is important to consider the background events that can be seen inside the detector.

As mentioned, there are two possible neutrino mass orderings, IH and NH. The ordering of the neutrino mass will have an impact on the sensitivity of all of these measurements, as the mass of the neutrino directly impacts the half life of $0\nu\beta\beta$. This is shown in Fig. 2.5 where the lightest neutrino mass, m_l, is plotted against the effective Majorana mass, $m_{\beta\beta}$ for either the IH (here defined as IO or Inverse Ordering) or the NH (or the NO, normal ordering) [47]. It is shown that in the NH, the lightest neutrino mass becoming much smaller will result in the $\sum m_{\beta\beta}$ becoming much smaller, decreasing the $m_{\beta\beta}$, and making the measurement of $0\nu\beta\beta$ increasingly more difficult. This will hold true for all $0\nu\beta\beta$ experiments that will attempt to measure the decay.

Of the many technologies and collaborations hoping to determine the neutrino's nature, this dissertation will focus on $0\nu\beta\beta$ measurements with the isotope ^{76}Ge as a semiconductor detector. Germanium has already been developed as a semiconducting radiation detector in industry, measuring the ionization charges directly [48]. An example is High Purity Germanium Detectors (HPGe) which are used for gamma-ray spectroscopy. By using the target isotope as the radiation detector, and by using a radiation detector with optimal energy resolution, the potential of measuring $0\nu\beta\beta$ decay can be significantly increased. While ^{76}Ge detectors are extremely radio pure, attention should be paid to components that hold detectors and readout their signals. More detail on ^{76}Ge detectors and the LEGEND Experiment are outlined in the next section, Ch. 3.

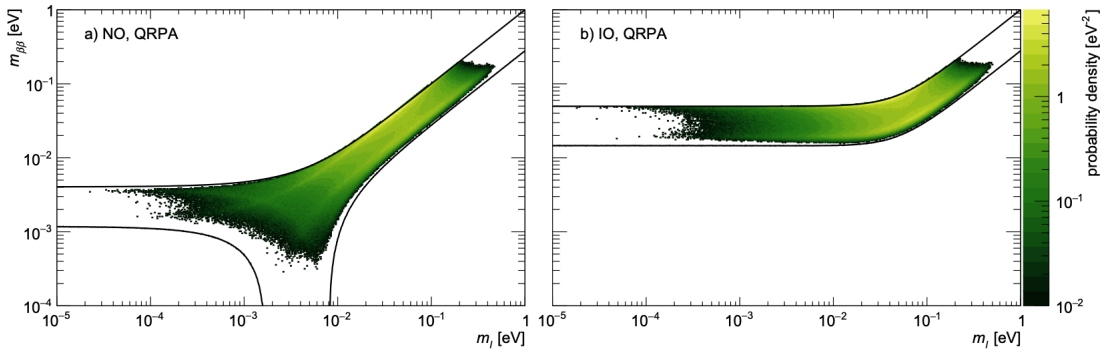


Figure 2.5: Distributions for the effective neutrino mass [47], $m_{\beta\beta}$ and the lightest neutrino mass, m_l, for the NH and IH of neutrino mass states. Here the solid lines show the allowed parameter space and the probability density is normalized by the logarithm of $m_{\beta\beta}$ and m_l.

Chapter 3

The LEGEND Experiment

Currently there are multiple detector technologies pursuing the measurement of $0\nu\beta\beta$ decay as listed in Chapter 2. The technology this dissertation will be focusing on supporting ^{76}Ge as a target material and detector to measure $0\nu\beta\beta$ decay. In this chapter, I will outline previous, current and future experimental efforts to measure $0\nu\beta\beta$ decay.

3.1 $0\nu\beta\beta$ Experiments Using ^{76}Ge

Germanium is used as a semiconducting radiation detector, measuring the ionization charges directly [48]. A commonly used germanium detector in gamma-ray spectroscopy is the high purity germanium detector (HPGe). These detectors have excellent energy resolution and have had demonstrated success in a number of nuclear experiments [49, 50, 51]. As a result there are well defined methods of purification and fabrication for HPGe detectors, with impurities present at less than 1 part in 10^{12} [48]. HPGe detectors used to measure $0\nu\beta\beta$ decay have the best energy resolution of all the detector technologies with a 0.12%(FWHM) at $Q_{\beta\beta}$ [9]. This provides a powerful method to reduce background due to the smaller ROI, and allows for the identification of residual radioactive contamination via precision gamma-ray spectroscopy.

The two collaborations that led the previous generation of measuring $0\nu\beta\beta$ decay with ^{76}Ge detectors are GERDA and the MAJORANA Demonstrator (MJD). Both collaborations explored using HPGe p-type point contact (PPC) type of germanium detectors with a total active mass of tens of kilograms in each experiment. The PPC detectors provide the ability to discriminate between single-site signal and multi-site background events. A single site event is characterized by a single energy deposition in a region of < 1 mm^3, where a multi-site event is usually separated by ~ 1 cm [52]. $0\nu\beta\beta$ decay events will be single site events as the two outgoing electrons will deposit their energy in a region < 1 mm^3. Conversely, background γ-rays will commonly Compton scatter multiple times within the crystal and be detected as multi-site events. The PPC detectors also have a low capacitance and therefore have a lower energy threshold, allowing the detectors to be sensitive to new physics like dark matter interactions at $Q << Q_{\beta\beta}$ [53].

GERDA and MJD had different approaches for pursuing a tonne-scale germanium experiment. GERDA was based at Laboratori Nazionali del Gran Sasso (LNGS) in L'Aquila, Italy. Approximately 40 kg of bare 86% enriched ^{76}Ge HPGe detectors were immersed in a liquid-argon (LAr) cryostat to minimize the amount of mechanical components and utilized low-Z shielding (Fig. 3.1). This LAr cryostat acted as both a cryogen and as a scintillation veto detector, with shrouds of wavelength shifting fibers acting as light guides, delivering argon scintillation light to photodetectors a distance away. This allowed the experiment to veto background events without placing radio-impure photodetectors near the ^{76}Ge crystals.

MJD was based at Sanford Underground Research Facility in Lead, South Dakota, USA. The experiment operated 29.7 kg of 88%-enriched ^{76}Ge and 14.4 kg of natural *Ge* p-type point-contact detectors (Fig. 3.2). Unlike the GERDA experiment, the MJD experiment installed the ^{76}Ge crystals in two large, custom built copper vacuum cryostats, encapsulated in a graded shield consisting of layers of copper, lead, an active muon veto, polyethylene and borated polyethylene. MJD focused on using ultra-clean materials and careful process controls to reach its background goals. An example of this is the use of electroformed copper, produced in an underground cleanroom to prevent contamination and cosmogenic

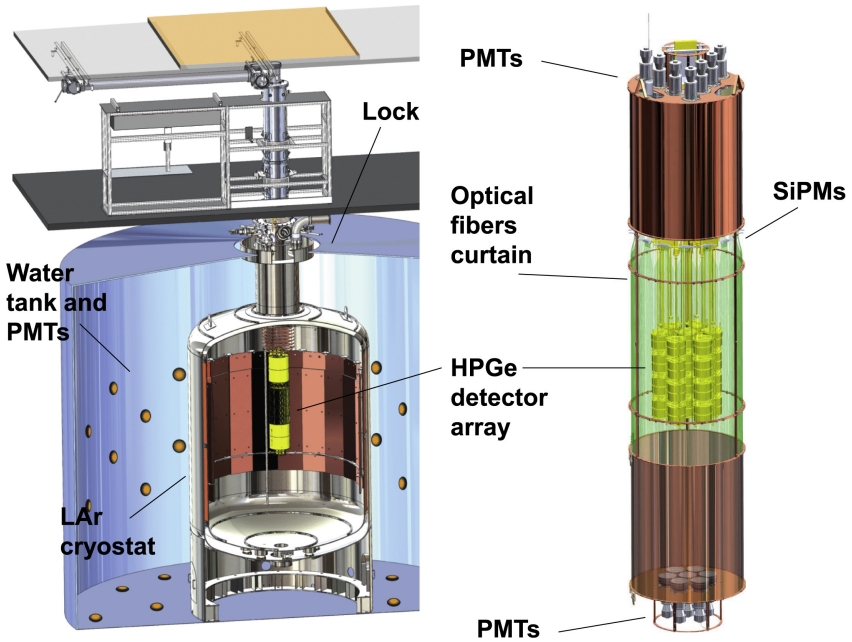


Figure 3.1: This figure shows a layout of the GERDA experiment. The zoom in the right-hand side of the figure displays the inner part of the setup, including an array of ^{76}Ge detectors and the LAr active veto system.

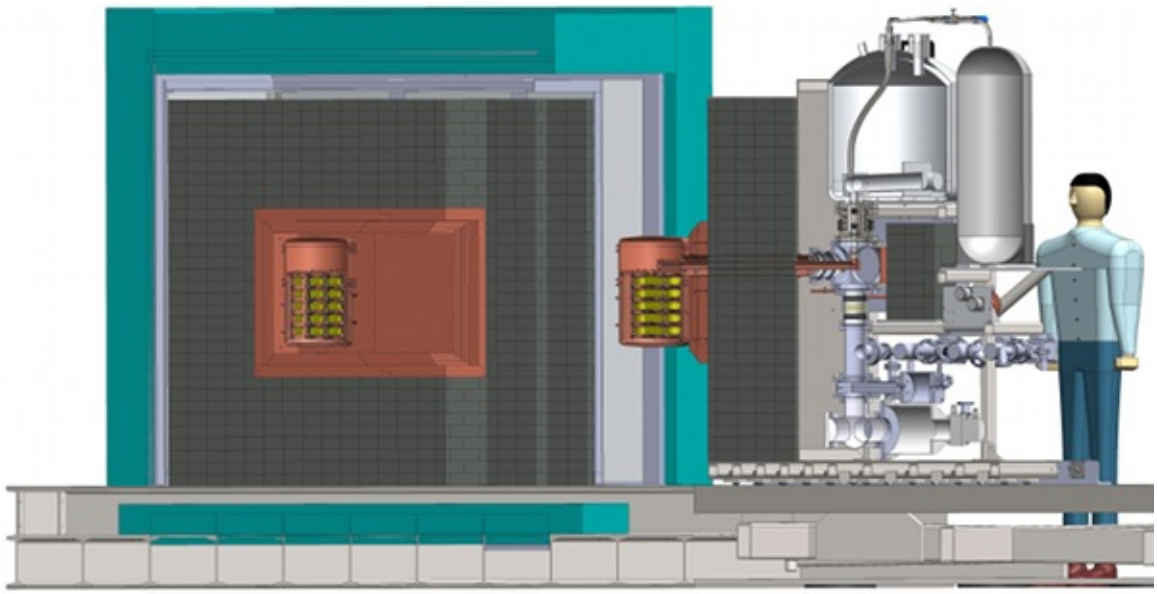


Figure 3.2: This figure shows the cross-section of the MAJORANA DEMONSTRATOR (MJD), where the shielding, installation and scale are shown [54].

activation. This extremely pure copper was used for structural components near the crystals, in the vacuum cryostat and in the innermost copper shielding.

3.2 Overview of the LEGEND Experiment

With each experiment successfully demonstrating the technical feasibility of a large ^{76}Ge detector array, the tonne-scale experiment looks to combine both collaborations' successes in the next generation effort, LEGEND (large enriched germanium neutrinoless double-beta decay). LEGEND combines the advantages of GERDA and MJD by operating with low-Z shielding and a scintillating veto like in GERDA, and strictly using ultra-pure materials and components like in MJD. LEGEND is planned in two stages, an intermediate 200 kg phase and a final phase of 1000 kg of ^{76}Ge with a sensitivity beyond $T^{0\nu}_{1/2} \sim 10^{28} yrs$.

3.2.1 LEGEND-200

The LEGEND-200 experiment is operating 200 kg of ^{76}Ge detectors at LNGS, in a LAr cryostat[11]. The experiment will probe $0\nu\beta\beta$ decay with a sensitivity of $T^{0\nu\beta\beta}_{1/2} \sim 10^{27} yrs$ at 90% confidence level (C.L.), corresponding to a range of the effective neutrino mass of $33-71$ meV within about 5 years [55]. The 200 kg phase will aim to reduce the backgrounds in the detector by a factor of 5 below that of GERDA and MJD. Of the 200 kg, 70 kg of detectors will originate from the MJD and GERDA experiments and the framework is an upgrade from its predecessor, GERDA. The new detectors are inverted-coaxial point contact (ICPC) detectors, with over double the mass per crystal, but still maintaining its excellent energy resolution capabilities. LEGEND-200 is an integral stage for $0\nu\beta\beta$ experiments, as it provides the opportunity to explore future technologies for tonne-scale experiments, with an aggressive timeline made possible by utilizing previous infrastructure.

The design for the LEGEND-200 experiment is ^{76}Ge detectors stacked into strings with a total of 14 strings submerged in the bath of LAr (Fig. 3.3). Each of the ^{76}Ge detectors is supported by 3 ultra-pure electroformed copper rods and PTFE supporting structure

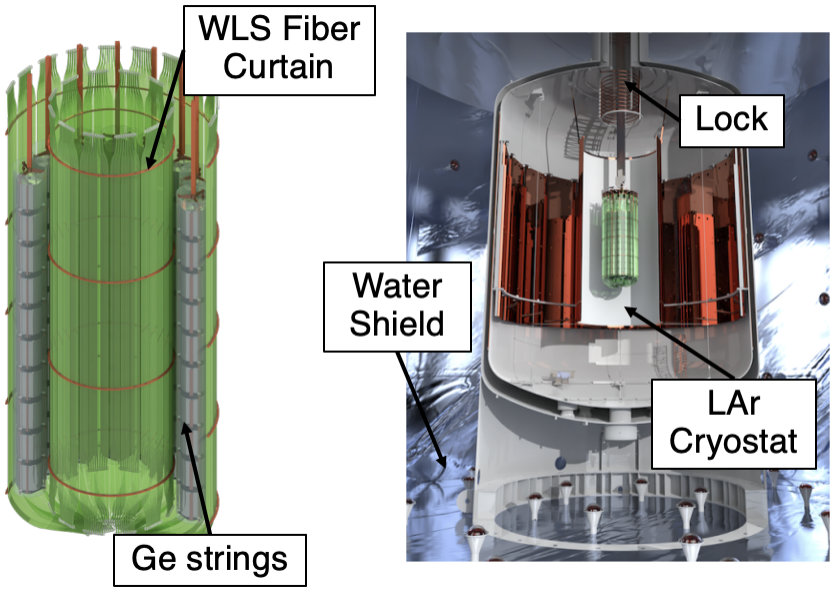


Figure 3.3: This figure shows a layout of the LEGEND-200 experiment. The zoom in the right-hand side of the figure displays the inner part of the setup, including the LAr active veto system and the wavelength shifting (WLS) fiber curtain.

to maintain the integrity of the string and prevent damage during the submerging process. Between each of these detectors, there is a baseplate to support the positioning of the copper rods and mount the low mass front end (LMFE) electronics. The LMFE electronics are designed to maintain the signal quality from the ^{76}Ge detectors, but reduce the mass and therefore the potential radioactivity of the circuit [56]. GERDA has pioneered the practice of wire bonding the electronic readout directly to the detector surface, which has proven to be reliable and introduce minimal amounts of contamination. MJD's use of high purity materials and process control reduced concern of the LMFE electronics introducing radioimpurities and therefore could be placed very close to the detector ($\sim$ 5cm from the crystal base). This arrangement results in a reduction of noise and improved signal threshold and resolution as well as reduced radioactivity near the detector.

3.2.2 LEGEND-1000

The second stage of LEGEND is LEGEND-1000, an experiment with 1000 kg of enriched ^{76}Ge detectors, which will operate for 10 years. This proposed experiment was recently reviewed in the Department of Energy Nuclear Physics Double Beta Decay Portfolio Review. Out of three international experiments reviewed (LEGEND CUORE and NEXO), LEGEND was chosen for primary funding for U.S. investment strategy. As a result, this proposed experiment is pushing ahead, pursuing innovative methods to improve the detection sensitivity and functionality.

LEGEND-1000 is a similar baseline design to LEGEND-200, with four string arrays with each containing 250 kg of enriched ^{76}Ge detectors (Fig. 3.4). The construction of the strings will be similar to LEGEND-200, with ultra-pure copper support rods creating the structural stability of the detector array and a base plate providing structural support to each detector, as well as providing a platform to attach LMFE electronics and a high voltage supply to bias each detector. Figure 3.5 shows the conceptual design for the detector unit.

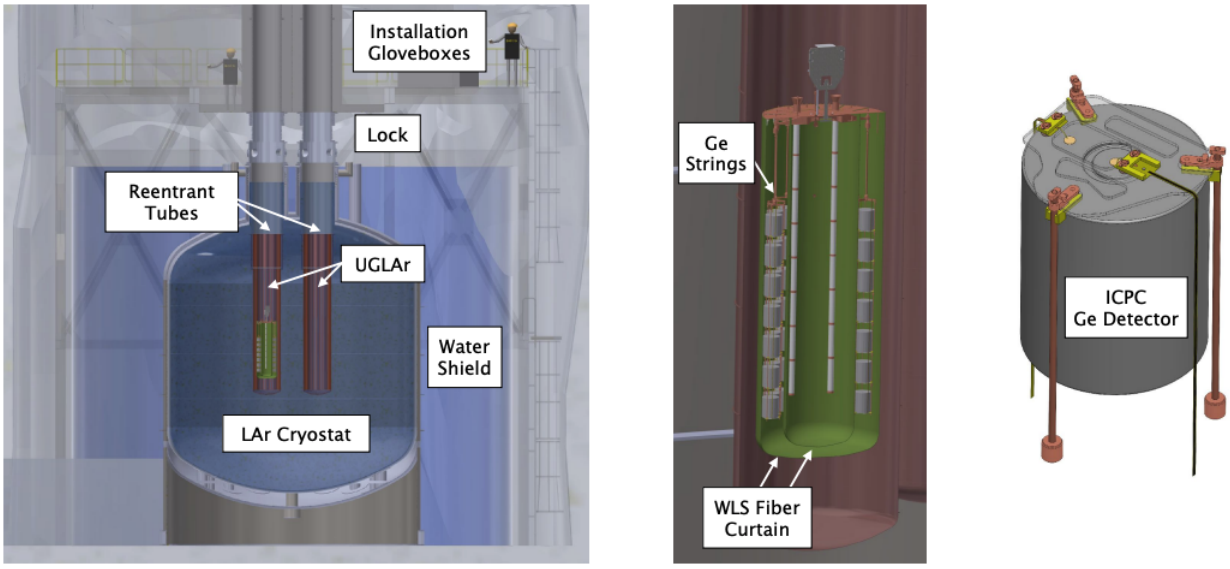


Figure 3.4: The figure on the left outlines the baseline design for LEGEND-1000. This detector has four modules, each housing 250 kg of ^{76}Ge detectors. These modules are filled with underground liquid argon (UGLAr) and submerged in a large LAr cryostat. The LAr cryostat is then surrounded with water in a large tank. A person near the module entrance is shown for scale. The middle figure shows a single module and the LAr light collection system. The right figure shows a single inverted coax point contact (ICPC) germanium detector with the PEN baseplate.

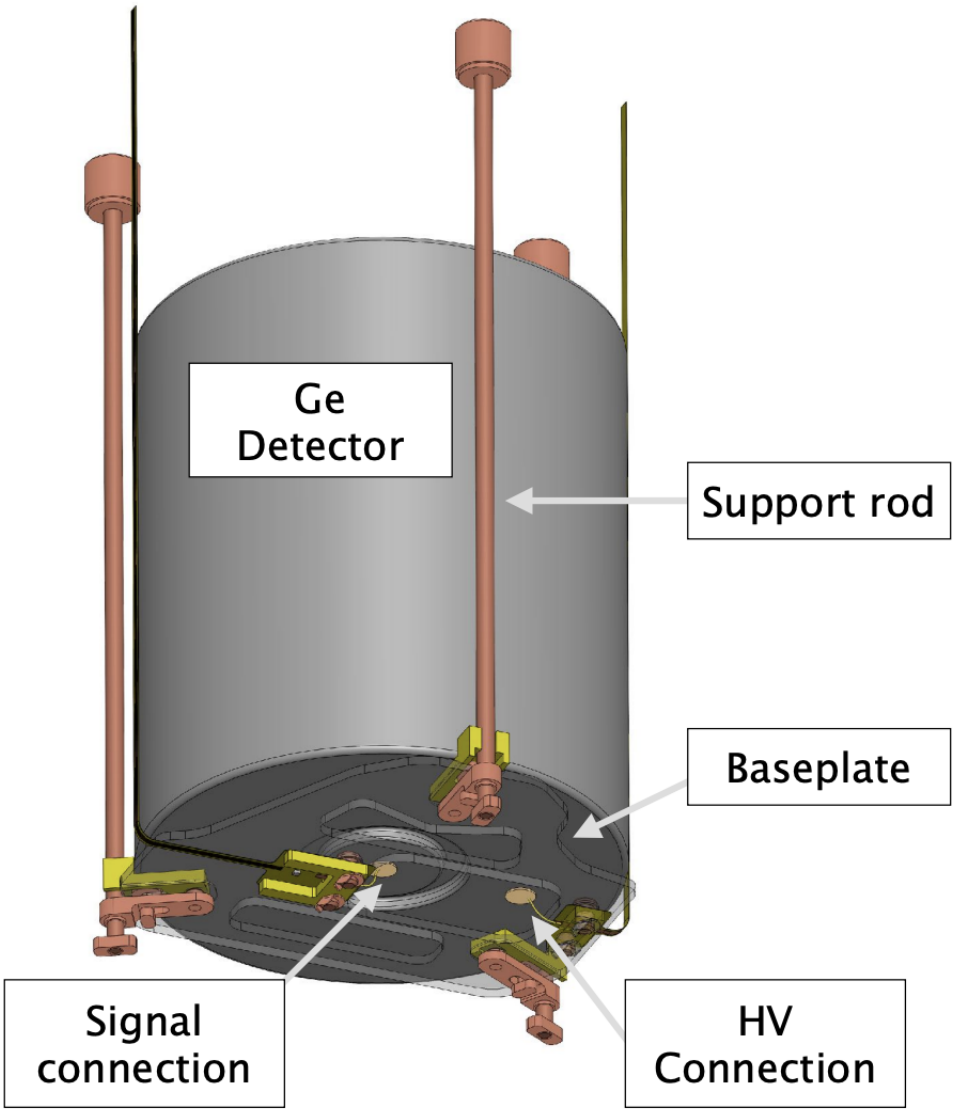


Figure 3.5: Baseline design for a detector unit in the LEGEND experiments. The support structures will be made of ultra-pure materials. For LEGEND-1000, the electronics will be modified from those used in LEGEND-200 to further improve the detector signal quality [11]

The location of LEGEND-1000 has not yet been decided, so some specific details of the geometry of the outer detector are fluid to ensure the experiment reaches its background goals.

3.3 Achieving a Quasi-Background-Free Measurement

Both the LEGEND-200 and LEGEND-1000 experiments are pursuing quasi-background free measurements of $0\nu\beta\beta$ decay, requiring the identification and mitigation of all potential sources of background radiation throughout the experimental operation [11]. In this instance, quasi-background free is defined as no background counts measured in the region of interest for the duration of the experiment. The different sources of background radiation are discussed below along with the methods for removing these events.

3.3.1 Sources of Background Radiation in LEGEND

There are a number of potential sources of background radiation in the LEGEND experiments. The sources that are of greatest concern are those which have a decay energy $E \geq Q_{\beta\beta}$, as these signals have the potential to inflate the $0\nu\beta\beta$ decay signal. The first source of background is internal primordial radionuclides, including the uranium and thorium series. These series are present to some level in all materials on Earth, as they were present during the Earth's formation therefore giving all materials some base level of radioactivity. Many of the isotopes in these decay chains have significantly longer half lives than the age of the Earth but the rate of their decays are well characterized (Fig. 3.6).

The radionuclides of interest are ^{238}U, ^{235}U and ^{232}Th. The isoptopes ^{220}Rn and ^{222}Rn, from the ^{238}U and ^{232}Th series respectively, are examples of isotopes that pose a unique risk. This is surprising as radon is an inert noble gas and should not chemically react with any material. However, radon emanated from the environment will adhere to material via the Van der Waals force, and would occasionally not have sufficient kinetic energy to leave the

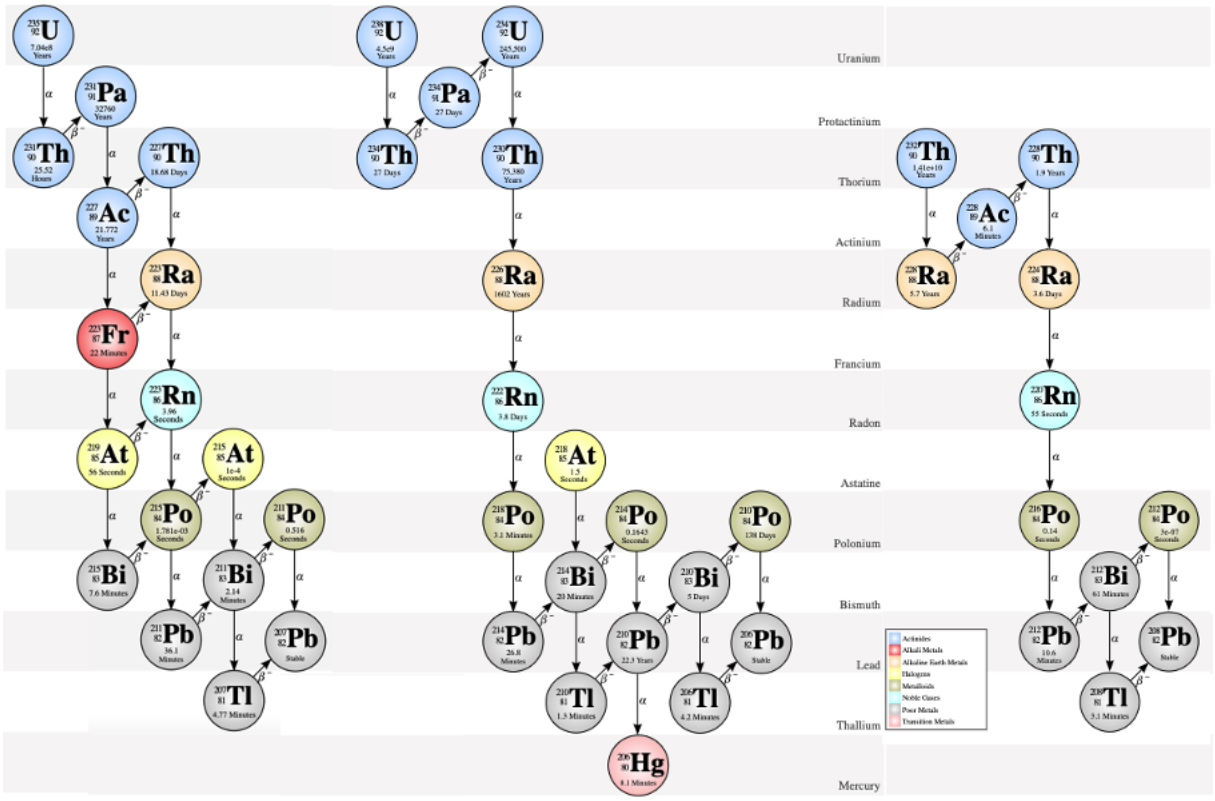


Figure 3.6: Decay chains for the primordial nuclides ^{238}U, ^{235}U and ^{232}Th. These isotopes have extremely long half lives and will produce the radiation shown here.

surface. Additionally, these isotopes of radon will decay into radioactive isotopes that can produce radiation that will inflate the region of interest.

Although these isotopes are naturally present in all materials, it is possible to purify some materials to significantly reduce the amount of primordial radionuclides. One successful example of this is the use of electroformed copper in the MJD experiment [53]. Electroformed copper is copper that is formed using electrolysis of a copper solution onto a conductive surface. By performing this underground they have been successful in creating the most pure commercially available copper.

Another example of this is the ^{76}Ge detectors themselves, which have internal impurities at less than 1 per 10^{12}. As a result, the greatest risk of contamination occurs on the surface of the ^{76}Ge detector. One method used to mitigate background events due to α decays on the surface of the ^{76}Ge detectors is to use Pulse Shape Discrimination, or PSD. PSD uses the shape of the signal to determine what kind of interaction occurred, and where the detector the event happened in the ^{76}Ge detector. By doing so, the liklihood of α decays at 3.5 MeV being included in the data set is decreased to 0.16% [11].

Another source of background radiation events is cosmic rays, high energy protons and nuclei that move through the universe at nearly the speed of light. These cosmic rays interact with Earth's atmosphere, producing secondary high energy particles like pions and kaons, which decay into muons, highly penetrating particles, and can reach detectors several kilometers below the ground. This shower of high energy particles produced by cosmic rays serve as potential background sources in $0\nu\beta\beta$ decay experiments, both directly and indirectly. Indirectly, these high energy particles can result in the cosmogenic production of ^{60}Co and ^{68}Ge in the detector, both of which are radioactive and have substantially long half lives. Fortunately, cosmic rays are strongly absorbed by matter. The most successful way to passively remove background events is to place the experiment underground, with overburden, or rock/soil overlaying the experiment, that can shield the detector.

Although overburden can be used to prevent activation during the experiment, if the sourced materials used in the experiment are exposed to cosmic rays prior to being installed,

they still risk being cosmogenically activated. This is of concern for the argon used in the cryostat, as when ^{39}Ar is cosmogenically activated it forms ^{42}Ar. This radionuclide has a long half life of $T_{1/2} = 32.9$ yrs. While ^{42}Ar only has a Q value significantly lower than $Q_{\beta\beta}$ at $Q = 0.599$ MeV, its short lived daughter, ^{42}K, has a β decay with a high Q value, $Q = 3.525$ MeV, and a short lifetime, $T_{1/2} = 12$ hrs. The resulting ^{42}K has been shown to reach the germanium detectors through convection in the cryostat. The electronics and walls of the cryostat are significantly warmer than the rest of the LAr, causing mixing and convection in the detector system. As a result, the ^{42}K can drift around the cryostat, and potentially move towards a ^{76}Ge crystal (Fig. 3.7). For LEGEND-200, the experiment will mitigate background events from ^{42}K through the use of the LAr active veto system, passive nylon shrouds as well as coincidence cuts between the active veto system and the ^{76}Ge detectors, known as AC cuts. However, as we look toward LEGEND-1000, significant improvements must be made to the passive shielding and active veto system, and/or underground argon (UGLAr) must be used. UGLAr is argon which is sourced underground where there has been significantly less exposure to cosmic rays, and has 1400 times less ^{39}Ar than atmospheric argon [57]. This has been studied extensively by the Darkside collaboration (Fig. 3.8).

One of the secondary particles produced from cosmic rays are muons as a result of charged pion decays. At intermediate energies, GeV to TeV, muons will have less energy loss due to Bremsstrahlung. Therefore these secondary muons will be able to penetrate deep into the Earth, and into underground experiments. Muon events are therefore detected using veto detectors, which can remove these background events using coincidence.

3.3.2 Active veto System in LEGEND

An active veto system is a secondary detector system which detects ambient radiation events. These ambient radiation events have the potential to inflate the region of interest, so by using coincidence cuts with the active veto signals, it is possible to remove these events from the data set.

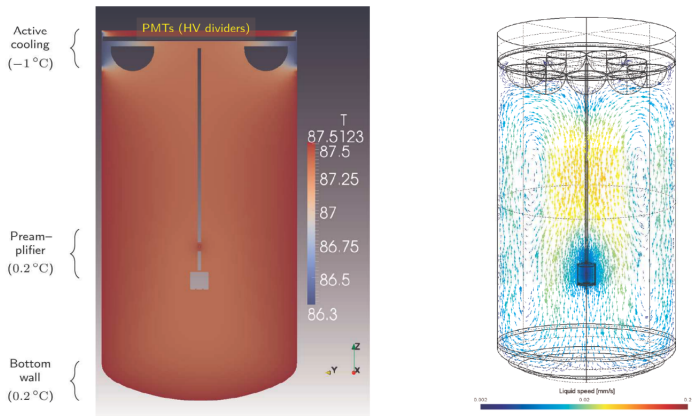


Figure 3.7: This is a heat map (left) and speed distribution of LAr (right) for the LArGe prototype used in the GERDA Collaboration. This prototype consisted of a singular germanium crystal in a large LAr cryostat. This prototype was used to study the contamination and propagation of ^{42}K [58].

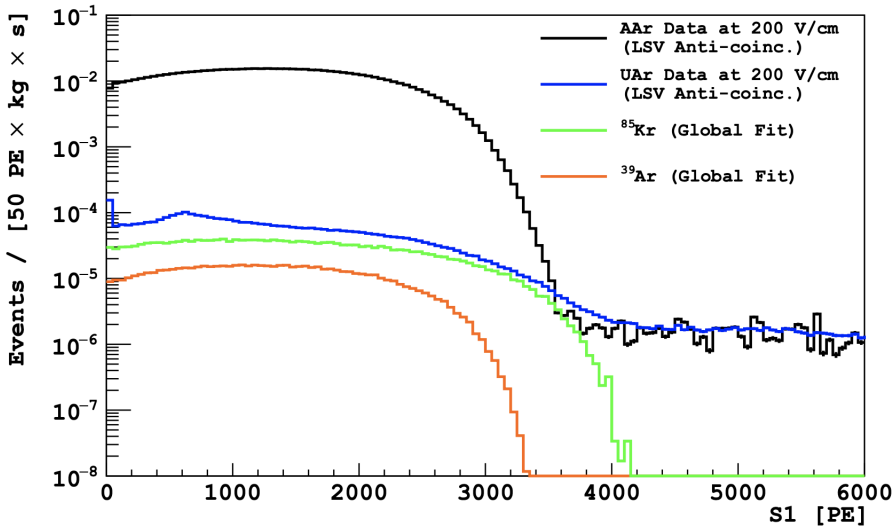


Figure 3.8: A spectrum of single-scatter events in atmospheric argon, AAr (black), and underground argon, UAr (blue), taken with 200 V/cm drift field [57].

The first quasi background-free measurement of $0\nu\beta\beta$ was measured by the GERDA collaboration, who contributed much of the background suppression to the use of a unique active veto system. GERDA submerged its ^{76}Ge crystals into a cryostat of LAr, both cooling the crystals to an operational temperature, and acting as an active veto material via the production of scintillation light.

In the previous section, the potential sources of background radiation were outlined. Most of these sources are reduced and benefit from the use of an active veto system. The active veto systems for the LEGEND experiments are similar to each other, with LEGEND-1000 looking to build and improve on what is found to be successful in LEGEND-200.

LEGEND-200

LEGEND-200 is using both passive and active methods to reach its aggressive background goal of <0.5 counts per FWHM·ton·year. The experiment is located underground, with 3500 m water equivalent of overburden, passively removing cosmogenic backgrounds and reducing the muon flux at the experiment. The detector system is further encased in a 590 m^3 water tank as an additional passive radiation shield. The water tank is also instrumented with 66 photo multiplier tubes (PMTs) to detect Cherenkov light, allowing for the active detection of muons. Inside the water tank, a 64 m^3 LAr cryostat is submerged. The LAr cryostat is both a method of cooling the ^{76}Ge detectors to their operating temperature of 90 K and as an active shield for background radiation. LAr radioluminesces in the presence of radiation, producing light at 128 nm. This light is read out by a series of wavelength shifting fibers surrounding the detector array. These wavelength shifting fibers are coated in tetraphenyl-butadiene, or TPB, so the LAr scintillation light can be shifted to a longer wavelength before being absorbed by the fibers, then read out by a series of silicon photomultipliers (SiPMs) far from the detector strings (Fig. 3.3).

An addition to the LAr active veto system in LEGEND-200, polyethylene naphthalate (PEN) is being used as baseplates to support germanium crystals. In GERDA, these base plates were made out of silicon, which can be produced incredibly pure, with no measurable

radioactivity. However, the silicon is a passive and opaque material, so if LAr light is generated between the crystals, it would be difficult to read out this light. This effect has been given the name shadowing. Alternatively, PEN is an active scintillating material with a peak wavelength of $\sim$ 450 nm and wavelength shifts LAr light. Characterization of the PEN to be used in LEGEND-200 as an active material and its impact on the active veto system is the main focus of this research.

LEGEND-1000

In the baseline design, the LEGEND-1000 experiment is located at SNOLAB in Sudbury, Canada, where the water equivalent overburden is 6010 meters acting as a passive radiation shield. Similar to LEGEND-200, there will be an outer water tank, instrumented as both an active and passive radiation shield and 12 m in diameter. The active veto detection system for LEGEND-1000 will look to use a similar structure as LEGEND-200, but expanding on methods to improve the veto efficiency and radiopurity of the experiment. This will be necessary for LEGEND-1000 to reach its lofty background goal of <0.025 counts per FWHM·ton·year. This is equivalent to a background-free measurement in the region of interest after 10 years of data taking.

One of the improvements being considered is the replacement of passive components with active components. The use of additional scintillating support structures would further improve the geometric efficiency of the active veto system, therefore further reducing backgrounds. One example would be to replace the vertical support rods made of copper (shown in Fig. 3.5) encapsulating the ^{76}Ge crystal with active material, acting as both passive and active shielding for background radiation like β^- particles from ^{42}K.

Chapter 4

PEN as a Low Background Material

As previously described, scintillators are a necessary detector technology in a number of large scale research efforts. However, it is only recently that efforts have gone from considering scintillators as a detecting volume, to considering them also as an alternative to structural components. Ideally in a low background experiment, every material, including the active detecting material, would have the ability to self-veto any background events, providing an absolute background-free environment. Currently, there are a number of inactive structural components in LEGEND that are not able to self-veto and may prevent veto signals propagating to photo-sensors. PEN could be a viable structural scintillator and replace inactive structural materials with self-vetoing components.

4.1 Poly(ethylene 2,6-naphthalte)

Polyesters are a category of polymers that have ester linkages throughout the backbone. An ester is a chemical compound derived from an acid (organic or inorganic) in which at least one OH (hydroxyl) group is replaced by an $-$O$-$alkyl (alkoxy) group [59]. This functional group is illustrated in the skeletal drawing of PEN, shown in Fig. 4.1.

Hundreds of different polyesters exist today, with commercial significance in today's industry. As of 2013, 18% of the world's polymer production consisted of polyesters [59]

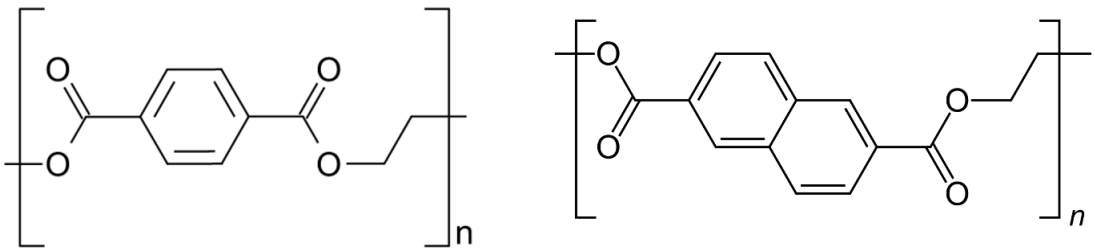


Figure 4.1: Skeletal formula of PET (left) and PEN (right). The ester group can be seen in both PEN and PET.

and in 2018, over 55 million tonnes of polyester fibers were produced [60]. One of the industry's most common polyesters, poly(ethylene terephtalate) (PET) has a number of attractive properties including high strength, high abrasion resistance, high dimensional stability, and chemical resistance at room temperature. Although PET is the most widely used polyester, there have been trends of developing new varieties with industry-specific properties by introducing co-polymers. For example, Polybutylene terephthalate (PBT) has butylenes in the chain linkage, resulting in a rapid crystallization rate- ideal for the injection moulding process [59]. Another example is poly(ethylene 2,6-naphthalate) (PEN). PEN is most commonly used in packaging because of its improved thermal barrier properties [60]. PEN films are also used in producing pressure sensitive tapes and thermal sheets.

In physics research, PEN has been identified as an attractive candidate as a scintillator [61, 7, 62]. Its proposed uses include a structural low-background scintillator for future tonne-scale $0\nu\beta\beta$ experiments, scintillating membrane technology for Kamland-ZEN[7], a radiation hard scintillator for LHC detector upgrades [63], and a wavelength shifter for liquid argon-based scintillators [62]. This aromatic polyester exhibits good mechanical, electrical, and scintillation properties permitting its use not only as an active shield, but also a structural component with a yield strength higher than that of copper at cryogenic temperatures [61].

4.1.1 Scintillation Characteristics of PEN

Radio-luminescence in commercial polyesters was first reported in 2011 with a light yield comparable to standard polyvinyltoluene based (PVT) plastic scintillators [64]. PEN and PET are both unique polymers in that their primary scintillation light is in the blue region ($\sim$400 nm), meaning that unlike PVT, no additional scintillation fluors are required [62]. Fluorescence of PEN was shown to be approximately 4.7 times brighter than PET, with its scintillation emission peaking at 425 nm, versus the 380 nm scintillation peak of PET [64].

The mechanism of PEN and PET fluorescence is by the formation of an excimer [65]. An excimer (an electronically excited dimer) is formed if two molecules of the same unit act

together to emit a photon [66]. Evidence of the formation of an excimer is seen by the shift in the absorption and emission spectrum with concentration. This is demonstrated with the absorption spectrum of dimethyl 2,6-napthalene (DMN), the building block of PEN (Fig. 4.2). The absorption/emission bands associated with the complex are larger than that of the individual molecule. Hence, as solution of a molecule becomes more dilute, the absorption/emission observed shifts from a complex, consisting of an excimer, to a monomeric system.

4.1.2 Wavelength Shifting VUV Light with PEN

PEN is a strong candidate as a structural scintillator for LEGEND not only for its radioluminescence, but also for its ability to wavelength shift vacuum ultra violet (VUV) light ($\lambda = 100 \sim 200$ nm). When the polyester absorbs a photon, it will re-emit a photon in its peak emission range. The shift from the absorbed wavelength to the emission wavelength is described as the Stokes shift. This is a necessary step known as wavelength shifting (WLS), which shifts high energy, short wavelengths to more easily measurable longer wavelengths.

LAr has been used in a number of experiments as either an active veto, the detection medium or as a cryogen for low background experiments [11, 8]. LAr scintillates in the VUV range, with a peak emission at 128 nm. However, there are very few photosensors that are directly sensitive to 128 nm light. Traditional photosensors like glass photomultiplier tubes and silicon photomultipliers are insensitive to these wavelengths and special photosensors that are sensitive have relatively poor efficiencies and are prohibitively expensive [62]. Most experiments combat these effects by wavelength shifting liquid argon scintillation light to range where most common photosensors have a peak efficiency (400-450 nm).

The most common wavelength shifter for VUV light is 1,1,4,4-tetraphenyl-1,3-butadiene (TPB) [61]. TPB has a high wavelength shifting efficiency, but has poor solubility and does not adhere well to surfaces. The wavelength shifting efficiency of PEN was compared to the industry standard in Fig. 4.3 by the PEN working group [61]. The light yield from a 3 mm thick PEN tile was compared to a 1.5 mm thick acrylic tile with 200 μg/ cm^2 TPB

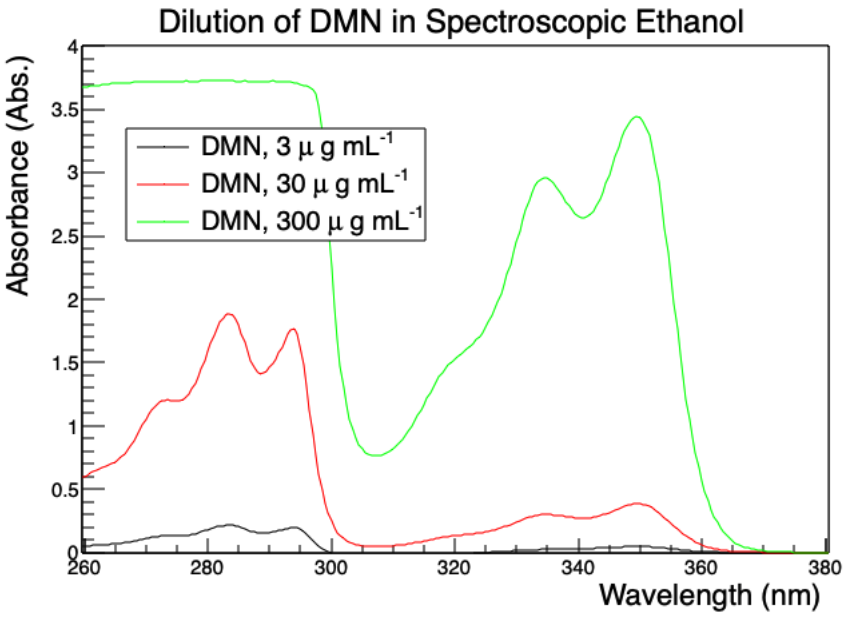


Figure 4.2: Three absorption spectra of dimethyl 2,6-napthalene (DMN) in ethanol.

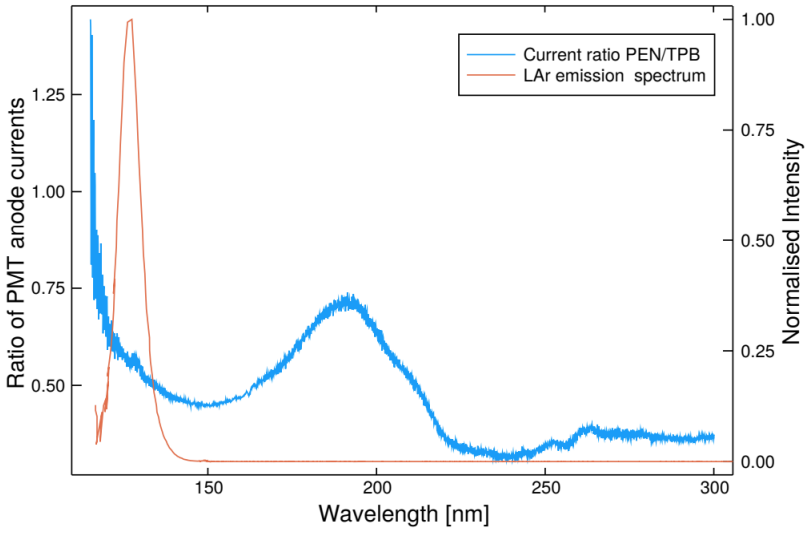


Figure 4.3: This figure describes the relative wavlength shifting efficincy of PEN compared to TPB-coated acrylic. The left axis is the ratio of PMT anode currents (blue line) from the measurements using a PEN tile and a TPB-coated acrylic tile, excited in the range of 116 to 300 nm. The right axis is the VUV/UV emission spectrum of liquid argon (85 K, orange line) with a peak emission at 126.8 nm, highlighting the wavelengths of importance for LAr emission [61].

evaporated on the surface. The PEN tile and the TPB coated acrylic were mounted in a dark box and illuminated using a turntable monochromator. The scintillation light from the tiles was then collected with a PMT and compared. The study concluded that PEN is approximately 60% as efficient as TPB at LAr peak emission ($\lambda = 128$ nm), however TPB cannot be used as a structural material, making PEN a possible alternative for large scale detectors that require stable components.

4.2 Production of PEN Components

PEN is a semi-crystalline polymer which co-exists in crystalline and amorphous phases [61]. Crystallization leads to formation of grain boundaries, which results in optical scattering so the material appears opaque. Crystallinity also results in brittle behavior of the polymer at cryogenic temperatures, which is far from ideal for structural components in liquid argon environments.

The degree of crystallinity can be partially controlled during processing through rapid cooling of the material, from the melt temperature T_m, to below the glass transition temperature, T_g. The Technical University of Dortmund plastics engineers demonstrated that by using injection molding, it was possible to cool PEN from 300°C to $<$ 220°C in less than 10 seconds, resulting in amorphous material [61]. Fig. 4.4 is an image of an injection molding machine with a compression injection molded PEN plate inside. The injection molding machine is filled with polymer pellets by a hopper on top of the machine. The pellets are dried while in the hopper with either compressed air or compressed gas. A specified volume of pellets are then fed into the machine and pushed forward through the neck of the machine by a rotating screw. Here, the material is simultaneously moved forward and heated, forming the melted polymer. The machine then collects a specified volume of the melt and injects it through a nozzle into the mold currently installed. The mold is cooled to a desired temperature, which for producing PEN parts, allows for rapid cooling and the production of amorphous parts.

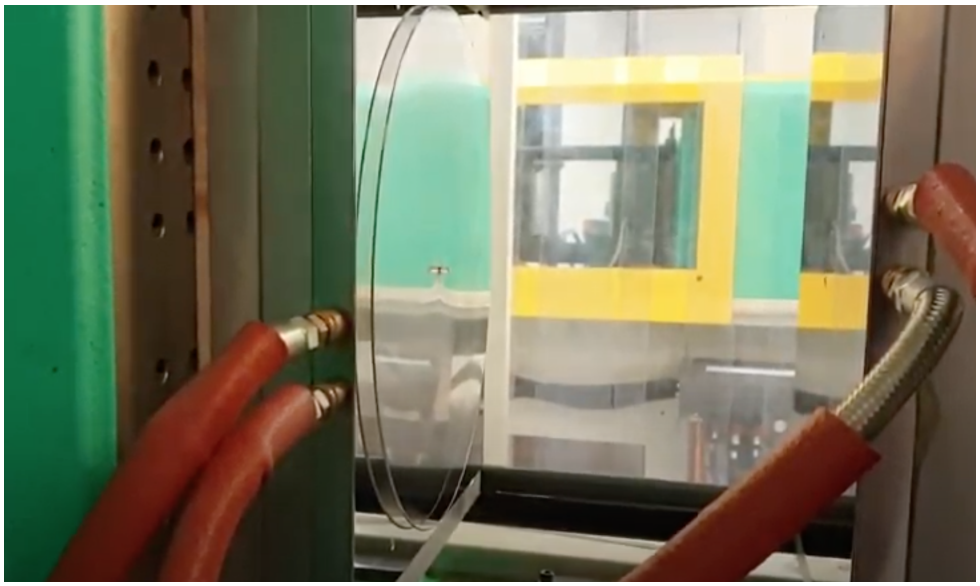


Figure 4.4: Injection molding machine with a PEN plate inside. The PEN plate was produced using compression injection molding, allowing a perfect optical finish and minimal contact.

Though injection molding is successful in producing transparent components, it includes many stages which could possibly introduce radio-impurities to the bulk or surfaces of the material. To combat this, a method was developed by the PEN working group to minimize the introduction of radio-impurities and was validated using multiple methods of radioassay [67].

4.2.1 Radio-Clean Procedure

Washing PEN Pellets

The raw PEN pellets that were used in this process were from Teijin-DuPont, batch number TN-8065 SC. These pellets were first rinsed in 18 MΩ water, then washed in an ultrasonic bath with VLSI (Very Large Scale Integration) grade isopropanol, and then washed again in an ultrasonic bath with 18 MΩ water. This rinsing and washing of the pellets was done twice. Then, after a final rinse, the pellets were dried out in a vacuum tank in $\sim$ 10 kg batches. After being dried for 8 hours at 60°C, the pellets were double sealed in a class 100 clean room plastic bag.

A pilot version of this cleaning method was initially tested by me at Oak Ridge National Laboratory. A 30% HPGe p-type coaxial detector at the High Flux Isotope Reactor counted 870 g of commercial PEN in a polyethylene bottle. The detector was calibrated with a liquid 1-litre multiline commercial calibration solution in the same container geometry as the PEN sample. The initial measurement of ^{40}K activity of these pellets was 3.7 ± 0.63 Bq/kg at 68% CL, prior to washing and without handling the bottle in a clean environment. The container and the pellets were then both cleaned with the following procedure; the polyethylene bottle was acid etched in 2% diluted ACS-grade nitric acid in 18 MΩ water, then rinsed with deionized water and 18 MΩ water, and was finally left to dry in a vacuum oven. The PEN pellets were washed in an ultrasonic bath with deionized water (6 min, 3 times) and with 18 MΩ water (6 min, 3 times) then dried in a vacuum oven in a acid etched PTFE beaker. The cleaning procedure was not conducted in a clean room but lab coats, hairnets, gloves and surgical face masks were used. After cleaning, the ^{40}K activity of the pellets was below the

detection limit, < 22 mBq/kg, more than a factor of 100 times reduction in contaminates. This result suggested that by thoroughly removing surface contaminants from the PEN pellets, there should be an acceptable ^{40}K content for current low background efforts.

Molding of PEN Material

Any component that came into contact with the PEN material during the injection molding process was carefully cleaned with the following procedure: rinsed with 18 MΩ water, washed with VLSI grade isopropanol, then etched in nitric acid solution (2% HNO_3 optima grade, 98% DI water) for 24 hrs and then finally rinsed with 18 MΩ water.

The injection molding machine used for the process was set up inside a Class-1000 clean room. The machine itself was cleaned with VLSI grade isopropanol and the hopper where the PEN pellets were stored was flooded with nitrogen boil-off gas to minimize exposure to radon and remove remaining moisture. The barrel and screw, inner components of the injection molding machine were replaced with new components to minimize the introduction of previous materials. As well, a custom mold consisting of two electropolished stainless steel plates (type 316) were used. By using this mold, it is possible to create a mirror-like finish on the PEN components. The reflectivity of these components is characterized in Section 5.

Using this method, large discs with a 1.5 mm thickness and a diameter of up to 35 cm were produced. After 40 seconds of cooling in the mold, the PEN discs could easily be removed, only being handled by sprue, or the hardened tip of PEN material that still protrudes from the nozzle. Next the disc was moved to a CNC machine, where it was milled to a uniform diameter and the sprue was removed. Next the discs were moved with acid etched pliers into class 100 clean room bags and transported to underground laboratories for screening and storage.

4.3 Radiopurity of PEN Components

Before a component can be installed in an ultra-low background experiment, it must be verified that the radioactivity meets the goals of the experiment. For the PEN baseplates,

this was verified using multiple radioassay methods [67]. By using multiple methods, it is possible to be more sensitive to particular isotopes and the overall confidence in the component's radiopurity can be increased.

4.3.1 HPGe Counting

One of the most direct methods of radioassay is the use of high purity germanium (HPGe) detectors in an underground, ultra low background environments to "count" or measure the radiation produced from the material. This allows the determination of the emission spectrum of a material and therefore the background radiation that can be expected to be produced in the experiment.

HPGe counting measurements were conducted for the PEN material at two locations, the GeMPI setup at Gran Sasso National Laboratory (LNGS) [68] and the OBELIX setup at Modane Underground Laboratory (LSM) [69].

These measurements were conducted at different stages of the PEN processing. The material measured included raw pellets, molded large disks and machined baseplate holders for LEGEND-200. The results in Table 4.1 show that the radiopurity of the material, from the pellets to the molded disks is significantly reduced. This is thought to be due to the extensive surface cleaning of the pellets that took place before molding the material. The limits placed on the LEGEND-200 holders does not verify whether there was additional contamination during the machining process, however these limits still meet the background goal of LEGEND-200 of an activity of < 1 μBq per 5 g part.

4.3.2 ICP-MS Measurement

Another useful method to conduct radioassay is the use of inductively coupled plasma mass spectrometry or ICP-MS. ICP-MS is a type of mass spectrometry that uses the inductively coupled plasma to ionize a sample. The sample usually is required to be a liquid, so solid samples are digested in an acid prior to analysis. Afterwards, it is aerosolized into argon gas, and then accelerated in an Argon plasma torch. The Argon plasma causes the sample

Table 4.1: The radiopurity results achieved for PEN material using HPGe counting at GeMPI and at OBELIX. The limits shown here are given with 90% confidence level.

	Raw TN-8-65S GeMPI4 at LNGS	Discs GeMPI4 at LNGS	Discs OBELIX at LSM	L200 holders GeMPI3 at LNGS
	-	14.315 kg 68 days	5.231 kg 79 days	1.07 kg 68 days
^{228}Ra	$<$ 0.15 mBq/kg	(92 $\pm$25)$\mu Bq/kg$	(107 $\pm$38)$\mu Bq/kg$	$<$ 0.46 mBq/kg
^{228}Th	(0.23 $\pm$0.05)mBq/kg	(32 $\pm$16)$\mu Bq/kg$	(67 $\pm$18)$\mu Bq/kg$	$<$ 0.48 mBq/kg
^{226}Ra	(0.25 $\pm$0.05)mBq/kg	(60 $\pm$15)$\mu Bq/kg$	(76 $\pm$22)$\mu Bq/kg$	$<$ 0.36 mBq/kg
^{234}Th	$<$0.11 mBq/kg	$<$1.9 mBq/kg	-	$<$ 5.8 mBq/kg
^{234}Pa	$<$3.4 mBq/kg	$<$1.7 mBq/kg	-	$<$ 7 mBq/kg
^{235}U	$<$0.066 mBq/kg	$<$56 $\mu Bq/kg$	-	$<$ 0.22 mBq/kg
^{40}K	(1600 $\pm$400)mBq/kg	$<$0.24 mBq/kg	$<$0.567 mBq/kg	$<$ 4.1 mBq/kg
^{137}Cs	$<$0.057 mBq/kg	$<$0.15 $\mu Bq/kg$	-	$<$ 0.091 mBq/kg

to ionize, and then the sample is extracted from the plasma using a skimmer, interference cones and extraction lenses. The beam of ions then travel into a quadrupole of the mass spectrometer, where the ions are separated by their mass-to-charge ratio, allowing only certain ions to be measured by the detector. This method is most successful for trace metal analysis, hence is useful for identifying trace levels of ^{232}Th and ^{238}U.

The ICP-MS measurement conducted for the PEN plates was done at Pacific Northwest National Laboratory (PNNL) where their method and instrumentation is capable to reach μBq sensitivity of ^{232}Th and ^{238}U. The instrument used was an Agilent 8900 ICP-MS and an external calibration standard was used for the quantification of ^{232}Th and ^{238}U. The samples that were measured were two machined LEGEND-200 base plates from the same batch measured using HPGe counting (Table 4.1). The holders were subsampled using stainless-steel scissors and went through two subsequent rounds of acid leaching in 5% HNO_3 for two hours. Afterwards, the leachates were transferred to ultra-clean, validated, PFA vials and analyzed. Table 4.2 reports the final measured values for each leach.

It can be seen that there was a reduction in the levels of ^{232}Th and ^{238}U from the first to the second leach, suggesting that the ^{232}Th and ^{238}U content is representative of surface level contamination from part handling, fabrication or subsampling. It should be noted that for the levels described in Table 4.2, the actual sample mass that was digested into the leachates was unknown, and the results reflect the total mass of the sample. Therefore these values are to articulate a trend rather than accurately qualify the levels of radioimpurities.

After the leachate measurement, the instrument uncertainty was quantified by spiking non-natural levels of ^{229}Th and ^{233}U into blanks and replicating the process. The subsamples were digested in concentrated HNO_3 at 250°C and transferred to identical Savillex vials. The subsamples were then dried out, reconstituted with 2% optima grade HNO_3 and analyzed on the same ICP-MS instrument. For the final PEN samples, the ^{232}Th and ^{238}U levels were below the detection limits. These results suggest that the remaining surface contamination on a PEN plate can be removed by using acid leaching.

Table 4.2: The radiopurity results achieved for PEN material using ICP-MS for ^{232}Th and ^{238}U. The absolute detection limits were calculated as three times the standard deviation of the process blanks and the instrumental precision for a given measurement as the error.

Leachates				
Tile		Sample Weight [g]	^{232}Th [*ppt*]	^{238}U [*ppt*]
PEN Tile 1	leach 1	0.7907	0.071 ±0.013	0.09 ±0.04
	leach 2		0.004 ±0.005	0.0068 ±0.0017
PEN Tile 2	leach 1	0.7136	0.10 ±0.03	0.031 ±0.011
	leach 2		0.0045 ±0.0015	0.007 ±0.002
Samples				
Tile		Sample weight [g]	^{232}Th [*ppt*]	^{238}U [*ppt*]
PEN Tile 1	Sample 1	0.2745	<1.13	<1.98
	Sample 2	0.2481	<1.30	<2.08
	Sample 3	0.2655	<1.22	<1.94
PEN Tile 2	Sample 1	0.2784	<1.02	<1.81
	Sample 2	0.1408	<2.02	<3.57
	Sample 3	0.294	<0.97	<1.71

4.3.3 Radon Emanation

High sensitivity radon emanation measurements are an additional method to understanding the radiopurity of the samples produced. These measurements are performed in a vessel under vacuum, with the sample inside, and a cold stainless-steel plate to collect ^{220}Rn and ^{222}Rn. After, by counting the number of emitted alpha particles emitted from the plate with a semiconductor detector, it is possible to quantify the amount of radon that was pulled from the surface of the part [70]. These radon emenation measurements were conducted using five machined LEGEND-200 baseplates at the Institute of Physics of the Jagiellonian University in Krakow. These measurements were repeated twice and conducted in a 50L vacuum chamber. Limits of $< 16\mu$Bq per holder and $< 12\mu$Bq per holder were placed for ^{220}Rn and ^{222}Rn respectively.

4.4 Synthesis of PEN

Studies with PEN have been mainly performed with commercially available PEN polymer sold as either granulate or thin-films. These materials typically contain discoloration-masking toners, additives, and catalysts which do not lend themselves to low-background and/or scintillator applications. Commercially available material may contain catalysts such as Zn, Mn, Co, Ti, Sb and phosphorous-based thermostabilizers at 10-100s ppm level [71]. Some of these materials have relatively long half lives when activated by neutron capture. An example of this is cobalt, which naturally contains 100% ^{59}Co. This isotope of cobalt can neutron capture to form the long lived ^{60}Co, with a half life 1925 days.

As we look to use PEN as a structural self-vetoing material in future low-background physics experiments, we must consider synthesizing PEN ourselves to meet the stringent radio-purity requirements [11]. A synthesis method has been developed which optimizes optical properties of PEN and aims to limit the exposure of radio-impurities while still maintaining the structural integrity of the polyester. The reaction setup and synthesis product are shown in Fig. 4.5.

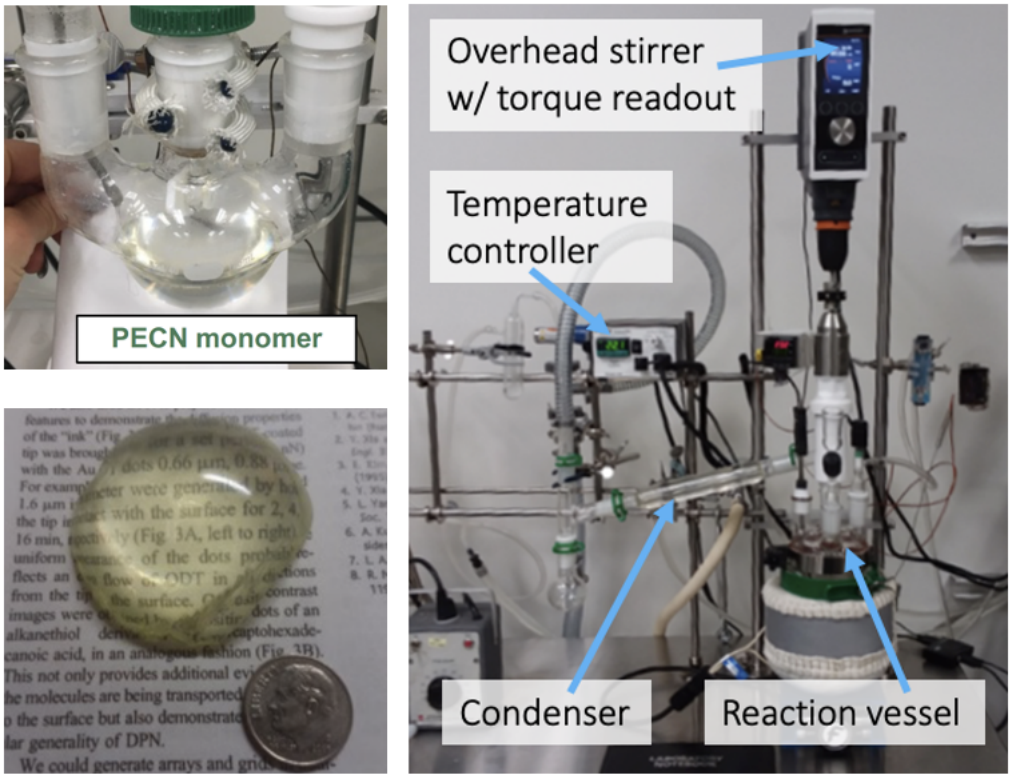


Figure 4.5: Upper left is an image of synthesized PEN monomer, before the polycondensation stage. Lower left is an image of amorphous PEN that has not been allowed to fully polymerize, but still maintains its clarity. Right is an image of the reaction setup. This setup was used for both the transesterfication and the polycondensation stages.

4.4.1 Experimental Methods

The radiopurity implications of all PEN reagents should be considered when synthesizing a low background structural scintillator. The optical and fluorescent properties of the material will improve the self veto efficiency of the material, and should also be considered as a necessity for low background applications.

Improving the Radiopurity

Purifying each of the reagents will improve both the overall radiopurity of the polymer and the optical clarity. DMN is the largest contribution of all reagents by mass. Esters pose a potential pathway for the introduction of radio-impurities as they may contain a small fraction of the parent carboxylic acid and its conjugate base in the form of a salt. The conjugate base may be the in form of a potassium and/or U/Th salt. The efficacy of the purification method in removing radioactive contaminants from DMN will have a strong impact on the overall radioactivity in the PEN. Recrystallization is a simple method of purifying DMN that can be easily scaled to large batches [72], where the solvent used for recrystallization dictates what type of impurity will be removed. For example, dimethyl formamide is an organic solvent with a high solubility for salts, therefore has a high efficacy of removing K and U/Th salt impurities from the DMN.

Cyclohexane-dimethanol (CHDM) is the second largest reagent of the polymer by mass and forms a co-polymer, hindering crystallization in the PEN. Because of the inherently waxy characteristics of CHDM, it is not possible to purify by re-crystallization at room temperature. However CHDM has a low melting point so distillation would be an easier alternativ method to purify the material.

The purification efficacy of DMN was measured by the reduction of impurities in the sample. The impurities of the samples were measured by two methods, Neutron Activation Analysis (NAA) and Inductively Coupled Plasma Mass Spectrometry (ICP-MS). The specific activities of PEN reagents are described in Section 4.4.5.

Another consideration in synthesizing low-background PEN is the choice of catalysts. Typically, transesterification of DMN is performed using a lewis acid [73]. Acetates of zinc and tin are commonly used as catalysts, but both risk being activated by neutron capture forming long-lived radioactive isotopes and therefore a are a risk to the radiopurity [74]. Magnesium acetate is an ideal catalyst for low-background scintillator synthesis as neutron capture on magnesium results in stable isotopes. The concentration of magnesium acetate can also be reduced to further improve the radiopurity, which would extend the transesterfication reaction time but would still result in the reaction reaching completion [75].

The use of antimony trioxide (Sb_2O_3) as a polycondensation catalyst for polyesters has been rigorously studied and demonstrated to produce high molecular weight polymer [76]. However, ^{123}Sb can be activated by neutron capture, forming ^{124}Sb with a half life of 60 days [74]. This not only acts as a potential path for radioimpurities, but also prevents commercial PEN from being radioassayed using NAA. GeO_2 is an attractive alternative as a polycondensation catalyst and is a well-known ultra-high radiopurity material, as demonstrated by the $0\nu\beta\beta$ decay searches using this material to develop ^{76}Ge detectors.

Improving the Luminescent Properties

PEN derivatives contain no strong chromophores, so after synthesis, the polymer should appear white or colorless. Masking the polymer's color with additives like cobalt will not only decrease the attenuation length but also decrease the efficiency of wavelength shifting light. PEN fluoresces by the de-excition of a dimer formed between aromatic structures, hence additives of any kind, perhaps even CHDM, could limit the formation of dimers and therefore the fluorescence of PEN. Minimal additives and reagents should be added to the polymer so that the dimer concentration may be conserved.

As previously mentioned, lewis acids are used for the transesterfication of DMN. Alykoxides of titanium are very effective transesterification catalysts but typically result in undesirable yellow product[77]. From this perspective, a weaker catalyst from group II metals is desirable, such as magnesium acetate. Group II metal complexes, in particular

magnesium, has a reduced absorption in the 400-450 nm range, reducing the attenuation of PEN scintillation light through the plastic [78].

GeO_2 is available to an incredible standard of radiopurity, offering itself as an ideal catalyst already. Additionally, GeO_2 results in a more colorless polymer [79] than Sb_2O_3 which leads to a graylish discoloration due to the formation of black flakes[80].

PEN is a semi-crystalline polymer which co-exists in crystalline and amorphous phases. Crystallization leads to the formation of grain boundaries, which results in optical scattering and the material becomes opaque. The degree of crystallinity can be partially controlled through rapid cooling of the material during processing from the melt temperature T_m to below the glass transition temperature T_g. Stress-induced crystallization and subsequent whitening can still occur in regions of high steer stress. The addition of dopants can also lead to whitening as the dopants can act as nucleation site to promote crystallization. Figure 4.6 shows examples of whitening occurring in commercially available PEN caps during the molding process. This whitening occurred as the material was slowly cooled, resulting in crystalline structures forming. Adding a bulky comonomer, through the addition of CHDM, can frustrate chain-packing and lead to more intrinsically amorphous materials that will circumvent this issue [81]. The addition of CHDM results in the PEN derivative, Poly(ethylene glycol-co-1,4-cyclohexanedimethanol naphthlate) (PECN). PECN has been shown to have similar properties of PEN but with the enhanced clarity of an amorphous polymer [81]. In [81] it has been shown that by introducing CHDM into the chain on the order of 30 mol% prevents crystalline structure from forming in the PEN-PECN copolymer, making it inherently amorphous. Amorphous polymer is ideal for large, more complex geometries, that will not be limited by the cooling time. In Fig. 4.7, synthesized samples of PEN with varying feed levels of CHDM are shown, and a decrease in whitening can be seen.

With DMN having the largest contribution of all reagents by mass, improving its color and organic impurities will have a significant effect on the polymer's color and scintillation. Organic contaminants in DMN can result in side reactions and oxidation during polycondensation, resulting in yellowing or low molecular weight product [80]. Recrystallization can also be used to remove organic impurities. Toluene is an organic

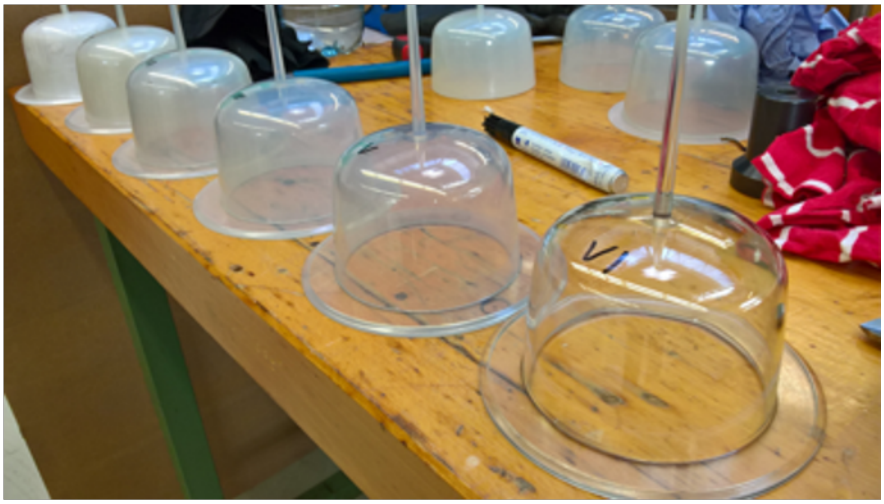


Figure 4.6: This image shows examples of whitening occurring in commercially available PEN caps during the injection molding process. This whitening occurred as the material was slowly cooled, resulting in crystalline structures from forming. As the rate of cooling increases, the material improves in clarity, and therefore has reduced crystalline structures within the caps.

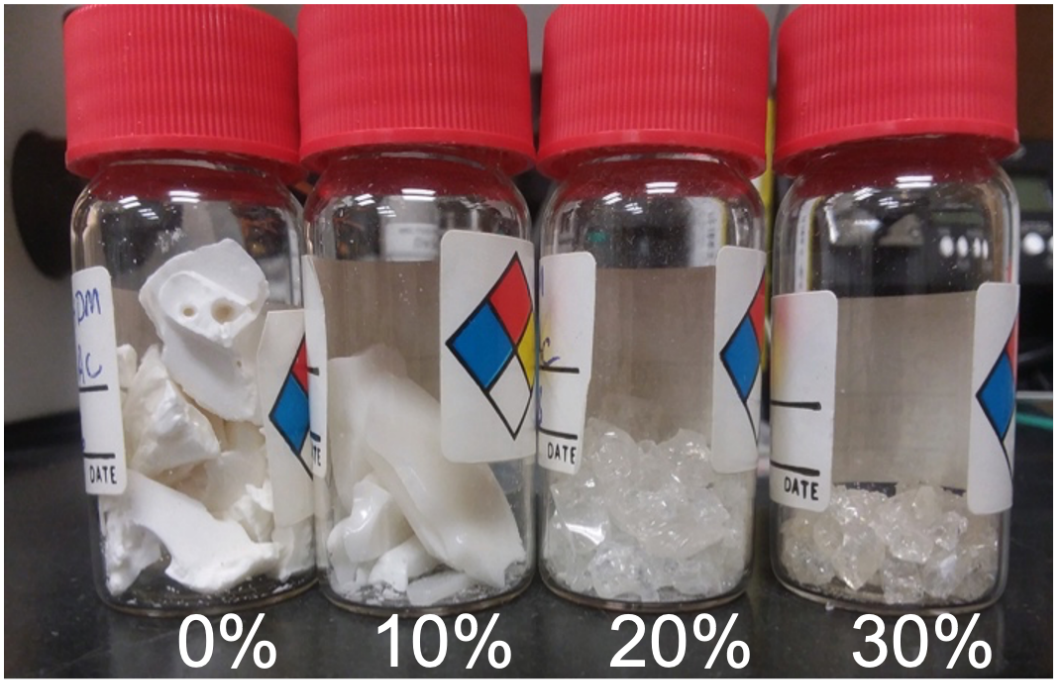


Figure 4.7: Samples of synthesized PEN with varying loading of CHDM-based copolymer. As the percentage of CHDM increases, the PEN material becomes more transparent, demonstrating fewer grain boundaries therefore decreased crystallization.

solvent commonly used for purifying organic reagents. Toluene is relatively volatile, allowing for any residual toluene in the DMN to be easily removed by vacuum distillation. Dimethylformamide is significantly less volatile and will oxidize during polycondensation if it remains in the reagents. Toluene can be used to remove any residual DMF and reduce discoloration during polycondensation.

4.4.2 Reagents

Dimethyl-2,6-naphthalenedicarboxylate (≥99%, Alfa Aesar) was recrystallized in dimethylformide (Sigma-Aldrich) and toluene (Sigma-Aldrich) then dried in a vacuum oven prior to use. Ethylene glycol (≥99%, Alfa Aesar) was distilled from a molecular sieve. 1,4-cyclohexane dimethanol (99%, Alfa Aesar) and magnesium acetate (≥99%, Sigma-Alrich) were used as received.

Germanium oxide (GeO_2) was prepared as a solution in ethylene glycol. GeO_2 was dissolved in deionized water at a concentration of 0.01 g/mL. Ethylene glycol was then added to the solution at a concentration of 0.01 g/mL to the GeO_2. The mixture was then heated to 100°C until the water had evaporated from the solution. The final concentration of the solution was 0.015 g/mL of GeO_2 in ethylene glycol.

4.4.3 Experimental Procedure

PEN is formed via a step-growth polycondensation that involves iterative transesterifications. During polycondensation, two molecules combine and result in the loss of a small molecule by-product. As the reagents are heated, the equilibrium is shifted towards polymerization by removing the small molecule by-product (as predicted by Le ChatelierâĂŹs principle). Details of how the synthesis was completed is outlined below.

Transesterfication

Transesterification was carried out in a 3-neck flask fitted with a Liebig condenser, overhead stirrer, and nitrogen gas port. Fiberglass insulated heating tape was coiled around the top

of the flask up to the neck of the condenser. A graduated receiver was used for collection of methanol. 10 g of DMN, ethyene glycol with an additional 20 mol% excess, CHDM at 30 mol%, and anhydrous magnesium acetate (3×10^{-3} mol mg / mol DMN) were added to the nitrogen purged reaction vessel and vacuum applied. Once $<$ 100 mTorr vacuum was achieved, the system was brought up to a slightly positive pressure of nitrogen with a flow rate of 50 $\pm$ 10 mL/min. The reaction flask was heated using a silicone oil bath with a temperature stability of ± 1°C. Transesterfication was performed at a temperature of 190 °C for 2 hours. Excess ethylene glycol was then removed by vacuum distillation.

Polycondensation

The same apparatus described above was used for the polycondensation reaction. The reaction flask, filled with the monomer bis-hydroxyethylenenaphthalate (BHEN), had 250 ppm of GeO_2 solution added to it, then heated to 150°C, with the melt sparged with argon for 1 hour. After sparging, the pressure was reduced to $<$ 50 mTorr and polycondensation was performed at a temperature of 270 °C for 2 hours. Once completed, the system was cooled to room temperature and brought up to a slightly positive pressure of nitrogen. An image of synthesized PEN can be seen in Fig. 4.8.

4.4.4 Properties of Synthesized PEN

Using the outlined method, we were able to successfully synthesize PEN with good optical properties. Collecting samples of successfully synthesized PEN however was difficult, as there was no way to extrude the material using a round bottom flask. Of the successful synthesized batches, we were able to collect enough material to create a sample for two different CHDM loading, CHDM at 20 mol% (Fig. 4.9) and CHDM at 30 mol%. The relative light yield was measured for these two samples and compared to the light yield of commercially available PEN. It was found that the light yield of the synthesized PEN was within error of the commercially available PEN pieces (Fig. 4.10).



Figure 4.8: Reaction flask after a successful PEN synthesis. PEN product can be seen coating the interior of the flask. At high molecular weight, it was difficult to remove the PEN material from the flask and therefore it was difficult to collect large enough samples to measure luminescent properties of PEN. In future, a pressurized reaction flask should be used for PEN synthesis to improve product collection.

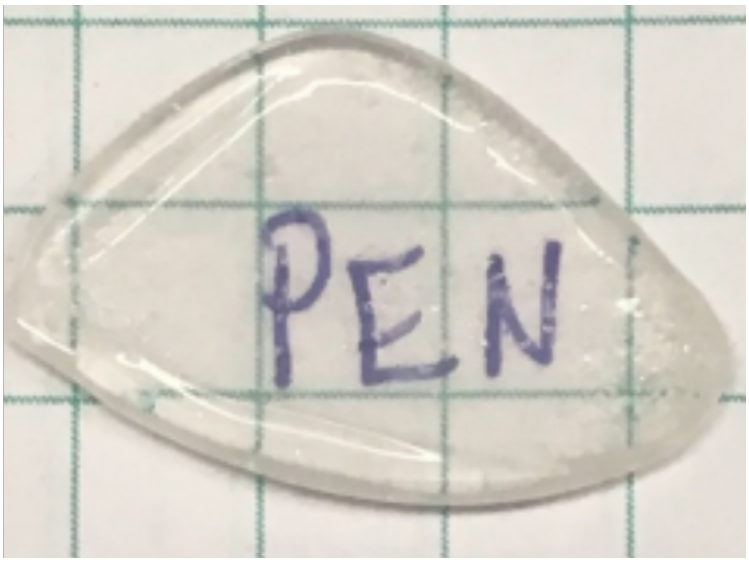


Figure 4.9: A synthesized PEN sample produced with 20% CHDM loading. This sample was used to measure the light yield of synthesized PEN in Fig. 4.8.

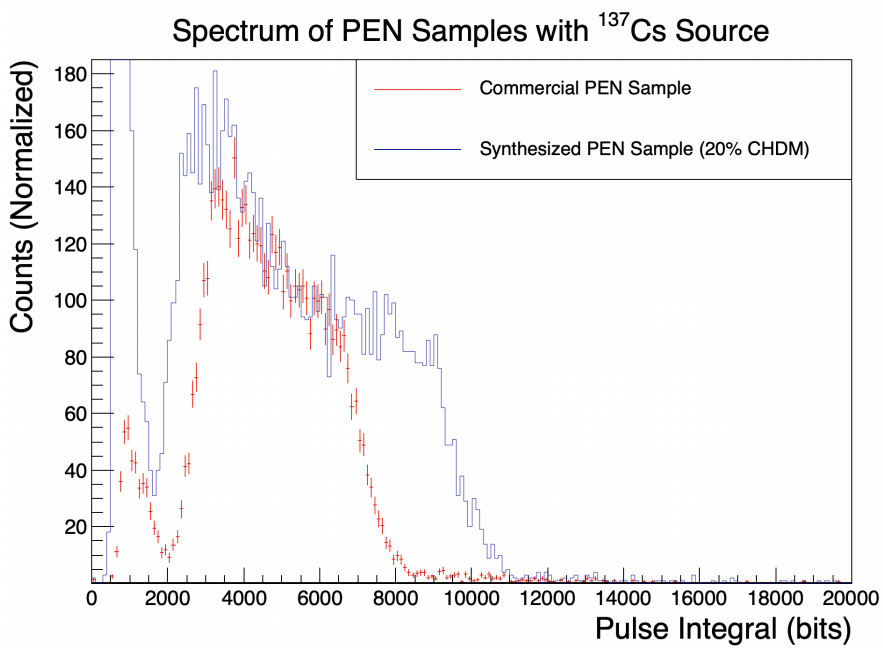


Figure 4.10: This is the light yield of two PEN samples, taken in the same geometry. The commercial PEN sample was a 1" circular coupon with a thickness of 1.5 mm. The Synthesized PEN sample has an area $\sim$ 1.6 times the area of the commercial PEN. This may explain the discrepancy in light yield.

As mentioned, PEN is semi-crystalline polymer and the degree of crystallinity can be partially controlled through rapid cooling. However, stress-induced crystallization and subsequent whitening can still occur in regions of high shear stress. However, the introduction of PECN as a copolymer with the addition of 1,4-cyclohexanedimethanol (CHDM) will yield non-crystalline polyesters [81]. A Differential Scanning Calorimeter (DSC) carefully measures the heat transfer of small samples on the order of milligrams with temperature. The results of the DSC are plotted in Fig. 4.11 of two amorphous samples I synthesized at ORNL and a commercial PEN sample. The PECT-PECN sample had 20 mol% copolymer and the PECN sample had 30 mol% copolymer. The samples were heated at a rate of $5°C/min$ across the glass transition temperature, crystallization temperature and the melting temperature. The commercial PEN sample has a clear peak at the crystallization temperature (265°C) where the enthalpy of crystallization is absorbed. Both synthesized samples, where the copolymer had been introduced, have no significant enthalpy of crystallization, suggesting a very long crystallization half life and an inherently amorphous polymer.

4.4.5 Radiopurity of PEN Reagents

The purification efficacy of each material was measured by the reduction of radio-impurities in the sample. The radio-impurities of the samples were measured by two methods, Neutron Activation Analysis (NAA) and Inductively Coupled Plasma Mass Spectrometry (ICP-MS). The specific activities of PEN reagents are listed in Table 4.3 for both NAA and ICP-MS.

Neutron Activation Analysis was performed at the University of Florida Training Reactor in Gainsville, Florida [82]. 10 gram samples were activated near the reactor core with a neutron flux of $1.8 \times 10^{12} cm^{-2} s^{-1}$ [82]. The activated samples were measured using a 1 kg Canberra HPGe detector in copper and lead shielding. The samples were measured 96 hours after irradiation. I conducted the analysis on the potassium and the bromine content and developed an online analysis tool to ensure the limits taken during measurements were well-understood. The bromine content of the samples was measured as a method of measuring salt and organic impurity reduction. In Table 4.3 the greatest reduction of bromine and

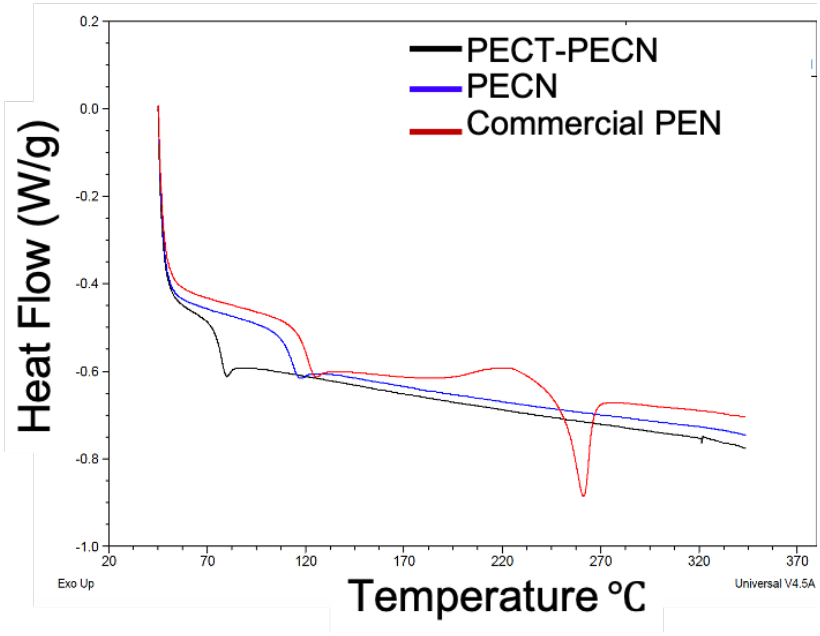


Figure 4.11: This thermogram shows the heat flow verses Temperature using a Differential Scanning Calorimeter. The peak at $265°C$ for PEN is the enthalpy of crystallization being absorbed. No such peak is seen in the other samples suggesting that there is no crystalline structure.

Table 4.3: The specific activity of different radio-impurities in PEN reagents. The ^{79}Br content is listed in nanograms per gram, providing an example of a measurable organic and inorganic salt that was removed from the DMN sample. The sample brackets describe whether the material is stock material or has been recrystallized in solvent. The radio-impurity brackets describe the method of measuring the sample.

Sample	ICP-MS [mBq/kg]			NAA [mBq/kg]	
	^{235}U	^{226}U	^{40}K	^{40}K	^{79}Br (ng/g)
DMN (Stock)	<9.5	<2.3	<580	<150	690± 40
DMN (Toluene)	N/A	N/A	N/A	<250	300± 10
DMN (DMF)	13.1	<2.3	<570	<7.9	37 ± 7
DMN (DMF and Tol.)	<9.8	<2.4	<560	N/A	N/A
CHDM (Stock)	105	<2.2	<570	N/A	N/A

potassium is recrystallization in DMF. The levels of bromine are reduced by a factor of 50 after recrystallization in DMF.

I prepared the samples for the ICP-MS analysis. The samples were recrystallized in stock dimethyl formamide (DMF) (Sigma Aldrich, CAS 68-12-2) and/or stock toluene (Sigma Aldrich, CAS 108-88-3). The DMN sample and solvent were heated in a glass volumetric flask on a hot plate until the DMN had dissolved. The magnetic stirrer bearing used to stir the material was cleaned by soaking it in 10% diluted nitric acid and rinsed with deionized water before use. The material was filtered using a stainless steel mesh, which was also cleaned by soaking in diluted nitric acid and rinsing with DI water. PTFE beakers cleaned using the same method, were used to store the DMN samples. While preparing the samples, I wore double set of clean gloves, a hair net and a face mask as well as a lab coat to try and minimize the risk of radio-contamination. It was noted that preparing these samples in a glass volumetric flask would introduce radio-impurities [83] and future measurements with better sensitivities should be carried out in quartz flasks.

4.4.6 Conclusions of Synthesized PEN

This synthesis was successful in producing small samples of amorphous PEN. The light yield was measured for the synthesized samples and found to be within error of the commercially available samples. Using this method however is limited to very small samples, which does not allow one to measure the mechanical properties of the material or produce enough to produce components to measure the full extent of the optical properties. As well, synthesis in glassware is convenient and inexpensive but will add radioimpurities to the sample [83]. To produce a sample where the radiopurity can be measured, the material must be synthesized in either acid-etched stainless-steel or quartz glassware.

For PEN to be synthesized on the scale required for ton-scale experiments, it would be necessary to involve a facility with industrial equipment that can produce batches $>$ 10kg as well as have the ability to replicate the same environment for each batch. With these increased batch sizes, more detailed analysis can be done on the effects of the structural

integrity and the light yield of the material as a function of PECN copolymer and with different synthesis methods. Finally by using industrial equipment we can use high vacuum stainless-steel reaction vessels. The improved vacuum from the reaction vessel will limit exposure to oxygen therefore improving color, limit the exposure of atmosphere therefore limiting radioimpurities and the melt will be in contact with stainless steel therefore reducing the exposure that is seen from glassware.

Note that for LEGEND-200, commercially available PEN was used. The synthesis method for this commercailly available PEN is outlined in Ref. [84] and was completed by Teonex.

Chapter 5

Studies of PEN as an Active Veto Material

In Ch. 4, it has been demonstrated that PEN meets the minimum requirements to be considered as a low background material for the LEGEND-200 Experiment by reaching an activity of $\sim \mu$Bq per part. In addition to PEN being considered a low background material, it is also being used as a structural component, and an active veto component. Therefore, the structural, optical, and luminescent properties must be characterized and considered when including this component and understanding its performance.

5.1 Structural Properties of PEN

The cryogenic behavior ($T < 125$ K [85]) of polyesters has been investigated thoroughly over the last 50 years, with various dynamic mechanical and stress strain measurements [86]. To understand the physical characteristics of a polymer at cryogenic temperatures, it is important to define the glass transition temperature, T_g. Amorphous polymers which show no evidence of crystalline behavior, will take on characteristics of a glassy-state like brittleness, stiffness and rigidity below their T_g after cooling [73]. For PEN, the T_g is significantly above cryogenic temperatures so the polymer will present some level of

brittleness, which is not ideal for a structural material. Polyesters are semi-crystalline, and therefore the degree of crystallinity will also have an effect on the structural integrity of the polymer.

Studies have demonstrated that the chemical and structural characteristics of commercial PEN and PET are very similar [87]. This is useful for applying previous research of PET to commercially available PEN. An in-depth study in 1969 of PET's structural characteristics at varying temperatures highlights what characteristics of PET most affect the structural integrity of the material [88]. The brittle stress was shown to be almost temperature and strain rate independent, whereas the yield behaviour is markedly sensitive to these parameters. Increasing crystallinity increases the yield stress and decreases the fracture stress. If the yield stress exceeds the fracture stress, the polymer will exhibit brittle behaviour, hence increased crystallinity will result in more brittle behavior.

The international PEN working group (a group I am an active member of) studied the structural properties of commercial PEN at both cryogenic and room temperature and compared to electroformed copper, another structural material in the LEGEND experiment [61]. The tensile strength (σ_{el}) and Young's Modulus (E) were measured using a three-point bending flexural test with accordance to the DIN EN ISO 178:2013-09 standard [89]. The tiles were machined out of an injection molded, amorphous commercial PEN to dimensions 15 x 30 x 3 mm. The results of the measurements and other published values for other materials in LEGEND are shown in Table 5.1. The Young's modulus is a description of how easily a material deforms. It is the ratio of a material's tensile stress ($\sigma = F/A$) to its tensile strain ($\epsilon = \delta l/l$). The results in Table 5.1 show that the PEN is more ductile than the copper samples, where the sample under extreme stress may deform but not break, potentially protecting the detector string from a catastrophic failure. The tensile strength is a better description of this, quantifying the amount of stress the material can withstand while being stretched, before it breaks. At cryogenic temperatures, PEN has a higher tensile strength than electroformed copper, supporting the proposal to use it as a structural material in cryogenic environments.

Table 5.1: This table shows the tensile strength, σ_{el} and the Young's modulus, E, for structural materials used in the LEGEND experiment.

	PTFE [90]	Copper [91]	EFCu [92]	PEN (RTP) [61]	PEN (77 K) [61]
σ_{el} $[MPa]$	<45.0	100	86 ±8	109 ±3	209 ±3
E [GPa]	<2.25	128	80 ±20	1.86 ±0.01	3.71 ±0.08

5.2 Optical Properties of PEN

One way to understand the efficacy of a component at vetoing background radiation would be to install it in a test setup and measure the scintillation light it produces, the amount that is detected and successfully vetoes this radiation. A direct method like this would be very useful but has limitations in the complexity that can be pursued. As well, it is unlikely to have the same levels of exposure that the LEGEND experiment will have. An alternative method of testing the efficacy of these components is to use simulations. Simulation packages, like Geant4, use Monte Carlo methods to randomly produce and track the passage of particles through matter. Using simulations like this, it is possible to understand how much light is produced in a component, and how much reaches the light readout system, like the WLS fibers. Therefore the likelihood of a decay being detected and vetoed in and around a component can be determined. This is a standard practice in nuclear and particle physics used during the design of a detector and its components. In order to accurately create a simulation, it is important to include all of the properties of the components so the transport of the particles can be accurately modeled. For active veto components, the optical properties will be of particular importance, as these directly impact how many photons are generated in the material and how they will propagate and be detected. A number of these properties have been measured as a part of the work of this thesis and are outlined in the following section.

5.2.1 Surface Reflectivity

The parameter σ_α used in GEANT4 simulations describes the roughness of a surface and therefore the way in which light reflects off the surface [93]. For example, if a photon is incident on a diffuse reflector at ϕ_β to the surface, the photon can reflect at all other angles, $\phi_\gamma \leq \pi$ ($\sigma_\alpha >> 0.5$). A specular reflector however, will reflect an incident photon at the incident angle, i.e. $\phi_\beta = \phi_\gamma$ ($\sigma_\alpha \leq 0.3$).

To measure the reflectivity of the PEN baseplate surface, a tool was designed and built to accurately measure the incident angle, ϕ_β and the measurement angle, ϕ_γ. Pins were

used on a calibrated pin wheel to fix ϕ_β and ϕ_γ. The accuracy of ϕ_γ was further improved by using a "General Tools and Instruments Digital T-Bevel". The light source was a laser diode, with $\lambda = 513$ nm, mounted to a Thorlabs Laser Diode Mount with Integrated TEC and Controller. The readout of the light was a Compact CCD Spectrometer with a read-in of a fiber cable and a lens mounted at angle ϕ_γ. To avoid reflections on the back surface of the PEN baseplate, the back was painted with matte black paint. A diagram of the tool and an image of the setup is shown in Fig. 5.1 and Fig. 5.2.

The intensity of reflected light for a given angle was fit with a Gaussian distribution, and σ_α was estimated to be the standard deviation, σ, derived from the Gaussian fit. The sensitivity of the instrument and measurement method was determined by using a mirror, placed on top of the PEN baseplate. These calibrations showed a minimum sensitivity of $\sigma_\alpha = 0.40°$. The average of the measurements taken at a series of angles produced a final value derived was $\sigma_\alpha = 0.46 \pm 0.07°$, which is in agreement with the mirror like quality of the surface. A plot of the data can be seen in Fig. 5.3.

5.2.2 Attenuation Length Measurements

Understanding how light is propagated through the bulk of a material is important for optical simulations of a material and for bench-marking the performance of the bulk as a scintillator. A standard used for defining this property is the attenuation length (λ), or the distance light of a certain wavelength can travel through a medium, before its intensity decays by $1/e$. The attenuation length and transmission are defined by Eq. 5.1 and Eq 5.2, where l is the length the light travels in the medium, I is the transmitted intensity and I_0 is the incident intensity.

$$\lambda = -\frac{l}{ln(T)} \tag{5.1}$$

$$T = \frac{I}{I_0} \tag{5.2}$$

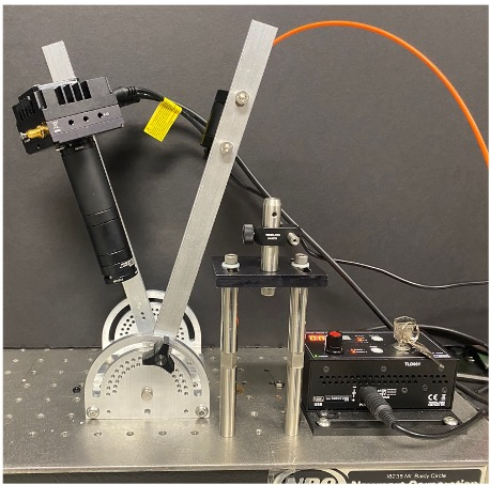


Figure 5.1: This is an image of the reflectivity tool setup. The laser, $\lambda = 513$ nm, is focused on the surface of a PEN baseplate and the reflected light is being read out using a Thorlabs spectrophotometer.

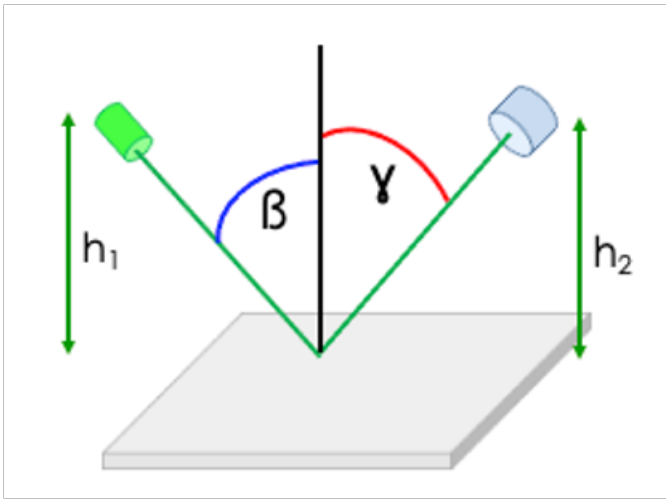


Figure 5.2: Diagram of the reflectivity tool setup.

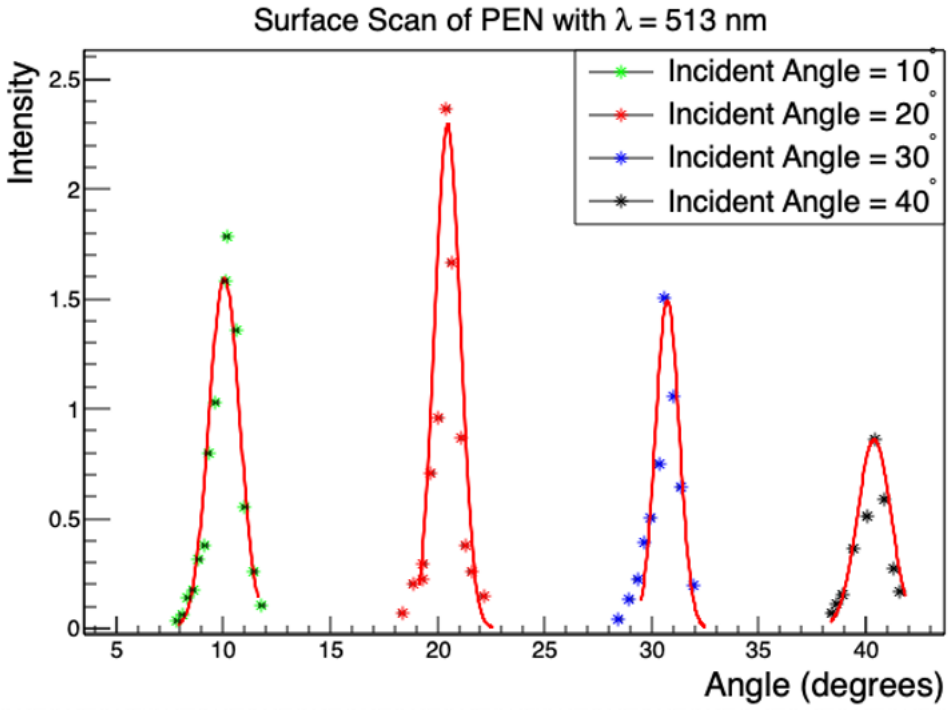


Figure 5.3: Plot of the results of the reflectivity measurements, measuring the light intensity at angle ϕ_γ at a series of incident angles, ϕ_β.

The attenuation length was measured using a Shimadzu UV-2700i UV-Vis Spectrophotometer. This instrument is a double beam, double monochromator spectrophotometer with a bandwidth of sub-nanometers and sensitivity to light in the 200 to 800 nm (Fig. 5.4). The double beam measures the transmission of the sample and the reference simultaneously, normalizing the intensity of the light source and improving the sensitivity of the instrument.

PEN pieces were machined to fit perfectly into a BrandTech Macro UV-Cuvette and were slotted into a black bottom and top fitting, designed to keep the face of the PEN plates parallel to the cuvette face, as well as create a standard position. Measurements were taken with both one and two pieces of PEN to check the efficacy of the measurement and check for consistency. An image of the slots are shown in Fig. 5.5. These slot pieces were machined from black plastic, to ensure no interference with the measurement and the reference liquid. The cuvette was then filled with ethanol as the reference liquid. Ethanol was selected as it was chemically compatible with the cuvette material, the PEN plastic and the slot pieces. In addition, ethanol has an index of refraction ($R_{Ethanol} = 1.36$) closer to the index of refraction of PEN ($R_{PEN} = 1.64$). The ethanol used was from Sigma Aldrich, HPLC Spectroscopic grade.

A factor to consider when using plastic pieces submerged in liquid is the loss of light from changing refractive index, that would not be seen in the reference sample. Without taking this loss of light into consideration, the attenuation length would have a systematic error and be artificially lower. To predict this loss of light, optical simulations were conducted in Geant4 [94]. These simulations used varied index of refraction for the ethanol, PEN and BrandTech cuvette (proprietary material). A circular light source with a radius of 3 mm was directed at a cuvette filled with either ethanol, ethanol and one PEN piece, or ethanol and two PEN pieces and ran 20,000 photons. The sensitive detector used in the simulation was a multi-pixel photon counter (MPPC) with a radius of 5 mm. In the simulation, it was assumed that the PEN, cuvette and ethanol had infinite attenuation length. This is so that any loss of light seen in the simulation was due to reflections, not due to attenuation. A rendering of this simulation is shown in Fig. 5.6. The factor, or fraction of light lost due to changing refractive index was determined by Eq. 5.3:

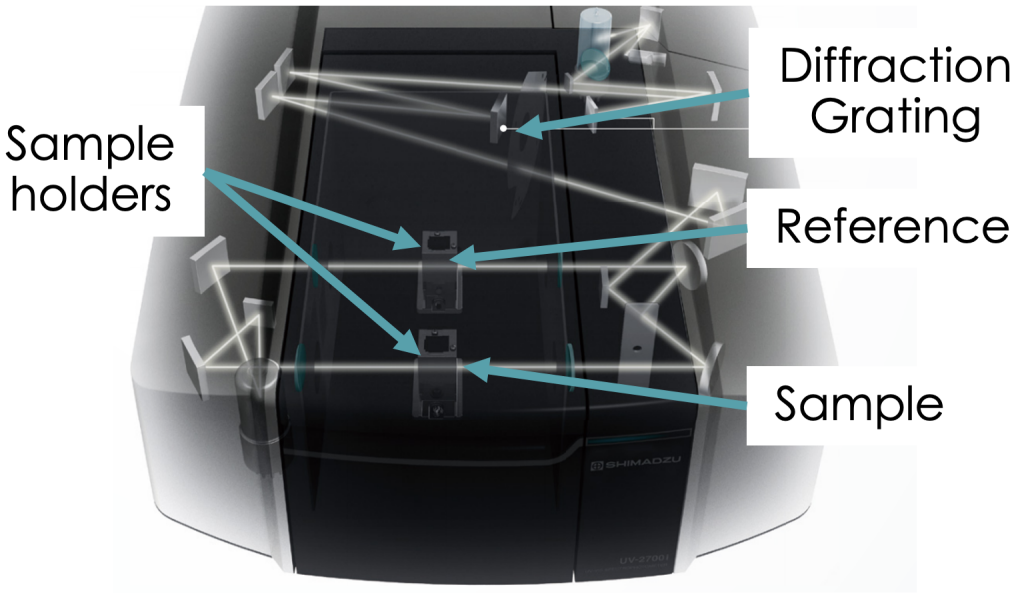


Figure 5.4: Diagram of the dual beam Shimadzu UV-2700i UV-Vis Spectrophotometer and how the light is propagated through the device.

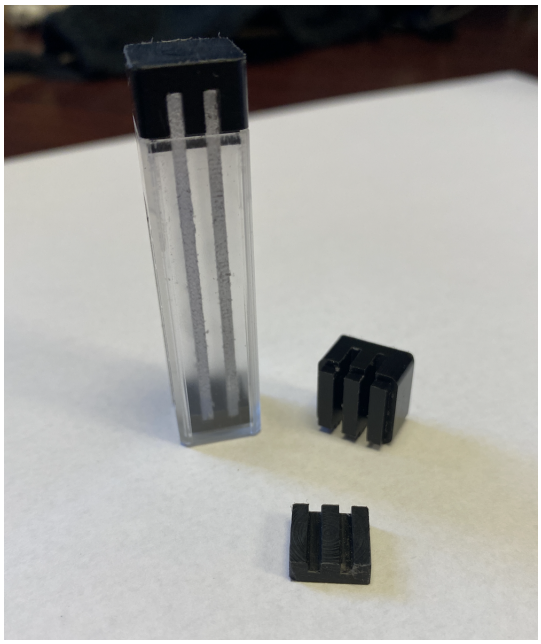


Figure 5.5: PEN pieces inserted into cuvette (on left) and black slot machines to fix PEN pieces(on right). Slot pieces were used in both the sample cuvette and the reference cuvette to ensure consistency.

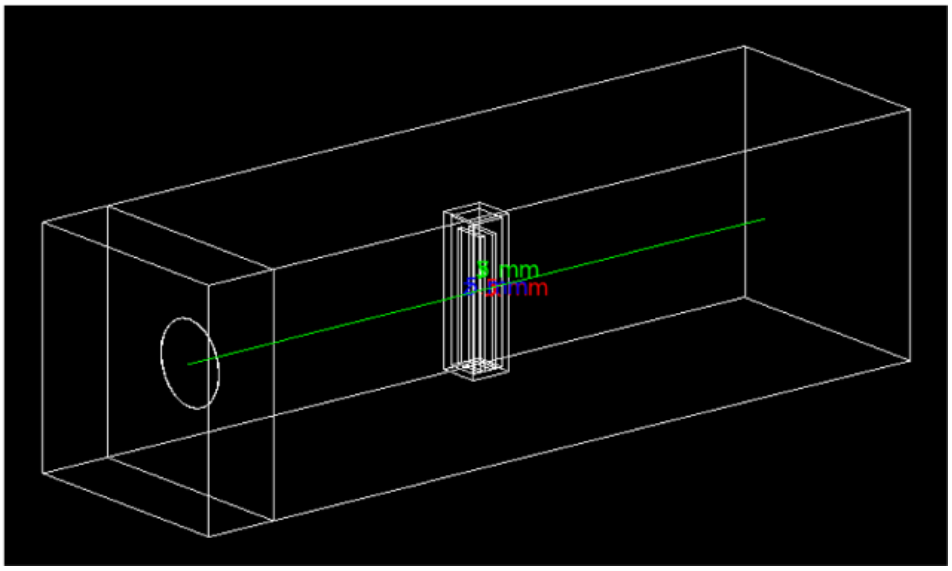


Figure 5.6: Rendering of optical simulation in Geant4, measuring the number of reflected photons as a result of changing index of refraction through the cuvette.

$$f_{PEN} = \frac{T_{PEN\ in\ ethanol}}{T_{ethanol}}. \tag{5.3}$$

The factors were determined for a number of wavelengths, and then fit with a polynomial. This function was fed into attenuation length calculations to take this effect into account. A table of these values is shown in Table 5.2.

Another factor that will impact the transmission of light through the PEN tiles is the quality of the surface of the material. PEN pieces are produced with optical finishes [67], however during handling and machining scratches can occur on the surface. These scratches will have a negative effect on the attenuation length, so to determine the true bulk attenuation pieces with optimal surface quality should be used. The two tiles used for these measurements, tiles A and B, are shown in Fig. 5.7 and Fig. 5.8.

The results of these measurements after the correction for reflections are shown in Fig. 5.9. A previously polished tile is shown in green, with significantly worse attenuation. This highlights that it is not possible to polish the surface of a PEN piece and return it to its previous surface quality. Care should be taken to ensure during installation of PEN into LEGEND-200 there is no damage done to the surface of the PEN pieces. The measurements agree well with each other, and it can be seen that tile A has slightly superior optical properties. These measurements will be used in Geant4 for LEGEND optical simulations. I would also like to mention that similar values for attenuation length were measured by collaborators at Max Plank Institute in Munich, Germany [95].

5.3 Wavelength Shifting Properties of PEN

As previously described, PEN has the ability to wavelength shift light in the VUV and soft UV range, to its peak emission at 450 nm. In a LAr environment, the wavelength shifting efficiency of PEN will have a strong effect on the overall efficacy of the LAr scintillation light detection efficiency. This is because LAr is approximately ten times brighter than PEN, but its photons (λ = 128 nm) can only be detected after being shifted, so by increasing

Table 5.2: Table of fraction values, determined by observing the transparency of a cuvette filled with PEN and ethanol versus a cuvette filled with only ethanol, using a Geant4 optical simulation.

Wavelength (nm)	Fraction (1 tile)	Fraction (2 tiles)
430	0.982	0.964
450	0.983	0.966
500	0.984	0.968
540	0.985	0.969
620	0.986	0.970

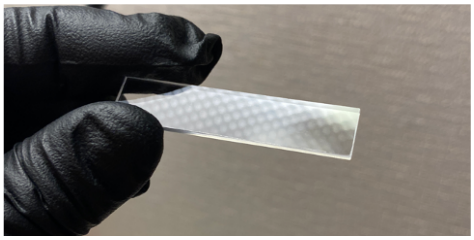


Figure 5.7: Image of PEN tile A.

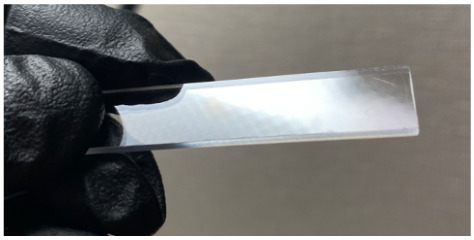


Figure 5.8: Image of PEN tile B.

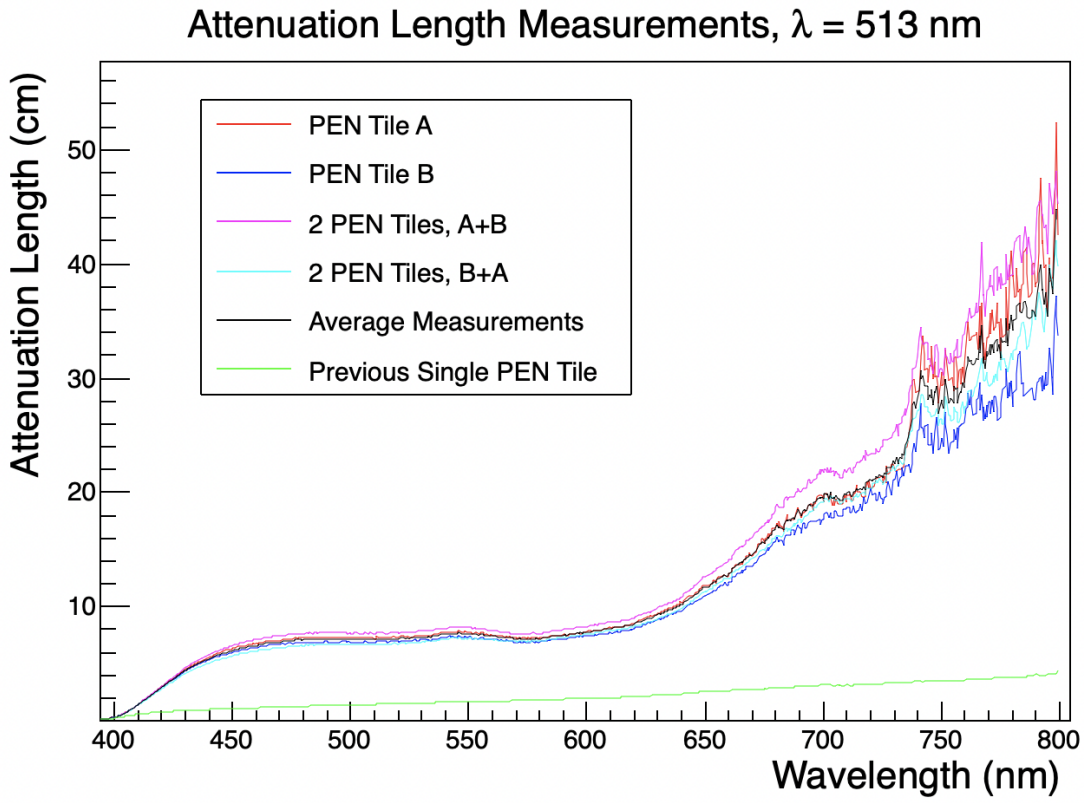


Figure 5.9: Results of attenuation length measurements. Measurements have good agreement with each other, and have improved optical quality compared to the previous PEN piece which was polished.

the surface area that can shift LAr light, the overall active veto system improves in its effectiveness.

This section focuses on environmental effects that could possibly alter these results.

5.3.1 WLS Effects of Cleaning PEN Components

Before components can be installed in a low background detector, it is common that they are cleaned to remove any surface contamination. The cleaning procedure developed by the MJD includes three different solvents; deionized water, 2% diluted Micro-90 with 98% 18 MΩ water, and 10% diluted American Chemical Society (ACS) grade nitric acid with 90% 18 MΩ water [83]. Although considered unlikely, it was unclear how these cleaning solutions would affect the surface and wavelength shifting characteristics of the PEN plates. To test this, 1" PEN tiles were machined out of the large PEN disks produced during the production run. Each tile was immersed in one of the previously listed solvents and left to soak for 7 days. Afterwards, the tiles were rinsed with deionized water and carefully packaged to prevent any surface contact. One tile was not immersed in any solutions and used as a control.

In Section 4.3, it was demonstrated that PEN is capable of wavelength shifting into the soft UV range. The soft UV range is ideal for testing wavelength shifting as air does not strongly attenuate soft UV light, yet soft UV light is still a significantly shorter wavelength than PEN's emission spectrum. I tested the wavelength shifting efficiency of each of the tiles by illuminating them with a high power LED at 340 nm. A Thorlabs Compact CCD Spectrometer was then used to collect and measure the shifted light at 450 nm. Fig. 5.10 is an example excitation and emission spectrum measured by the spectrophotometer. Fig. 5.11 is a bar chart illustrating the intensity of the shifted light and respective error at 1σ. From this figure, it is clear that the intensity of the shifted light is all within the same error. Therefore, post-production cleaning of the plates does not appear to effect the wavelength shifting efficiency.

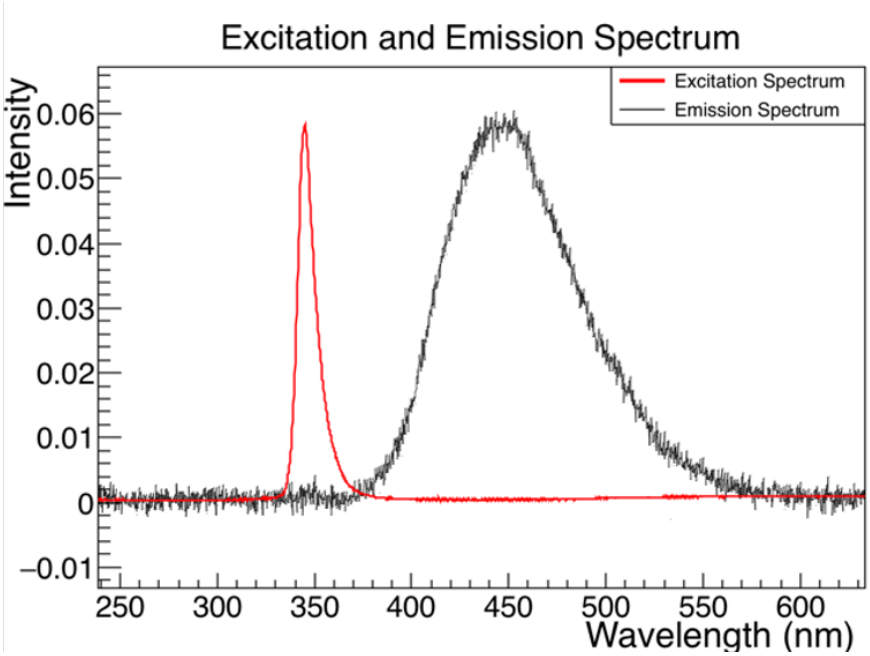


Figure 5.10: Excitation and emission spectrum of wavelength shifting set up.

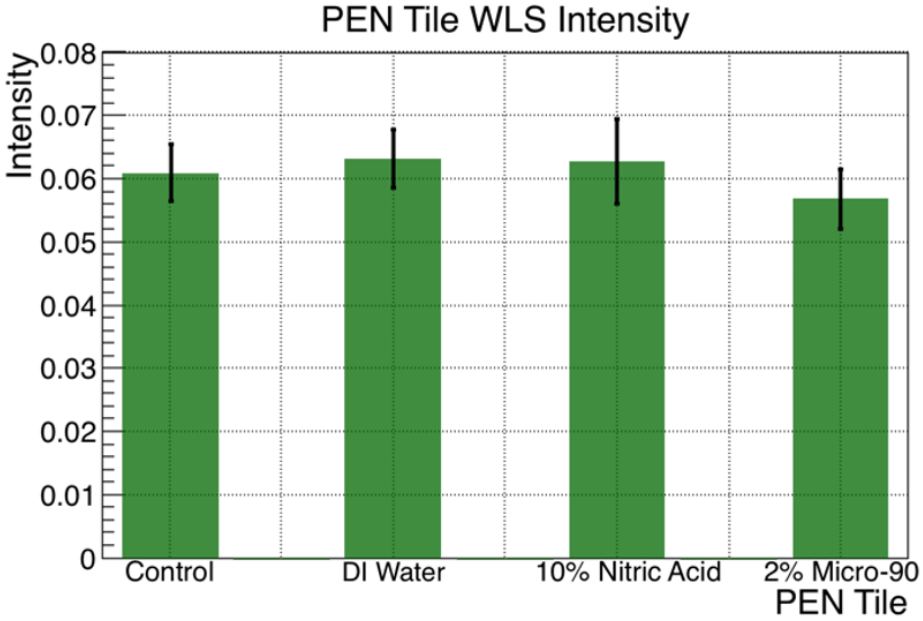


Figure 5.11: Relative intensity of wavelength shifted light by the different tiles, with each of their cleaning procedure.

5.4 Light Response of PEN to Neutrons

This section is reproduced from Brennan Hackett et al [96]. Some parts of the paper have been edited to better fit with the thesis presented, while some parts of the paper remain unchanged.

Radioluminescent properties of PEN have been measured to aid in the evaluation of this material. In this section I present a measurement of PEN's quenching factor for neutrons using three different neutron sources; neutrons emitted from spontaneous fission in ^{252}Cf , neutrons generated from a DD generator, and neutrons emitted from the ^{13}C(α,n)^{16}O and the ^{7}Li(p,n)^{7}Be nuclear reactions. The fission source used time-of-flight to determine the neutron energy, and the neutron energy from the nuclear reactions was defined using thin targets and reaction kinematics.

The light response for PEN has been measured for alpha particles [97], but never for neutron interactions. Quenching in scintillators is defined by considering the light produced by a nuclear recoil, $L(E)_{nr}$ as a fraction of the light produced by an electronic recoil of equivalent energy, $L(E)_{er}$

$$QF(E) = \frac{L(E)_{nr}}{L(E)_{er}}. \tag{5.4}$$

There are many models to describe how the light is quenched as a function of energy in a scintillator [98]. This chapter will focus on the use of Birk's law:

$$\frac{dL}{dr} = S\frac{\frac{dE}{dr}}{1 + kB\frac{dE}{dr}}. \tag{5.5}$$

Birk's law describes how the light per unit length, $\frac{dL}{dr}$, is quenched as a function of stopping power, $\frac{dE}{dr}$. The scintillation efficiency S, and the Birk's constant, kB, describes the shape of the light response curve, and to what degree it is non-linear as a function of energy deposition by the neutron.

To determine the quenching factors and determine the Birk's parameters, it is necessary to determine which measured events are from neutron recoils on nuclei and which are from γ-ray interactions with electrons. One tool used for this is pulse shape discrimination (PSD) as it allows the distinction between particles with different charge/mass ratios, such as electron and proton recoils. Fig. 5.12 defines the pulse shape discrimination parameter as the fraction of the integral of the light pulse tail compared to the integral of the whole light pulse from the detector.

This is the result of the population of different singlet and triplet excited states by electron and nuclear recoils. The decay of the singlet excitation is an allowed transition and will therefore immediately decay (prompt fluorescence). Triplet excitations can radiatively decay via a forbidden decay (phosphorescence), suppressed, or by annihilating with another triplet state resulting in a ground state and another singlet excited state - which then decays immediately (delayed fluorescence). This results in scintillators fluorescing on two time scales, prompt fluorescence from first excited state decays, and delayed fluorescence as a result of triplet-triplet annihilation (TTA). For beta and photon interactions that result in electronic recoils, the energy deposition per unit length over the particle track is relatively small. Therefore these interactions result in a low density of triplet state excitations and therefore will have a low portion of light produced from delayed fluorescence. On the other hand, nuclear interactions, such as neutron, proton and alpha interactions, result in proton recoils. These heavily ionizing particles result in larger energy deposition in a very short track, resulting in a much higher density of triplet state excitations. This increases the likelihood of a triplet state annihilating with another triplet state, increasing the ratio of delayed fluorescence to prompt fluorescence compared to an electronic recoil. Therefore, there will be a greater portion of light in the tail of the pulse for proton recoils, it is possible to discriminate between electron and proton recoils with the PSD parameter. Examples of average light pulses at 0.6 MeVee are shown for PEN are shown in Fig. 5.12.

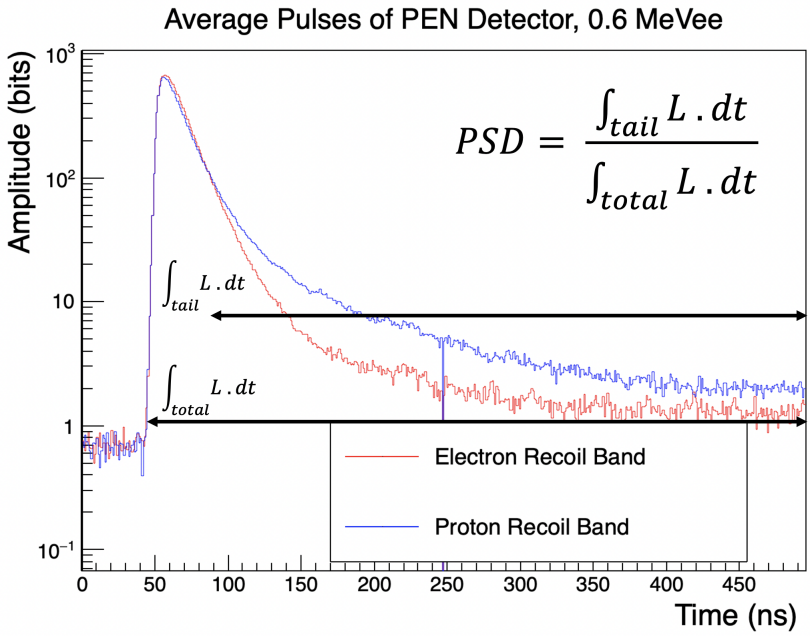


Figure 5.12: Average pulses in PEN for electron and proton recoils for 100 pulses. Pulse energies are approximately 0.6 MeVee.

5.4.1 PEN scintillation detector

The PEN component used for this measurement is an amorphous sample produced by an injection molding process described in Ref. [61]. The commercially available PEN used to produce this component was supplied by Teonex, TN-8065S. The PEN component is 5.08 cm in diameter and 0.5 cm thick (Fig. 5.13).

The detector consisted of three main components; a 3D printed cap to hold the PEN component and optically seal the detector, the PEN component itself, and a photomultiplier tube (PMT). For the measurement conducted using nuclear reaction neutrons, a Hamamatsu R6233 2" PMT was used. This tube is a hybrid design with box-and-grid technology to maximize light collection, and linear focused technology to improve pulse linearity [99]. For the measurement conducted using spontaneous fission neutrons, a Hamamatsu R7224 2" PMT was used. This tube has a linear focused design, with a smaller transient time spread and larger gain, resulting in a lower light threshold and improved time resolution, and therefore energy resolution. The same detector used for the fission chamber measurement was used in the DD generator measurement. Both detectors were lined with Teflon which serves as the optical reflector, and the component was optically coupled to the face of the PMT using Saint Gobain optical coupling compound, BC-630.

5.4.2 Experimental Method

The experimental method was as follows; $L(E)_{er}$ was calibrated for each detector with gamma-ray sources. Next, the energy of the neutrons are determined using reaction kinematics or time-of-flight. Finally, the quenching factor is determined by measuring the light produced for a proton recoil of a given neutron energy, $L(E)_{pr}$.

Detector Calibration

Gamma-ray radiation sources were used to calibrate the PEN scintillation detector in each measurement. The gamma-ray energies from these sources have an energy range $0.356 < E_\gamma < 1.332$ MeV. The gamma-ray source response in the PEN scintillation detector was

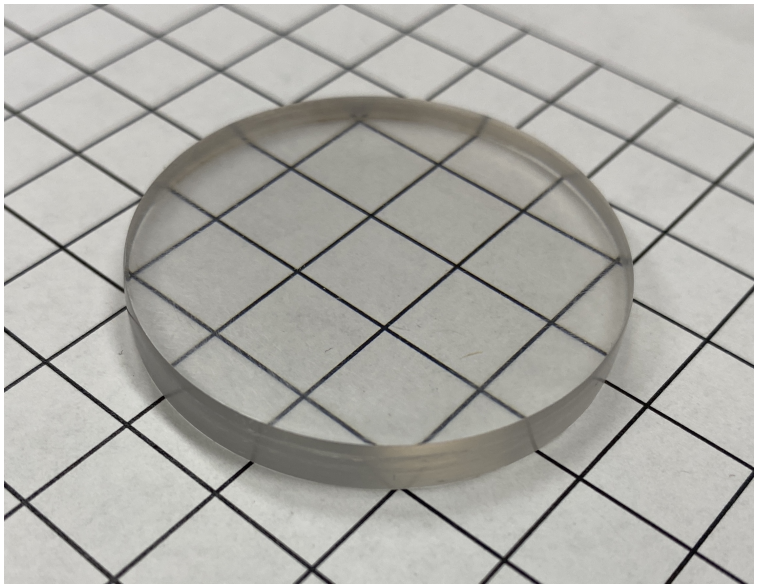


Figure 5.13: The PEN component used for these luminescent measurements has a radius of 5.08 cm and a thickness of 0.5 cm.

simulated in Geant4, and the energy deposited by recoiling electrons in the PEN component was recorded. The experimental resolution of the data was recreated in the simulation data using Gaussian smearing with the resolution defined by Eq. 5.6, and the inverse error function as described in Eq. 5.7:

$$FWHM = E * \sqrt{\alpha^2 + \frac{\beta^2}{E}} \tag{5.6}$$

$$E' = (E + erf^{-1}(r) * \sqrt{2\left(\frac{FWHM}{2.35}\right)^2}) * C. \tag{5.7}$$

To determine the optimal α and β parameters, first a Gaussian function is fit to the Compton edge in the data:

$$f(x) = k * exp^{-\frac{1}{2}\left(\frac{x-\mu}{\sigma}\right)^2}. \tag{5.8}$$

The initial values for μ and σ were estimated in the Gaussian function (Eq. 5.8) and then fit to the simulation. The simulation is multiplied by a scaling factor, C, to reproduce the simulation on the same scale as the data, which is in arbitrary units. An iterative method was applied to find optimal parameters for α, β, and C. A minimum χ^2 is found between the fit function and smeared simulated deposited energy spectrum, and used to quantify the goodness of the fit.

Figure 5.14 shows an example of a best fit for a ^{137}Cs source in comparison with the data. Figure 5.15 plots the resolution of the calibration sources as a function of energy. The simulation was smeared with the following values; $\alpha = 0.053$, $\beta = 0.12$ and $C = 8020$. The same α and β parameters were then used to Gaussian smear the neutron simulations to determine the neutron edge.

Calibration of Neutron Sources and Experimental Setup

Any single neutron source measurement could result in systematic errors in the measured light response, and would be limited in its energy range. However, by measuring the

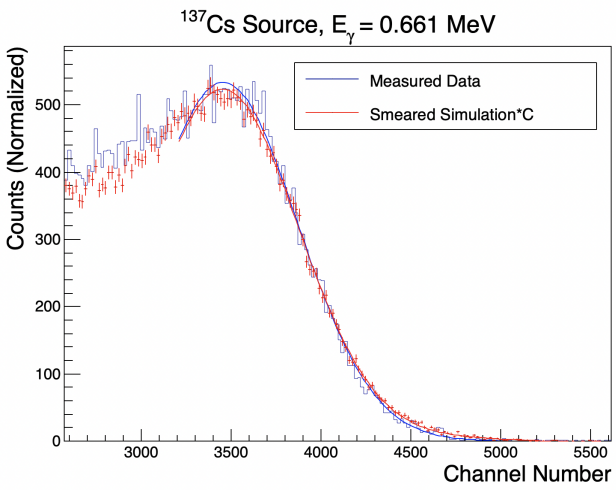


Figure 5.14: Measured data of a ^{137}Cs source with $E_\gamma = 0.661MeV$, impinging on a PEN scintillation detector. The simulation with the following values; $\alpha = 0.053$, $\beta = 0.12$ and $C = 8020$.

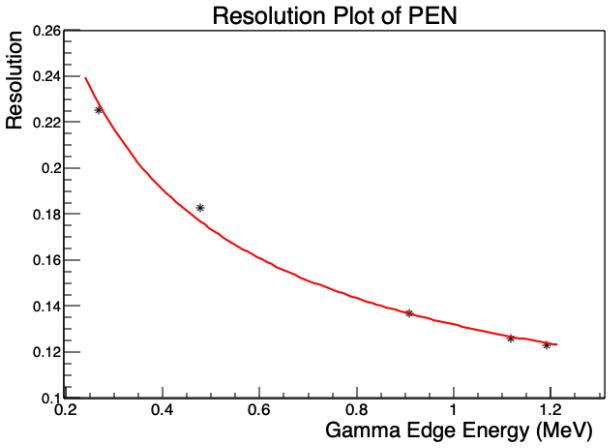


Figure 5.15: The detector energy resolution was measured using various gamma-ray sources. This plot shows the detector resolution for the detector used at the University of Notre Dame for the nuclear reaction neutron sources.

luminescent response of PEN using multiple neutron sources, as well as using different light collection systems and data acquisition systems, agreement between measurements will reduce the likelihood of global systematic errors. Therefore three different types of neutron sources were used; a white ^{252}Cf neutron source with time-of-flight, monoenergetic neutrons from a DD generator, and monoenergetic neutrons produced from the ^{13}C(α,n)^{16}O and ^{7}Li(p,n)^{7}Be reactions using monoenergetic particle beams, made incident on thin targets where the beam experienced very small energy losses. There are different methods used to determine the neutron energies between these three measurements. The first is time of flight, where the flight time, T of a neutron can be used to determine its kinetic energy from a white neutron source. The neutron's energy and its uncertainty can be found using:

$$E_n = \frac{1}{2} m_n \left(\frac{D}{T}\right)^2 \tag{5.9}$$

$$\Delta E_n = 2\sqrt{\left(\frac{\Delta D^2}{D} + \frac{\Delta T^2}{T}\right)}. \tag{5.10}$$

The energy resolution of this measurement is defined by the uncertainty in the time and distance. It is possible to increase the flight path to improve the energy resolution, but this comes at the cost of statistics or run time. Similarly, as the neutron energy increases, its time-of-flight decreases, therefore resulting in a decrease in energy resolution. This places an upper limit on the energies that can be reasonably measured using time-of-flight.

The second method used to determine the energy of the neutron is to use reaction kinematics. Neutrons produced in two-body nuclear reactions will have a well defined energy depending on the beam bombarding energy and the angle of emission, with an energy uncertainty determined by the solid angle acceptance, energy loss through the target and fluctuation in the beam energy. Both the beam energy fluctuations and the energy loss through the target were determined to be negligible. However, there is the potential for other reaction channels, resulting in other reaction products, producing a large number of background events. With these background events, it becomes increasingly difficult to distinguish low energy neutron events. PSD also becomes more difficult at lower energies as

it becomes more difficult to distinguish an electron and proton recoil. This has limited the ability to measure neutrons at energies less than than ≈0.7 MeV.

^{252}Cf Spontaneous Fission Source For this measurement, ^{252}Cf was used as a white neutron source. The non-relativistic kinetic energy of the neutrons was determined using time-of-flight from the source to the detector. Neutrons are produced by spontaneous fission in ^{252}Cf . When a fission spontaneously occurs, both neutrons and photons are released. The ^{252}Cf source is within a small fission chamber, which will trigger on fissile fragments passing through an ion chamber, and therefore will set a start time for the event [100]. A diagram of the fission chamber can be seen in Fig. 5.16. The ^{252}Cf source is plated on a platinum disk and is set parallel to the signal collector. The ^{252}Cf source and signal collector are set in a hemispherical ionization chamber filled with a mixture of 97% Ar and 3% CO_2 gas. There is a bias voltage applied between the disk and signal collecting electrode to ensure there is a trigger when a fission occurs.

The trigger from the ionization chamber is fed into a CAEN desktop digitizer model 5730, and coincidence is required between the fission chamber and PEN scintillation detector to record the event. The trigger time was defined by using the CAEN onboard Leading Edge Discriminator, or LED [101]. Using an LED may result in edge walking for varying pulse amplitudes, or shifting of the start time with pulse height, but this was not a concern for the fission chamber pulses, as the rise time was faster than the digitizer sampling speed. The PEN scintillation detector had pulses with significantly slower rise times, therefore on board CFD (constant fraction discriminator), triggering at 50% amplitude, was used to determine the start time of the pulse. Unlike LED, which uses a trigger amplitude to define the start time for a pulse, the CFD shapes the pulse and defines the start time when the pulse height is at 50% of its maximum amplitude.

The distance between the fission chamber and the PEN scintillation detector was measured to be $d = 0.890 \pm 0.005$ m. The gamma flash in PEN was centered at $\delta T = 2.8$ ns, with a resolution of $FWHM = 2.3$ ns (Fig. 5.17). This resolution was used to determine the neutron energy resolution, as shown in Eq. 5.10. This is very close to the resolution of

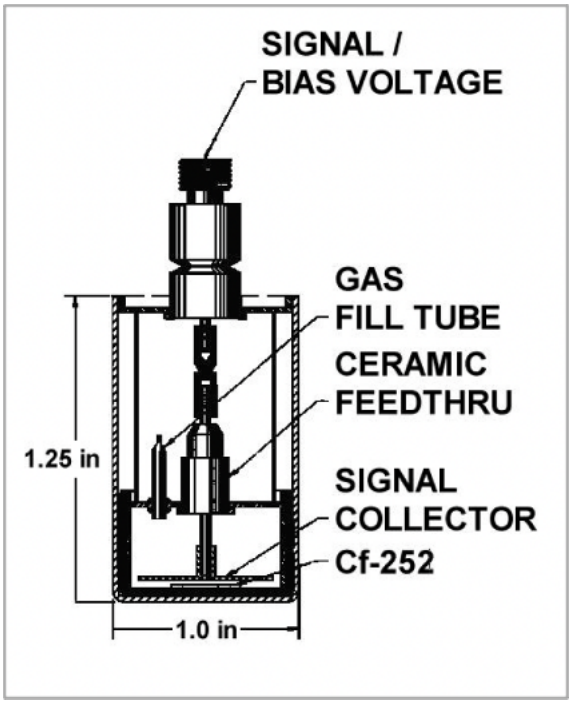


Figure 5.16: Schematic of the ^{252}Cf Parallel Plate Ionization Chamber [100].

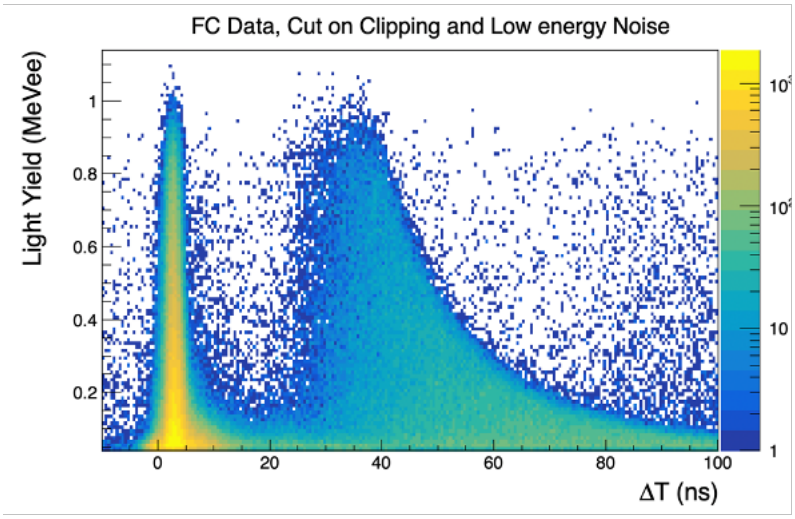


Figure 5.17: The time of flight was used to determine the energy of neutrons from the ^{252}Cf source. This plot shows the time of flight or δT for events from the fission chamber to the PEN scintillation detector versus the light yield for that event. The gamma flash can be seen focused around ~ 3 ns.

channel-to-channel timing using the onboard CAEN DPP-PSD firmware ($\sim$ 2.2 ns) [101]. The total pulse was integrated over 430 ns, with the short integral starting at an offset of 70 ns from the peak amplitude of the pulse. The pulse shape discrimination parameter, described in Fig. 5.12 was defined by using the ratio of the total pulse and the short integral (Fig. 5.18). Averages of PEN scintillation pulses for the electronic and nuclear recoils are shown in Fig. 5.12.

Using a similar technique that was used for the gamma calibration of the PEN scintillation detectors, the energy deposited by recoiling protons in a PEN component was simulated using Geant4. The simulation is smeared using the same smearing function as shown in Eq. 5.7, with the resolution (FWHM) being defined by Eq. 5.6.

Energy deposited by neutrons in hydrogen-based scintillators has a step shape, that can be fit with a sigmoid function:

$$f(x) = \frac{p_0}{1 + e^{-p_1(x-p_2)} + x * p_3}. \tag{5.11}$$

This sigmoid function was fit to the data, to determine the parameters p_1 and p_2. With these parameters fixed, and p_0 and p_3 allowed to float, the sigmoid function was then fit to the simulation. The simulation was scaled by a "quenching factor" or QF. The χ^2 for this fit was minimized by varying the QF. The accuracy of the quenching factor was defined by the variation of the QF as the χ^2 per degrees of freedom, or $\Delta\frac{\chi^2}{DOF} = \pm 2$.

The width of the energy step for the fission chamber measurements was determined by the timing resolution of the experiment, or the FWHM of the gamma pulse. This is equivalent to a FWHM resolution of 36 keV for a 1 MeV neutron. The energy steps for neutrons had a range that was larger or equivalent to the energy resolution from the timing. The range of neutron energies measured from the ^{252}Cf source was $0.5 < E_n < 2.0$ MeV.

DD Generator A DD generator uses the fusion of deuterium to produce neutrons, as described in Eq. 5.12:

$$^2H +^2 H \rightarrow n +^3 He. \tag{5.12}$$

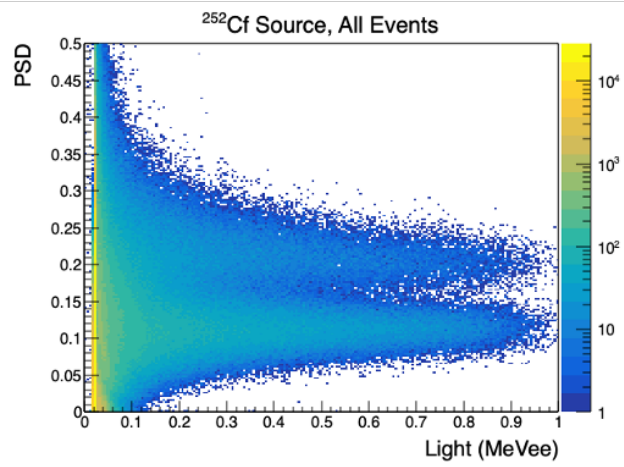


Figure 5.18: This plot shows the PSD for the PEN scintillation detector used in the fission chamber measurements. The neutron events and therefore proton recoils can be seen in the top band and the gamma events and therefore electronic recoils can be see in the bottom band.

This reaction releases monoenergetic neutrons, at $E_n = 2.45$ MeV [102]. Because this source is monoenergetic, time-of-flight was not needed to determine the energy of the neutrons. The data was collected on the same CAEN 5730 desktop digitizer used in the ^{252}Cf fission source measurements. The total pulse was integrated over 430 ns, with the short integral starting at an offset of 70 ns from the peak amplitude of the pulse.

The data for the DD measurement was also fit with the sigmoid function (Eq. 5.11). These simulations were generated in Geant4, and the energy deposited on protons from 2.45 MeV neutrons was recorded. The simulation was then smeared as described in Eq. 5.7, and the data and smeared simulation are plotted in Fig. 5.19.

Nuclear Reaction Neutrons The nuclear reactions used in these measurements were ^{7}Li(p,n)^{7}Be and ^{13}C(α,n)^{16}O and were conducted at the University of Notre Dame Nuclear Science Laboratory. The Sta. ANA 5 MV accelerator was used to produce a beam of $^{1}H^{+}$, $^{4}He^{+}$ or $^{4}He^{++}$, which was impinged onto a water-cooled target. For the ^{7}Li(p,n)^{7}Be measurement, a beam of $^{1}H^{+}$ impinged on a thin LiF foil (natural abundance) mounted onto a thick tantalum backing. For the ^{13}C(α,n)^{16}O reaction, a beam of either $^{4}He^{+}$ or $^{4}He^{++}$ impinged on a 99% isotopically enriched ^{13}C foil also mounted on a thick tantalum backing. The outgoing neutrons for both reactions were measured at angles $\theta = 41.8°$ or 127.5° in the laboratory frame. The experimental set up at $\theta = 41.8°$ is shown in Fig. 5.20. An excellent understanding of the position of the detector is required, and the kinematic acceptance was taken into consideration in the uncertainty of this measurement.

Waveforms taken from the PEN scintillation detector were recorded using a CAEN V1725 250 MS/s, 14-bit waveform digitizer. The total pulse was integrated over 440 ns, with the short integral being 340 ns starting at an offset of 80 ns from the peak amplitude of the pulse.

The ^{7}Li(p,n)^{7}Be reaction was used to measure neutrons in the range of $0.8 < E_n < 1.9$ MeV and the ^{13}C(α,n)^{16}O reaction was used to measure neutrons in the range $2.5 < E_n < 7.1$ MeV. The energy deposited by an equivalent energy neutron was simulated using Geant4 for each measurement. As described in Section 5.4.2, the data were fit with a

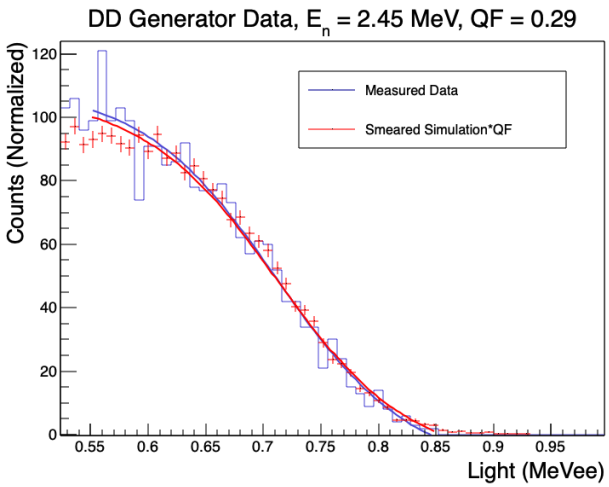


Figure 5.19: This is a plot of the data and simulations for the DD generator measurement. The simulation is fit to the same sigmoid function as the data.

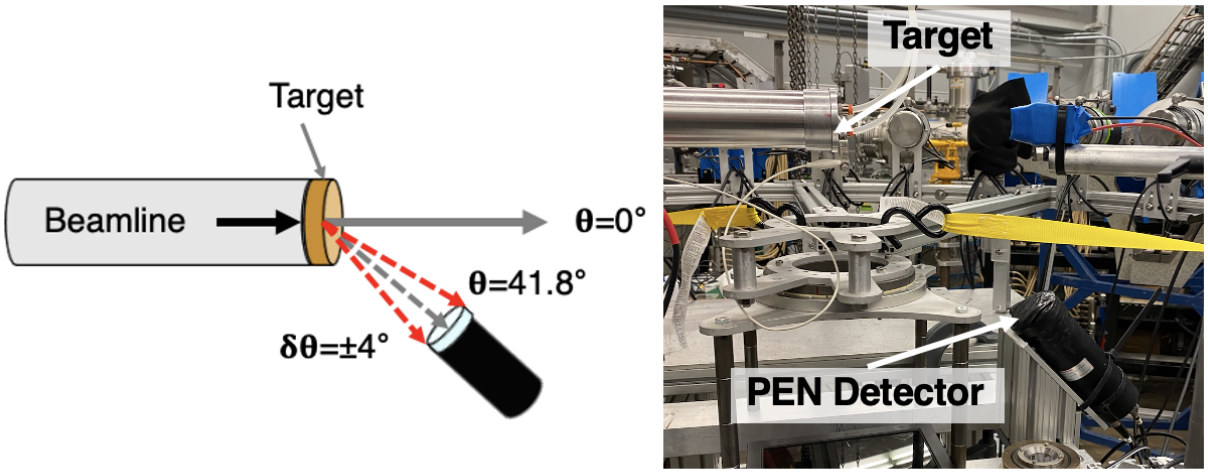


Figure 5.20: Experimental setup at University of Notre Dame Nuclear Science Laboratory with a diagram (left) and image (right). Detector placed 30 cm from target, at 41.8° from the beamline.

sigmoid function, with terms p_1 and p_2 being fixed, and the sigmoid function was fit to the smeared neutron simulation. In Fig. 5.21, the data from $E_n = 1.724$ MeV is plotted with the corresponding simulation and the PSD gates for the data are shown in Fig. 5.22. The PSD gates were determined by projecting a light bin onto the PSD axis and fitting a double Gaussian for each proton and electron recoil band. The PSD gates were then set to be 2σ from the mean of the Gaussian for each recoil band. The use of the PSD gates were vital in minimizing background events in the nuclear reaction measurements, as the gamma-ray background was often significant. An example is in the ^{13}C(α,n)^{16}O reaction, if the beam energy is $E_{C.M.} > 3.9$ MeV, then the second excited state of ^{16}O is populated, and will result in the emission of a 6 MeV gamma-ray. This high-energy gamma is one example of potential gamma-ray backgrounds that could affect measurements.

5.4.3 Error Analysis

The accuracy of the neutron energy determination for the fission chamber measurements was determined by measuring the spread of energies for a given energy slice. This was done by calculating the root mean squared of all the neutron energies of a certain slice. This is described in Eq. 5.13.

$$RMS = \sqrt{\frac{\sum_{i=1}^{n} (E_i - E_{Avg})^2}{n}} \tag{5.13}$$

The accuracy in the energy for the nuclear reaction measurements was partially determined by the kinematic acceptance of the detector geometry. It was also impacted by variations in the beamline energy impinging on the target, which was less than 40 keV between runs.

The error in the quenching factor values has been determined by variation seen in $\frac{\chi^2}{DOF} = \pm 2$, where χ^2 is found by fitting the sigmoid function to the neutron edge.

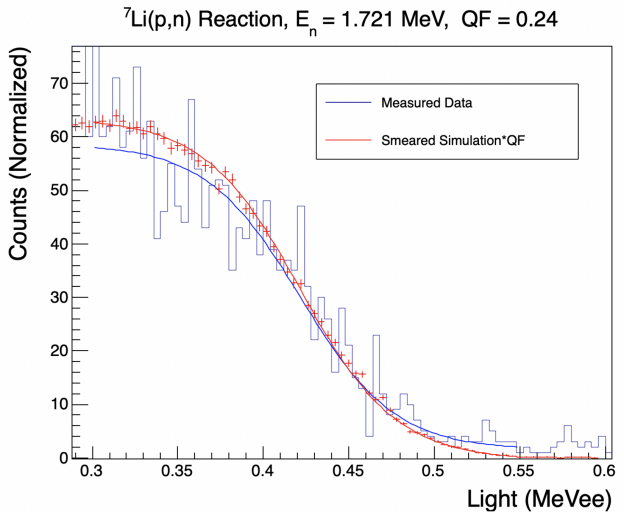


Figure 5.21: The data from $E_n = 1.724$ MeV is plotted with the smeared simulation. The data has excellent agreement with the simulation over the range where the sigmoid function is fit.

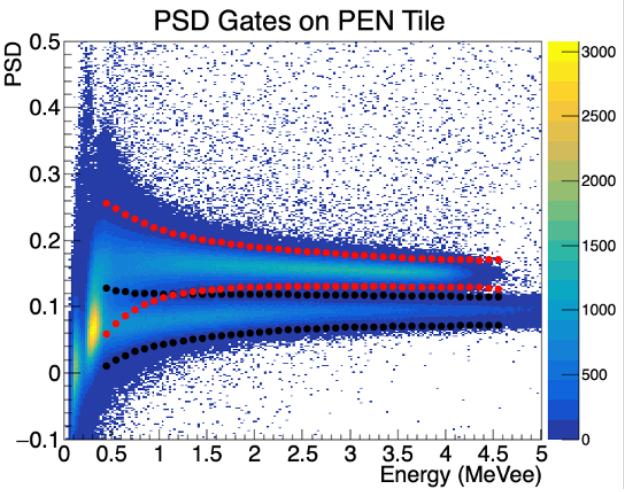


Figure 5.22: This plot shows the PSD gates for the PEN scintillation detector. Gates were used to distinguish neutron and gamma-ray events with an estimated probability.

5.4.4 Results of Light Response

The quenching factors are plotted for the three measurement methods in Fig. 5.23. It is seen that all three measurements have a good agreement with each other and follow a similar trend. At $E_n = 1.0$ MeV, PEN has a quenching factor $QF = 0.199 \pm 0.005$, where for example EJ-200 has a quenching factor of $QF = 0.156 \pm 0.003$ [103]. The reason for PEN's smaller quenching factor for neutrons, compared to EJ-200, is not clear but it does lend itself as a promising property for PEN as a self-vetoing material.

It is possible to analytically fit the Birk's law to quenching factor data using Eq. 5.5. By using numerical integration, it was possible to determine a best fit for the PEN light response and derive values for the scintillation efficiency, S and the Birk's factor, kB. ROOT Minuit fitting function determined the parameters which provided a minimum χ^2 and their respective error.

As shown in Fig. 5.24, the light response of PEN was fit with Birk's equation with a final fit of $kB = 0.12 \pm 0.01$ mm MeV^{-1} and $S = 1.31 \pm 0.09$ MeV$_{ee}$ MeV^{-1}. Again, kB describes the shape of the quenching factors for a given energy, the larger kB, the more the light response becomes non-linear with energy.

By defining the Birk's factor and scintillation efficiency, it is possible to define quenching factors for PEN at all energies. Using these parameters, the neutron spectral shape from the ^{13}C(α,n)^{16}O reaction where $E_n = 4.91$ MeV, was recreated. In Fig. 5.25, the simulated energy deposited by the neutrons (simulated in Geant4) are smeared and scaled given the light response of PEN. It is clear that over the whole spectrum, there is strong agreement and the method used in this analysis does well to recreate the measured spectrum.

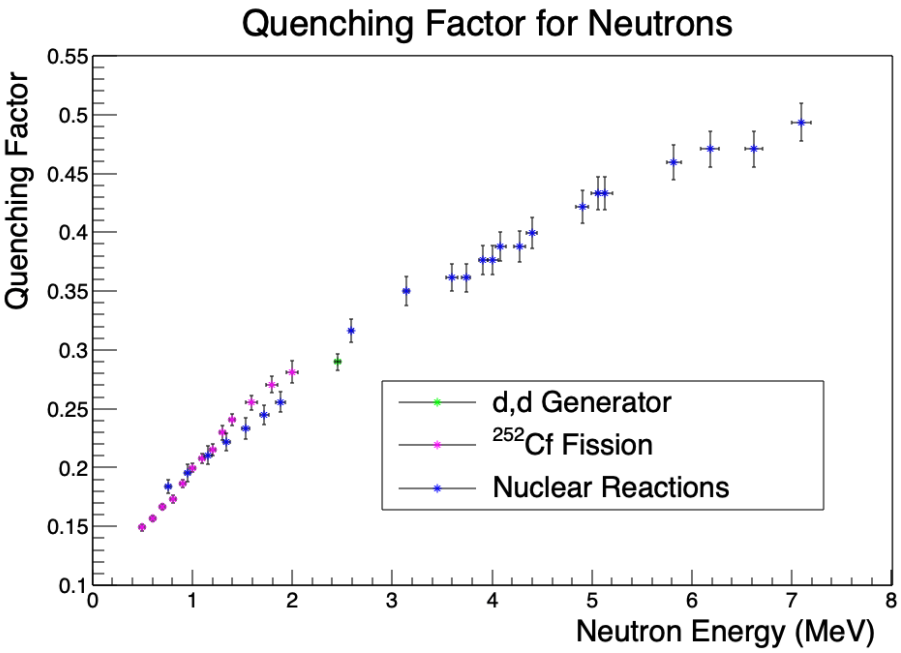


Figure 5.23: Quenching factors of all data show good agreement with each other.

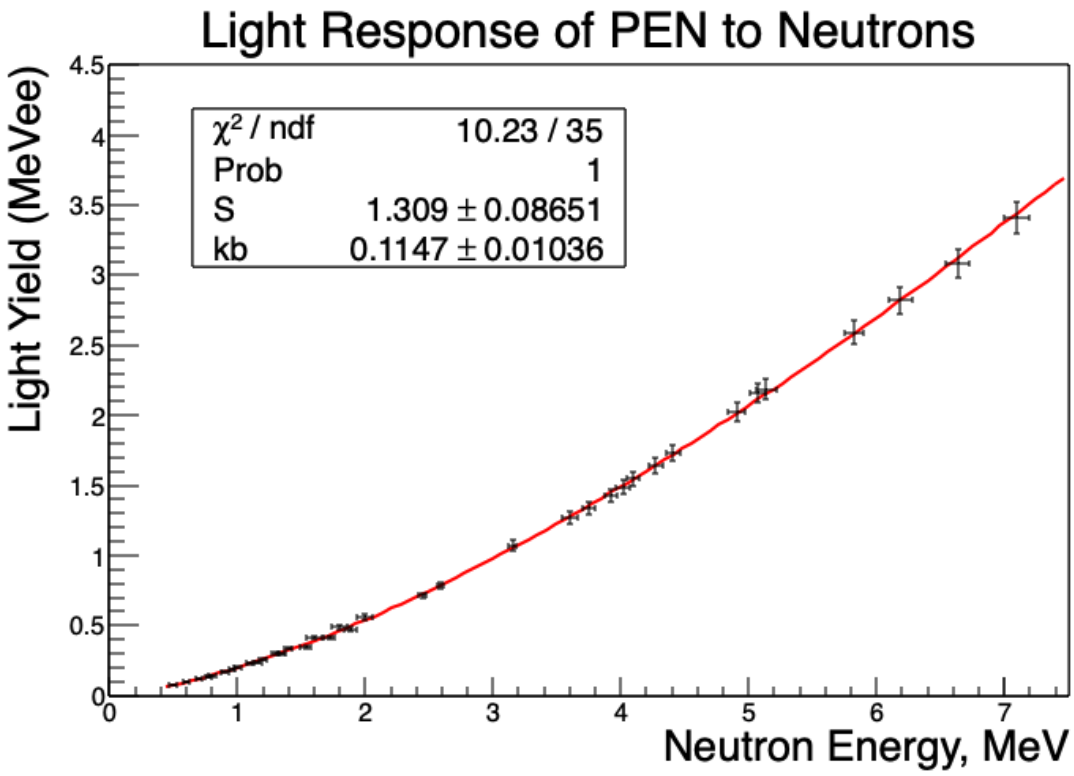


Figure 5.24: The light response of PEN fit with Birk's function, as described in Eq. 5.5.

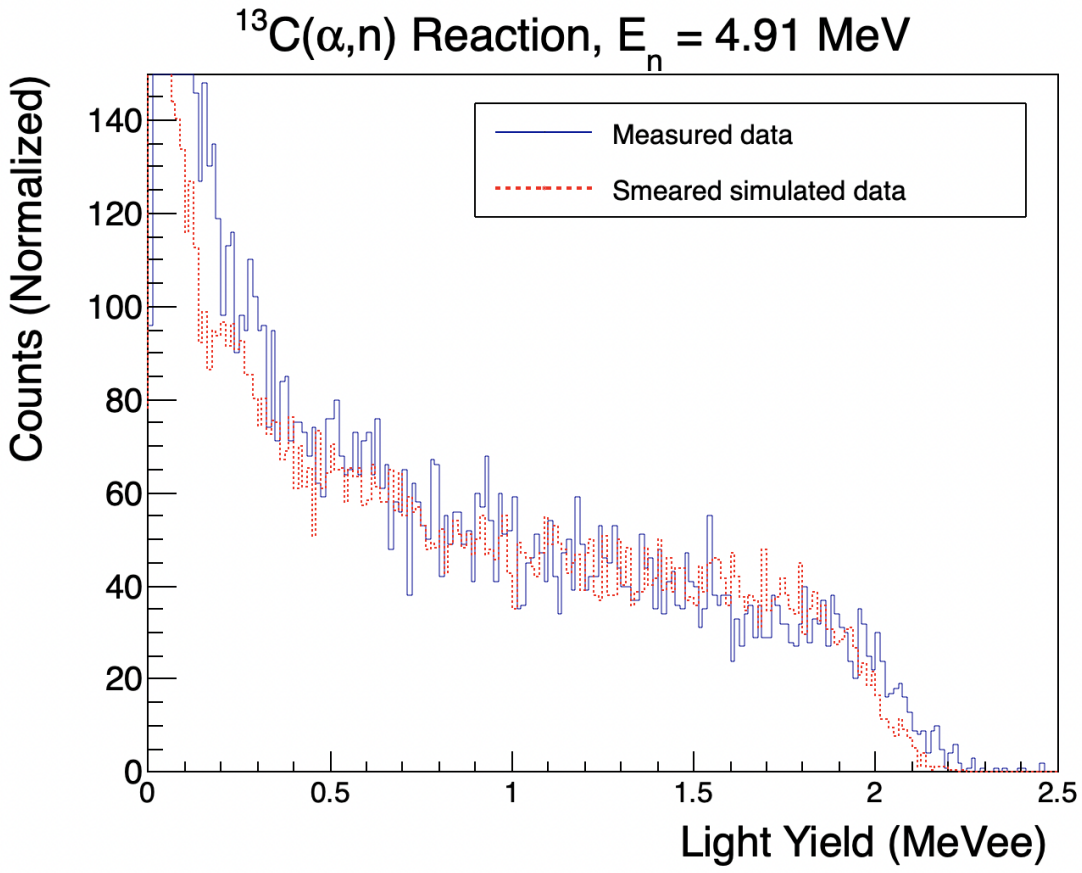


Figure 5.25: This figure shows data taken from neutrons generated in nuclear reactions, E_n = 4.906 MeV. The simulated energy deposited by neutrons at 4.906 MeV are smeared and scaled given the light response of PEN, recreating the measured data.

Chapter 6

PEN in the Post Gerda Test

The most direct method to test the PEN baseplate performance is to install it in a LEGEND geometry, and observe the performance of the component and the supported germanium detector. This testing is a necessity prior to committing to any component as the run time for LEGEND-200 and LEGEND-1000 are > 5 years. A test setup to quality access the baseplates should include a series of ^{76}Ge detectors with various shapes to reflect the LEGEND-200 geometry, use of improved electronics, and a well characterized infrastructure. The Post Gerda Test strives to meet these goals and provide an extensive test of the PEN baseplates and other components.

6.1 The Post Gerda Test (PGT)

After the Gerda experiment concluded its operations in 2020, and before installation of LEGEND-200 began, a short but necessary test was undertaken at LNGS, named the post Gerda test (PGT). This test included $\sim$ 40 kg of ^{76}Ge detectors, in the Gerda experiment geometry and light collection system(Chapter 3), but utilizing upgraded electronics and components for LEGEND-200.

One of the components upgraded in this geometry were the germanium crystals support baseplates. Originally in Gerda, the baseplates were constructed with silicon, an extremely

radio-pure material with very low levels of radioactivity. However these plates are expensive and passive, i.e. not scintillating, as well as opaque therefore not contributing to and potentially hindering the active veto system. One material that could be used as an active structural material is PEN, with a demonstrated low radioactivity (Section 4). In PGT, detectors were installed with either PEN baseplates or silicon baseplates. By installing these two in parallel, it was possible to have a direct comparison of the ^{76}Ge detector's performance with both materials and the first time it was possible to test long term mechanical performance of PEN in a cryogenic environment. The PGT was instrumental in determining the viability of using PEN baseplates for the LEGEND-200 experiment and provided feedback for LEGEND-1000 R&D.

6.1.1 Geometry of the PGT

The PGT had four strings with approximately four germanium detectors per string. The strings were mounted in a hexagonal geometry, with positions 1, 2 and 4, 5 having strings mounted and positions 3 and 6 being empty (Fig. 6.1 and 6.2). The string are identified as S1, S2, S3 and S4 and the detectors are identified as their position in the string, i.e. the first detector in the first string is S1.1. The germanium detector geometries installed included BeGes [104], ICPCs [105], PPCs [106] and coaxial detectors [107]. As mentioned previously, the same light collection system used in Gerda was used in the PGT. This includes a shroud of optical fibers, coated in TPB, optically connected to SiPMs to read out the light(Section 3.3.2). Over 600 hours of data was taken in this geometry to be analyzed and was used to define the stability of the PEN baseplates.

6.1.2 Preparation of PEN Plates for the PGT

I led the effort to produce PEN baseplates for the PGT. This included designing and preparing the machining jigs, developing a cleaning and handling procedure to minimize the introduction of radioimpurities, and personally assembled and deconstructed the jigs as well as packaged the PEN baseplates to be shipped to LNGS.

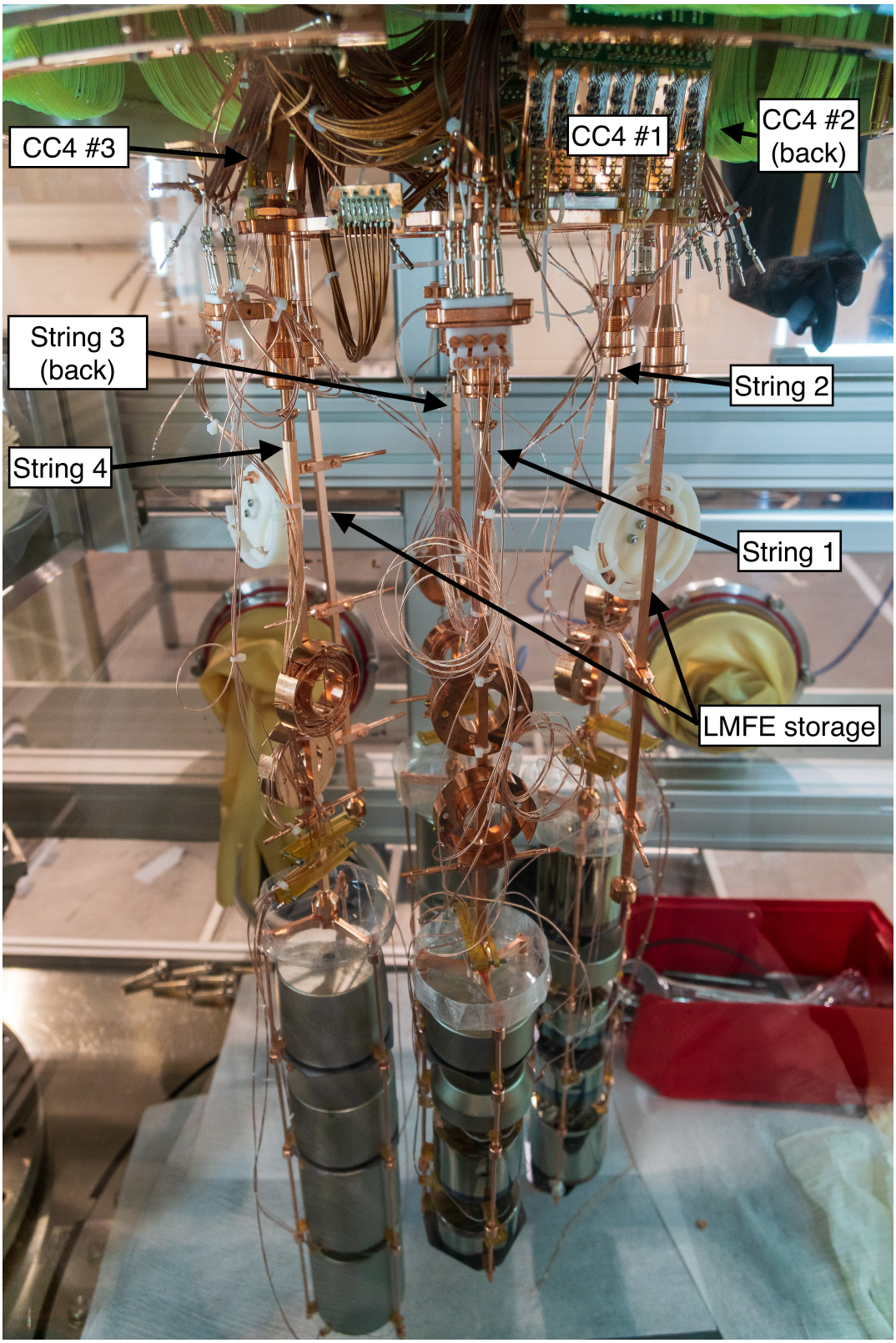


Figure 6.1: The Post Gerda Test geometry installed at LNGS in the Spring of 2020. This installation was originally for the Gerda Experiment.

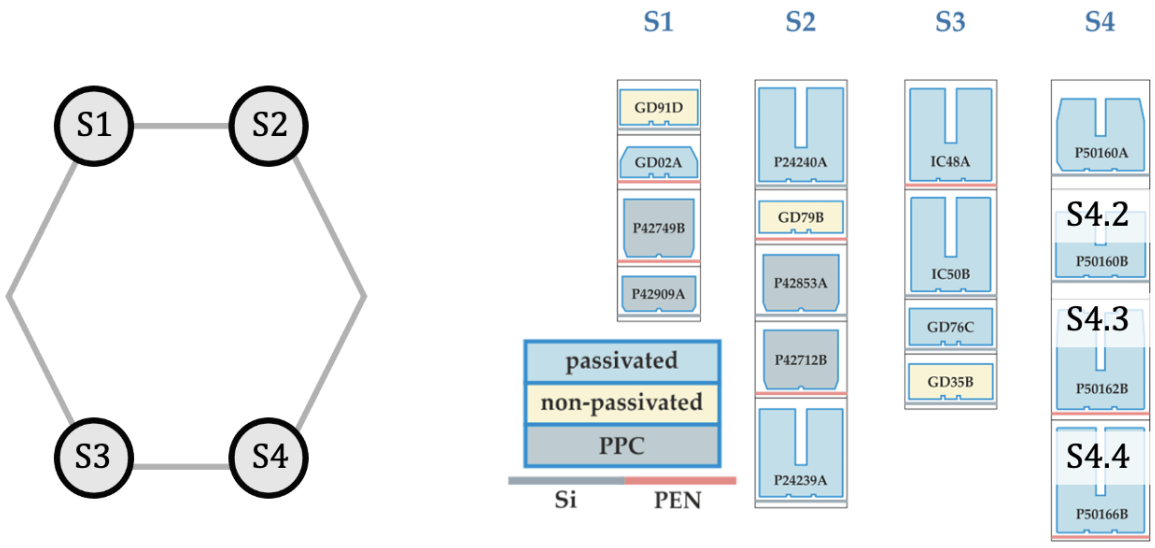


Figure 6.2: The orientation of the strings is shown on the left. On the right, a drawing of the geometry of the PGT test setup shows which detectors have PEN baseplates with an orange base. The string are identified as S1, S2, S3 and S4. The detectors are identified as their position in the string, i.e. the first detector in the first string is S1.1.

The timeline for obtaining components and completing installation for the PGT was aggressive so not interfere and delay needed upgrades for the LEGEND-200 experiment. For PEN to be installed and therefore considered for LEGEND-200, it was necessary to not delay and be in step with this timeline. To do this, the PEN tiles were machined at the University of Tennessee Machine shop. This is a well maintained machine shop with an expertise in machining and polishing scintillators [108], but is not designed to be an ultra clean environment. The method used to machine the PEN plates had to be adapted as the introduction of radioimpurities was very likely. A cleanroom was available at the University of Tennessee, with a laminar flow hood installed inside. The cleanroom was used as a buffer area for preparing the clean material, and the laminar flow hood was used as the clean environment for handling and packaging the PEN plates.

The plates have a complex geometry, with strict tolerances ($\sim$ 1 mm) to be installed in the detector strings. To ensure the tolerance was met, the plates were machined using a Computer Numerical Control machine, or a CNC machine. A CNC machine relies on the alignment of the system to ensure the positioning of machining is completed accurately. A jig was designed to allow for the CNC to be easily aligned and to minimize the likelihood of introducing radioimpurities (Fig. 6.3). The jig consisted of an upper and lower acrylic plate, to sandwich around the large PEN disk (Section 4) to be milled. The acrylic plates had stainless steel pins to align the PEN disk, and a center screw to maintain the structure for transportation. By sandwiching the PEN disk, and milling through the acrylic upper plate, the surface area of PEN that was exposed to the machine shop environment was minimized, and was only fully exposed when it was disassembled in the clean environment in the cleanroom.

After the upper and lower acrylic pieces for the jig were machined from new material, they were transferred to ORNL, with a series of stainless steel bolts, stainless steel calipers and stainless steel screw drivers. Once there, all components were washed with agitated 2% dilute Micro-90 for 24 hours, and rinsed with 18 MΩ water. The washing was completed in a laminar flow hood, to try and minimize the introduction of radioimpurities during washing. Images of the preparation are shown in Fig. 6.4. The conductivity of the rinse water of

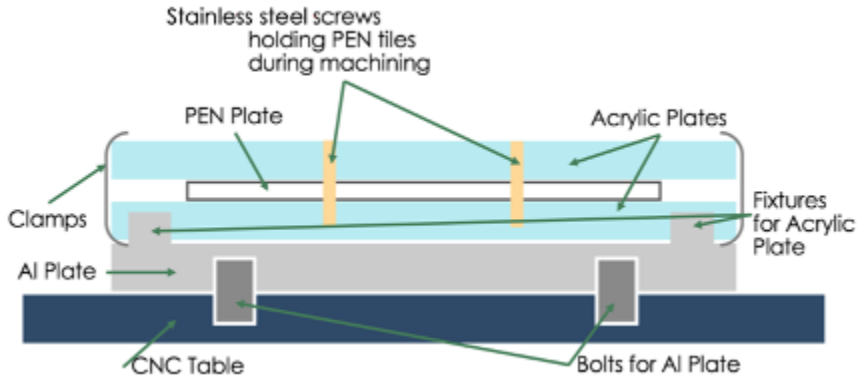


Figure 6.3: Diagram showing the jig for the machining of PEN plates for the Post Gerda Test.

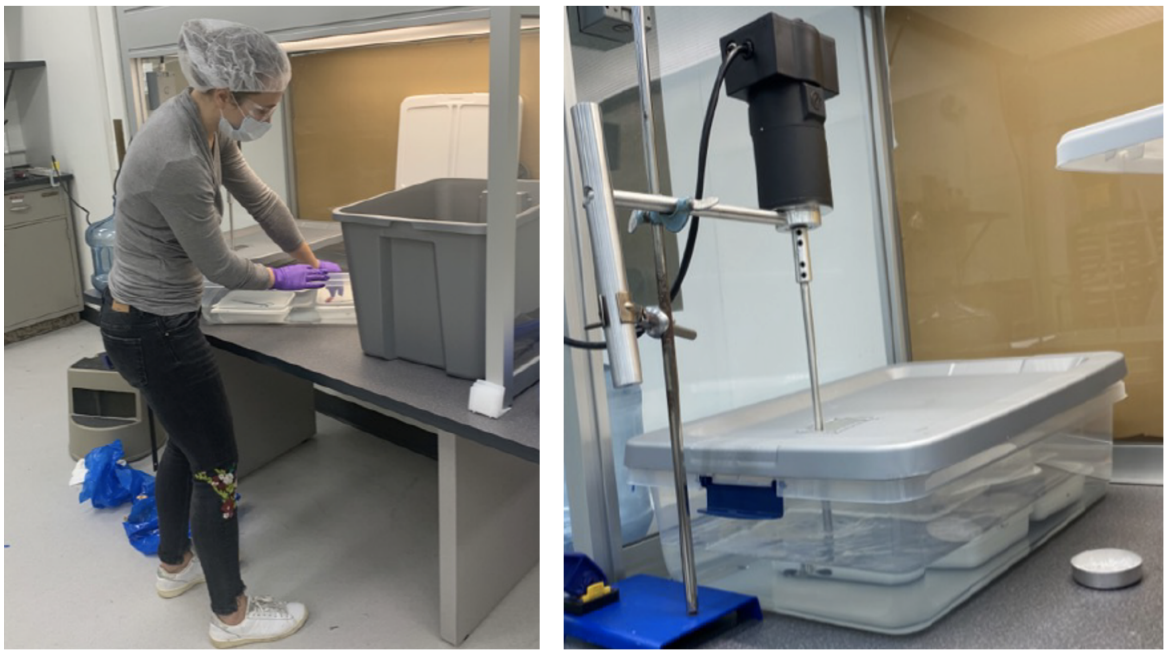


Figure 6.4: Left is an image of me preparing components to be washed in the laminar flow hood at ORNL. The image on the right is the dilute Micro-90 bath, washing components for PGT machining. Washing cycle took place over 24 hours to maximize cleaning.

each component was recorded and repeated until it reached the baseline conductivity. After rinsing, the components were stored in a clean, sealed container and transported back to the University of Tennessee's clean room, to be dried in the laminar flow hood.

The end mills and mill drills used for machining could not be washed with Micro-90 as there was the concern rust could form, so instead they were cleaned in an ultra sonic bath with hexane, acetone and then rinsed with 18 MΩ water.

Once all components were clean and dried, the jig was assembled in the laminar flow hood with a single PEN disk. After the jig was assembled, the whole setup was inserted in a large class-100 clean room bag and transported in a sealed container to the machine shop. Every effort was made to minimize the amount of time that the PEN material was exposed to an unclean environment, therefore a minimum amount of time was spent in the machine shop.

Each large disk produced $6-8$ PEN baseplates, and took approximately 6 hours to machine. The long machining time was due to a series of tool changes and installation of screws in the jig to maintain the upper acrylic plate coverage. Throughout the machining, careful notes were taken of potential exposures to contamination and which plates were affected. Throughout machining, boil-off N_2 gas was used as a coolant. Normally, compressed N_2 gas has insignificant levels of radon contamination, but by using boil off gas, the radon gas remains frozen in the bulk and only N_2 is released. An image of the CNC machine is shown in Fig. 6.5.

After the machining was complete, the jig was placed back in the clean bag and transferred back to the clean room. Once there, it was disassembled in the laminar flow hood and each PEN baseplate was packaged in class-100 clean room bags. The CNC machine at the UT machine shop was limited to what speed it could rotate at, and our cooling method was also limited. As a result, the edges of the PEN baseplates had significant burring, most of which could be easily removed, however with the concerns of contamination, were left to be removed later. An image of a finished PEN baseplate is shown in Fig. 6.6.

The baseplates were shipped to the Max Plank Institute in Munich to have the burring removed, and then brought to LNGS to be cleaned and acid etched. After cleaning, the



Figure 6.5: Image of the CNC used to machine the PEN baseplates. This image was taken after completing machining before disconnecting the jig from the CNC table.



Figure 6.6: PEN baseplates after machining. Significant burring can be seen along the edges, however the quality of the edge was maintained. The majority of burs were removed later using clean PEN tools.

baseplates were installed in the PGT, in the geometry shown in Fig. 6.1. More details of the machining and handling procedure are described in Appendix A.

6.2 Experimental and Simulated Data for the PGT

As previously mentioned, there were varied detector types in PGT as well as different detector baseplates. When referring back to Fig. 6.2, there are five ICPC detectors shown (U shaped detectors). In string S4, the second (S4.2), third (S4.3) and fourth (S4.4) detectors are mounted with either two silicon baseplates, one silicon and one PEN baseplate, or two PEN baseplates surrounding the detector. These three ICPC detectors provide an interesting opportunity to compare the contamination from the PEN baseplates, with these detectors having either zero, one or two PEN baseplates in close vicinity.

This section quantifies the rates of $E_\gamma = 2.614$ MeV from ^{208}Tl decay for a simulation and compare to data obtained during the PGT. In the simulation, contamination from ^{232}Th in the PEN baseplates was simulated. These rates in the simulation were used to understand the probability of the ^{76}Ge crystals measuring the $E_\gamma = 2.614$ MeV. The detection efficiencies were determined and compared for a series of data cuts: no cuts, AC cuts and PSD cuts. Then, using these efficiencies, a limit was set for the ^{232}Th contamination using the PGT data and the efficacy of these cuts were compared for each detector. Additionally there is a brief discussion on how using the active veto cut would improve the background rate at $Q_{\beta\beta}$ for the PGT setup.

6.2.1 Simulated Data of the PGT

The LEGEND collaboration has heavily invested in developing extensive Monte Carlo simulations to design the experiment's geometry and develop its background radiation model. This simulation framework, called MaGe [109], is based in Geant-4 and was developed jointly by the Gerda and Majorana collaborations. The MaGe framework contains geometric models for all objects in the LEGEND experiment, as well as all versions of the experiment itself,

including prototypes and tests stands. It has a large number of features including event generators, output formats and customization via the use of macros. By combining all of these tools into one framework, the aim was to reduce duplicate efforts and ease the comparison between simulated and experimental data.

To utilize a framework like MaGe, it is necessary to create a detector class for each version of the experimental geometry. When developing the PGT detector class, some unique aspects needed to be included as PGT included parts from Gerda, Majorana and the future LEGEND-200 experiment. The PEN baseplates have a detailed geometry, which could impact the light propagation and therefore veto efficiency of the baseplates. Therefore to ensure the simulation accurately reproduced PGT, a tessellated mesh was used to input the plate geometry, directly from a CAD drawing using a tool called CADMesh [110] (Fig.6.7). The geometry and placement of PGT was recreated in MaGe and rendered using FreeCAD (Fig. 6.8).

Optical Transport in MaGe

The first stage of generating a simulation using MaGe is to verify the geometry and the optical properties of the materials included (Section 5). Understanding how the veto efficiency changes with the use of the PEN baseplates predicts what can be expected in LEGEND-200. The optical properties measured in the previous chapters of this dissertation were included in the MaGe simulations.

An optical map is generated for the PGT geometry to describe the probability of light that is generated in a specific voxel being measured by the SiPMs. This includes the light reaching the wavelength shifting fibers, being wavelength shifted or transported through the TPB and finally travelling up the fibers to be read out by the SiPMs in the LAr veto system. This optical map takes wavelength shifting on PEN plates into consideration, as well as how the PEN wavelength shifted light will propagate in the LAr. The size of a voxel in these simulations are $5 \times 5 \times 1$ and $5 \times 5 \times 5$ mm for the PEN baseplate and the LAr simulations respectively. The optical map was generated for the volume around and inside the shroud of

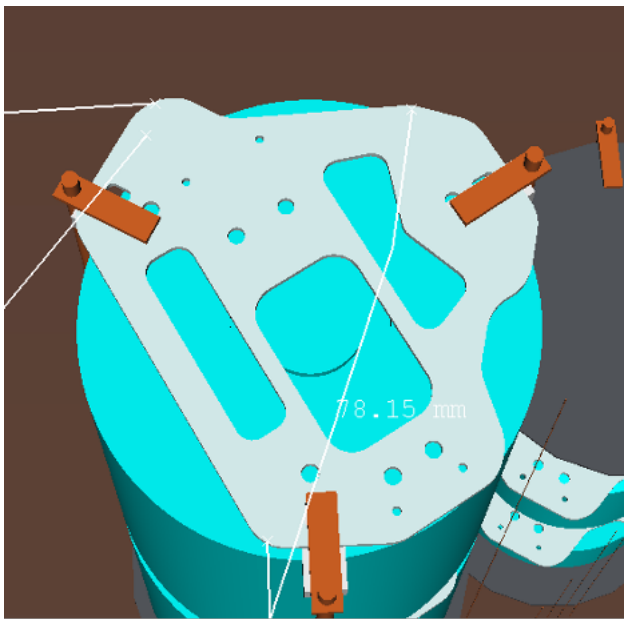


Figure 6.7: The geometry of the PEN base plate was recreated in MaGe using CADMesh, shown here in this rendering of PGT.

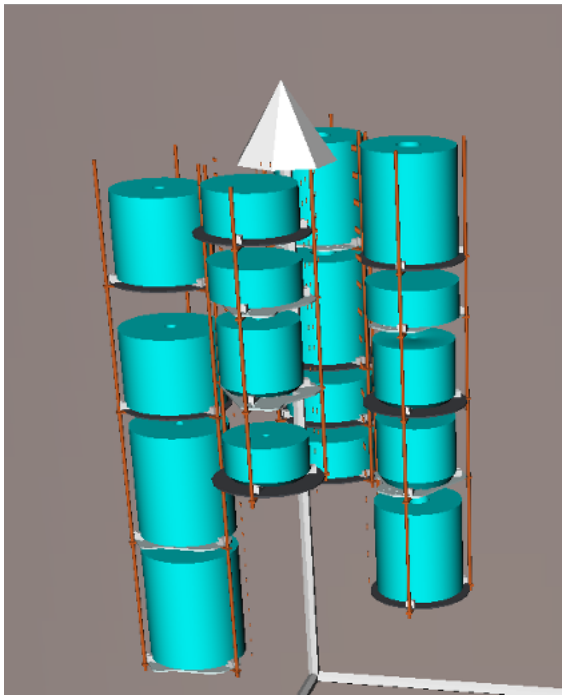


Figure 6.8: Rendering of the PGT geometry using MaGe.

wavelength shifting fibers. There are two generators, a LAr generator and a PEN generator. Each generator only produces photons when the location in the voxel matches the material. If the material matches the generator, it produces a photon corresponding to the spectrum for the generator (e.g. $\sim$ 128 nm or $\sim$ 450nm for LAr and PEN). Assuming the material matches, 500 photons are produced and tracked through the geometry of the PGT and the simulation records if the photon reaches the SiPM detectors. The optical map for the LAr light propagation and the PEN baseplate light propagation can be seen in Fig 6.9 and Fig. 6.10.

Across the surface of the PEN baseplate, the average probability that a photon will reach the SiPMs and be read out is $P \sim 0.002$. Decreased probability can be seen surrounding areas in the middle of the baseplate, which is as expected as PEN's attenuation is significant at its peak emission ($\lambda \sim 6$ cm at 450 nm). Combining this detection probability with the known light yield of PEN ($LY_{PEN} \sim 5000$ photons per MeVee [67]), the sensitivity of PEN baseplates, $E_{Deposited}$, in the PGT can be approximated.

$$E_{Deposited} = \frac{\text{Photons Detected}}{LY_{PEN} \times P} \tag{6.1}$$

For a three photon sensitivity, the minimum energy E_{min} is defined as:

$$E_{min} \geq 0.3 \text{ MeV}. \tag{6.2}$$

There is another problem to consider; the limited amount of energy a recoiling electron (from an interacting gamma-ray or beta particle) can deposit before it leaves the surface of the PEN baseplate. As the PEN baseplate is only 1.5 mm thick, the maximum energy an electron can deposit is $E_{max} = 0.5$ MeV. For the PEN baseplates to have any significant ability to veto radiation from beta particles or gamma-rays the detection threshold, E_{min}, must be less or equal to the maximum energy that can be deposited through the PEN baseplate, $E_{max} = 0.5$ MeV. Otherwise, it becomes increasingly unlikely that the electron will travel a long enough distance in the tile, and produce enough scintillation light that

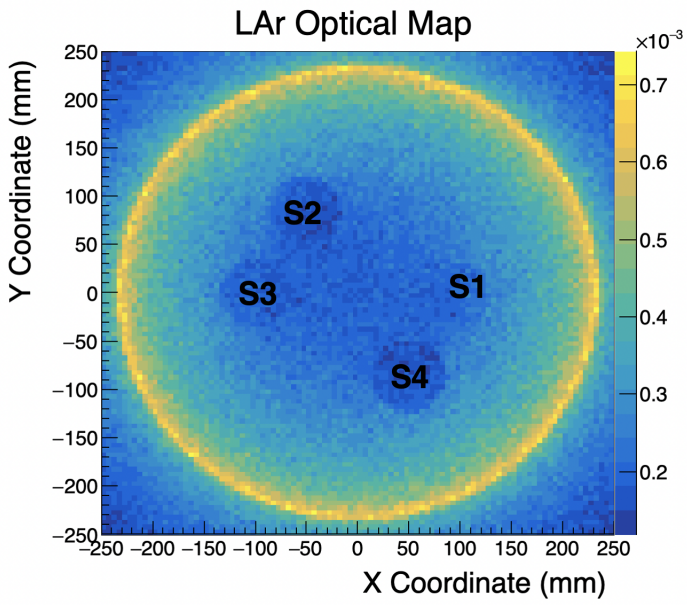


Figure 6.9: Probability mapping of light produced in a $5 \times 5 \times 5$ mm voxel in LAr to reach the light readout system and be detected by the SiPMs. This map was generated by MaGe in the PGT configuration. The faint outline of circles is the decreased probability from the silicon baseplates, and gives perspective to where the strings are located.

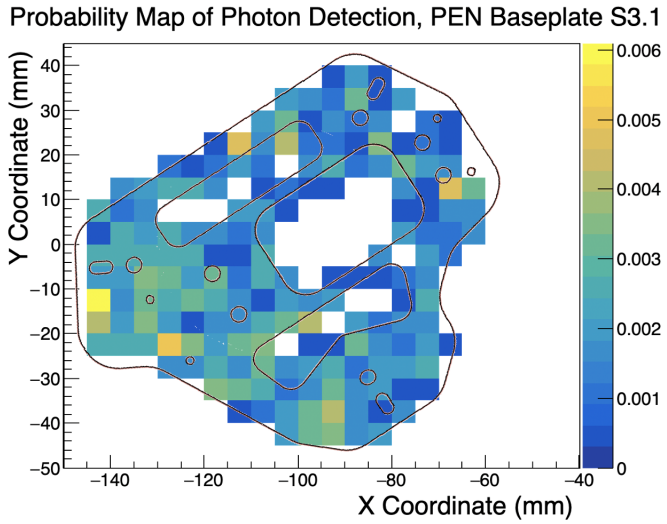


Figure 6.10: Probability mapping of light produced in a $5 \times 5 \times 1$ mm voxel in PEN to reach the light readout system and be detected by the SiPMS. This map was generated by MaGe in the PGT configuration. An outline of the PEN baseplate can be seen overlaid on the probability map.

the event can be detected. By rearranging Eq. 6.1, it is possible to define the minimum probability P_{min}, setting $E_{max} = 0.5$ MeV and the Photons Detected = 3.

$$P_{min} \geq \frac{\text{Photons Detected}}{LY_{PEN} \times E_{max}} = 0.0012 \tag{6.3}$$

The PEN baseplate has a probability $P_{min} \geq 0.0012$ across most of the volume, supporting the idea that it will be able to partially veto events from passing gamma-rays and beta particles.

Rates from Simulation Analysis

As previously described, MaGe is used to understand the energy deposition and the light collection across the geometry of the LEGEND experimental setup. With these two maps (energy deposition and light detection probability), it is possible to use GAT (Germanium Analysis Toolkit) to generate spectra from each crystal, and apply cuts that are equivalent to the cuts applied to data. The experimental data that this dissertation will compare to is no cuts, an anti-coincidence (AC) cut and a pulse shape discrimination cut. An AC cut essentially removes any events where another ^{76}Ge crystal is also triggered. This cut is useful for high energy gamma-ray events that scatter from one crystal to another or for muon events (Section 3.3.2). A pulse shape discrimination (PSD) cut uses the shape of the pulse to define whether the event was a single site or a multi-site. If the event is multi-site, there will be two sequential pulses stacked, where a single site event will be a continuous shape (Section 3.3.2). GAT does not directly generate pulses to be analyzed, but uses drift maps - how fast charge drifts in different voxels in the crystal - to assign a parameter called the heuristic value. It is expected that the heuristic value used for cuts will be different for each crystal but can be informed by understanding the cuts used in the experimental data analysis. The value used for the heuristic cut is defined where approximately 40% of the Compton scattered events from the gamma at $E_\gamma = 2.614$ MeV should be retained. This is considered equivalent to the experimental data cut using PSD.

The fictional radiation simulated in MaGe was ^{232}Th contamination in the PEN baseplate volumes. This would include the decay daughters like ^{208}Tl, which produces a characteristic

peak at $E_\gamma = 2.614$ MeV. In these simulations, 1×10^6 decays were simulated to occur somewhere in the PEN baseplates. It will be possible to see how the rate of detection (for $E_\gamma = 2.614$ MeV) changes as cuts are applied to the data. The three crystals that are being considered are S4.2, S4.3 and S4.4, with the respective simulated data shown in Fig. 6.11, Fig. 6.12 and Fig. 6.13. The detection efficiencies for measuring $E_\gamma = 2.614$ MeV are shown in Table 6.1.

6.2.2 Experimental Data for the PGT

Around 40% of the ^{76}Ge detectors installed in the PGT were mounted with PEN baseplates. Of these, studies were conducted to check the stability of the detectors with PEN plates and compare them to the detectors with silicon base plates. A major concern for detectors with PEN plates is charge collection across the plate that could cause shorting to occur across the electronics mounted to the baseplate. A minimum requirement for PEN to be considered as a material for the baseplate is that there was no substantial loss of performance of the ^{76}Ge detectors. A baseline study was therefore conducted to understand the stability and performance using two ICPC detectors, each with either a PEN or a silicon baseplate [111]. The baseline for this study was determined using the first 1000 samples of the waveforms from the ICPC detectors and averaged. There was no significant difference seen between these two detectors over this time period (Fig 6.14). The energy resolution between these two detectors was also compared using a ^{208}Tl source, $E_\gamma = 2.614$ MeV. The FWHM for these two detectors was found to be 2.43 keV and 2.61 keV for the silicon and PEN mounted detectors respectively, within uncertainty of each other [111].

Rates from Experimental Data Analysis

The data that is being presented in this dissertation was analyzed by Frank Edzards as part of his PhD dissertation [111]. Data run Run0030 was taken over 27 days and was also used for the baseline study (Fig. 6.14). As mentioned previously, the three detectors being used for this study are S4.2, S4.3 and S4.4 which correspond to ADC Channels 38, 39 and 40.

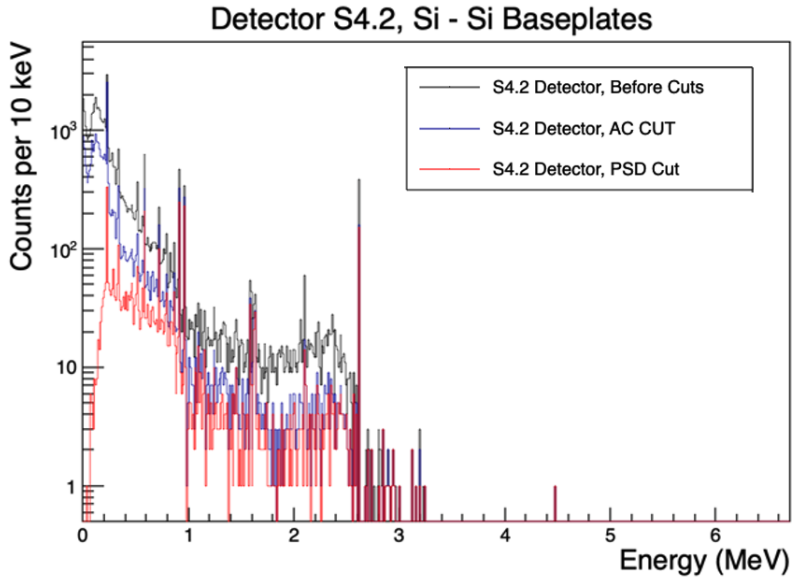


Figure 6.11: Simulated data from detector S4.2 with 1×10^6 events of ^{232}Th decays in all PEN baseplates. This detector had a silicon baseplate above and below it.

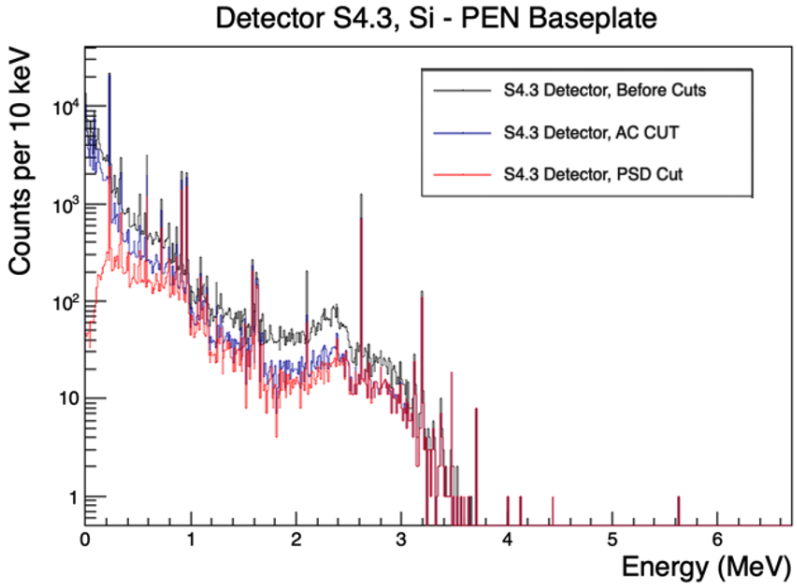


Figure 6.12: Simulated data from detector S4.3 with 1×10^6 events of ^{232}Th decays in all PEN baseplates. This detector had a silicon baseplate aboive it and a PEN baseplate below it.

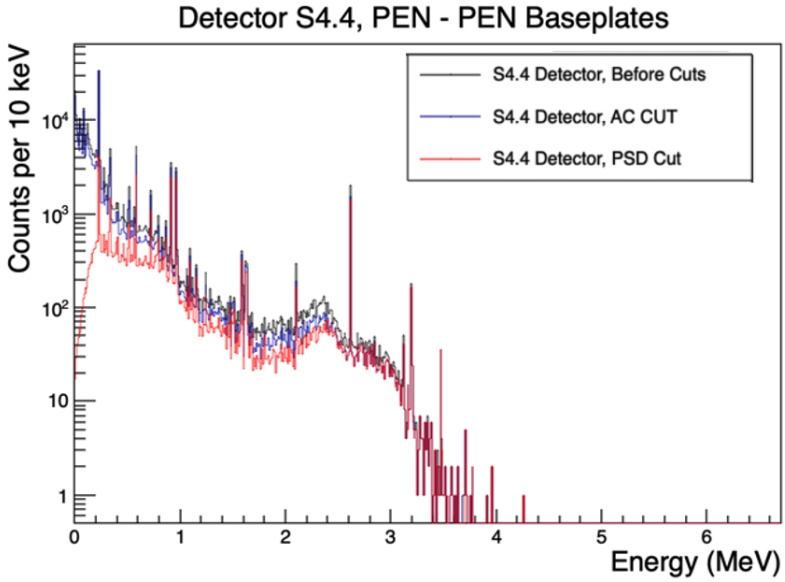


Figure 6.13: Simulated data from detector S4.4 with 1×10^6 events of ^{232}Th decays in all PEN baseplates. This detector had a PEN baseplate above and below it.

Table 6.1: Simulated detector efficiencies for $E_\gamma = 2.614$ MeV simulated using the MaGe and GAT software packages.

Cuts	Detection Efficiency for $E_\gamma = 2.614$ MeV		
	S4.2	S4.3	S4.4
Before Cuts	0.000386	0.001254	0.00202
AC Cuts	0.00159	0.000725	0.0015
PSD Cuts	0.00015	0.000684	0.001404

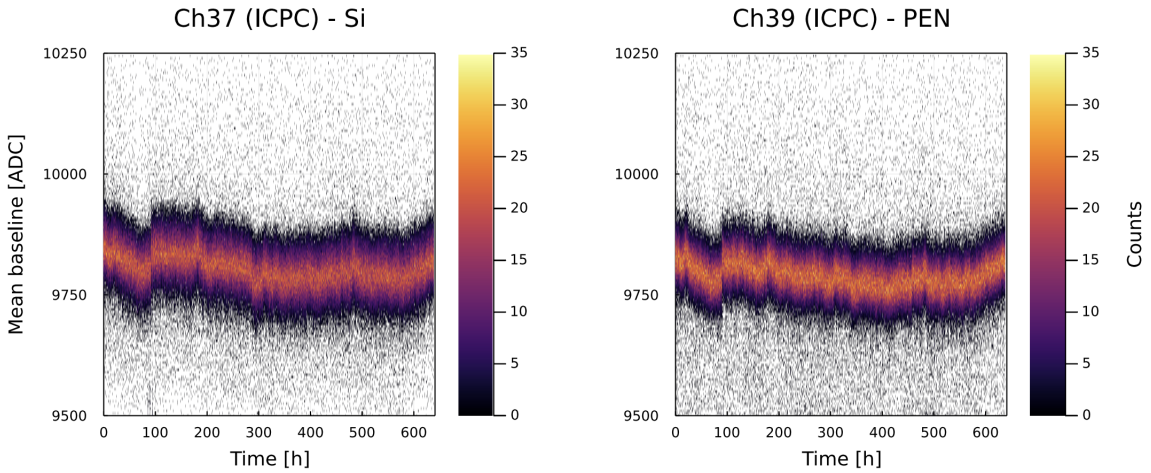


Figure 6.14: Baseline studies for the PGT taken over 27 days to test the stability of detectors with PEN baseplates [111]. The mean baseline is shown for the detectors mounted with silicon (left) and PEN (right).

Like the simulation data, a series of cuts were applied to the data to see how the background was affected. The first cut was an anti-coincidence (AC) cut, which removes any events where more than one ^{76}Ge crystal was triggered. Similar to the multiplicity cut, this is to remove any events that would scatter from one crystal to another. The AC cut also includes a general data cleaning, where pile-up and other poor quality pulses are removed. The second cut was the pulse shape discrimination (PSD) cut. This cut looks at the A/E ratio, or the ratio of the maximum amplitude for the pulse (A) and the total energy (E) for the pulse. The PSD cut used in this data places a cut on both low and high A/E ratios. A low A/E cut removes multi-site events - or events where there were multiple locations where energy was deposited. This is an important tool, as $0\nu\beta\beta$ decay will have a single site energy deposition. A high A/E cut is used to remove events surrounding the p+ contact of the ^{76}Ge crystal. The spectra from detectors S4.2, S4.3 and S4.4 with each series of cuts are shown in Fig 6.15, 6.16 and 6.17 respectively.

There are a number of features to note in Fig. 6.15, 6.16 and 6.17. First, the strong peak seen at E 3750 keV is from an external pulser, used for testing and non-linearity investigations of the setup. Second, the peak seen at $E = 1524$ keV is from ^{42}Ar contamination. These increased levels were expected as the PGT did not use any sort of shroud or passive shielding to mitigate the drift of charged ions reaching the detectors. Finally, there is possibly a peak forming in Fig. 6.17 at $E = 2614$ keV from ^{208}Tl decay from ^{232}Th contamination.

6.2.3 Placing ^{232}Th Limits in PEN Baseplates

The MaGe simulation package was used to understand how energy is deposited in the PGT geometry if the PEN baseplates contained ^{232}Th contamination. With these simulations, it was possible to use GAT and produce spectra with a series of cuts. After the cuts were applied, the efficiency, ϵ, was defined for each ^{76}Ge crystal for detecting the $E_\gamma = 2.614$ MeV from ^{208}Tl decay (Table 6.1).

PGT experimental data were used to set limits on the activity of $E_\gamma = 2.614$ MeV from ^{208}Tl decay. This was done by fitting the experimental data with a second order polynomial

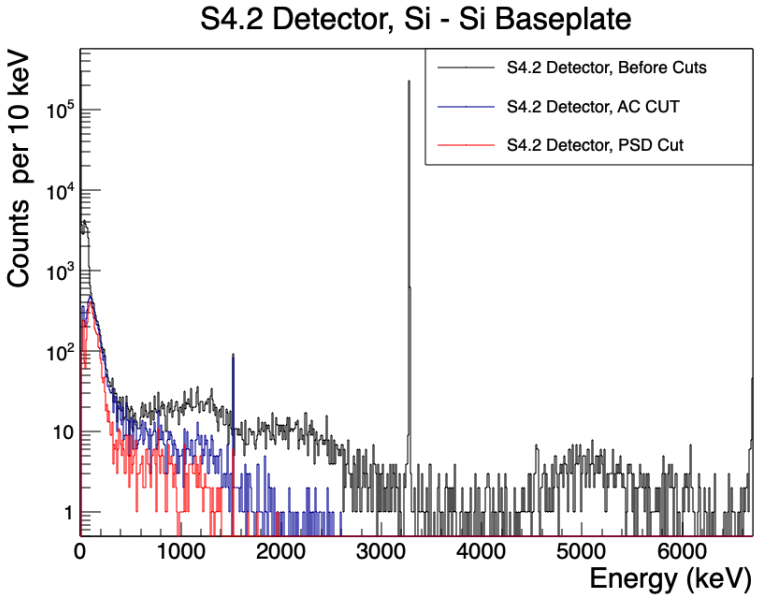


Figure 6.15: Spectrum from detector S4.2 after taking data for 27 days in the PGT setup. This detector had a silicon baseplate above and below the detector. Data has been reformatted from F. Edzard's dissertation [111].

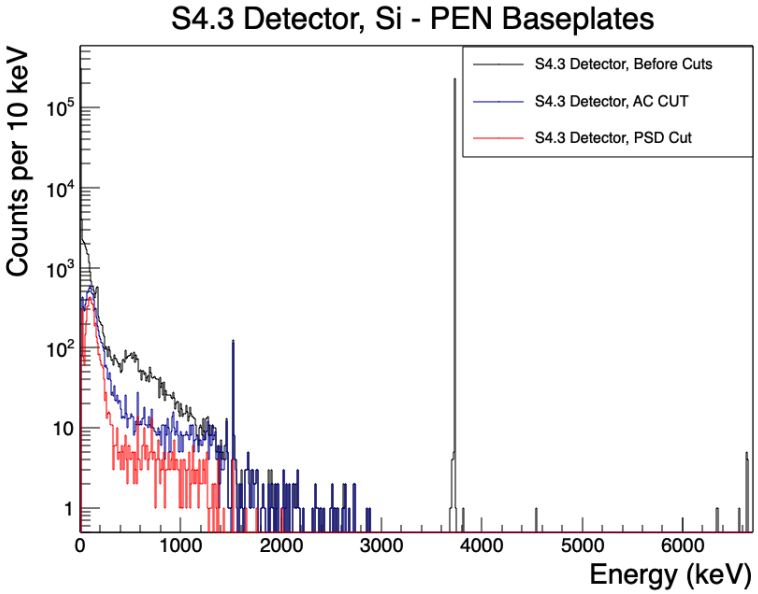


Figure 6.16: Spectrum from detector S4.3 after taking data for 27 days in the PGT setup. This detector had a silicon baseplate above the detector and a PEN baseplate below it. Data has been reformatted from F. Edzard's dissertation [111].

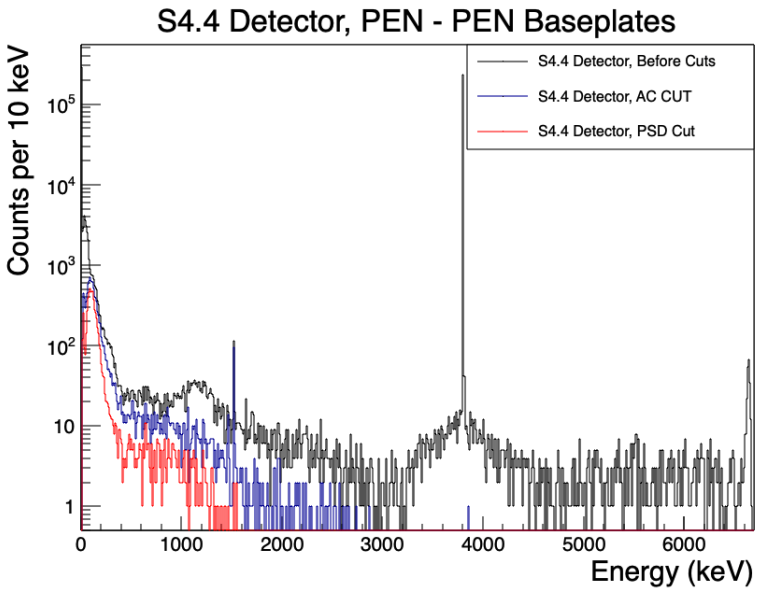


Figure 6.17: Spectrum from detector S4.4 after taking data for 27 days in the PGT setup. This detector had a PEN baseplate above and below the detector. Data has been reformatted from F. Edzard's dissertation [111].

in the energy range $2.50 < E_\gamma < 2.70$ MeV:

$$F = a \times x^2 + b \times x + c \tag{6.4}$$

then adding counts at $E_\gamma = 2.614$ MeV until $\Delta\chi^2 \geq 4$:

$$\Delta\chi^2 = \chi^2_F - \chi^2_{F'}. \tag{6.5}$$

For simplicity, it is assumed that the ^{232}Th content in the PEN baseplates is in secular equilibrium. Secular equilibrium is defined as when all of the decay products in a decay chain have the same half life as the progenitor of the decay chain, so in this case the same half life as ^{232}Th. This occurs when the progenitor has a long half life, resulting in the production rate of the decay daughter being equal to its own decay rate. This is not always the case, secular equilibrium is sometimes broken by chemical processes that result in the accumulation or depletion of some isotopes [112]. However for the scope of this dissertation, it is assumed that ^{208}Tl is in secular equilibrium with ^{232}Th, so for a single decay of ^{232}Th, there will be a single decay of ^{208}Tl.

Each of the PEN baseplates has a mass of 5.72 g, therefore the total PEN mass in the PGT was 40.07 g. Considering the branching ratio of $E_\gamma = 2.614$ MeV in ^{208}Tl decay (99.75%), the efficiency of each detector measuring the $E_\gamma = 2.614$ MeV, the specific activity for ^{232}Th and the total time that the data was collected ($\sim 2.31 \times 10^6$ s), it was possible to set limits on the ^{232}Th content in the PEN baseplates (Table 6.2).

These limits in Table 6.2 are at the level of parts per billion (ppb) or 10^{-9} g/g. For LEGEND-200, it is expected that the sensitivity will change significantly. The mass of PEN in LEGEND-200 will increase from $\sim$ 40 g to $\sim$ 1140 g. This is approximately 29 times the amount of mass, so the limits would go from $\sim 10 \times 10^{-9}$ g/g to $\sim 3.5 \times 10^{-10}$ g/g. As well, the run time for LEGEND-200 will be significantly longer than the PGT. The run time for LEGEND-200 is 5 years, so compared to the run time of PGT at 27 days, there is an

Table 6.2: Background measurements conducted at the PGT were used to place limits on the content of the ^{232}Th levels inside the PEN baseplates.

Cuts	S4.2, Si - Si Baseplate		
	Counts	Specific Activity (Bq/g)	^{232}Th Content (ppb)
Before Cuts	<5	$<1.41\times10^{-4}$	< 34.8
AC Cuts	<6	$<4.09\times10^{-4}$	< 101.3
PSD Cuts	<4	$<2.89\times10^{-4}$	< 71.6

Cuts	S4.3, Si - PEN Baseplate		
	Counts	Specific Activity (Bq/g)	^{232}Th Content (ppb)
Before Cuts	<6	$<5.19\times10^{-5}$	< 12.9
AC Cuts	<5	$<7.48\times10^{-5}$	< 18.5
PSD Cuts	<4	$<6.34\times10^{-5}$	< 15.7

Cuts	S4.4, PEN - PEN Baseplate		
	Counts	Specific Activity (Bq/g)	^{232}Th Content (ppb)
Before Cuts	<8	$<4.30\times10^{-5}$	< 10.6
AC Cuts	<6	$<4.34\times10^{-5}$	< 10.7
PSD Cuts	<4	$<3.09\times10^{-5}$	< 7.7

increase of approximately 67 times the amount of run time. This increase in run time would further reduce the limit from $\sim 3.5 \times 10^{-10}$ g/g to $\sim 5.1 \times 10^{-12}$ g/g or 5 ppt.

6.2.4 Predicted Veto Efficiency with PEN Baseplates

Unfortunately, the active veto system was not online during the PGT therefore there was no scintillation data from the PGT. Though this does prevent the verification of the optical simulations, it does allow for a prediction of how the veto efficiency will change with the use of PEN. It is possible to apply a third cut to the data on how many photo-electrons or PEs were detected for a certain event. The impact of using an active veto baseplate was investigated by simulating ^{232}Th contamination in all baseplates in string 4, S4. For example, detector S4.2 would have contaminated, passive baseplates above and below the detector, where detector S4.4 would have contaminated, active baseplates above and below the detector. The simulation was run for 1×10^6 events, randomly distributed in the two silicon and two PEN baseplates, using the MaGe software package and analyzed using the GAT processing code.

To understand the impact of the light cut on the background in the region surrounding $Q_{\beta\beta} = 2.039$ MeV, a zeroth order polynomial was fit in the region fit of $2.00 - 2.08$ MeV. The results of these fits in the three different detectors are shown in Table 6.3. The third cut requires that there are three photo electrons detected by the light readout system for the event to be vetoed.

The final line of the table, Light Cut Efficiency, describes what fraction of the background was removed using the Light Cut of PE$<$ 3. The reduction of background is significantly improved from S4.2, surrounded by passive material, to S4.4, surrounded with active material. This does not consider the increased veto efficiency for events that occur in the volume in between the crystals. In these volumes, the PEN material could either produce scintillation light for radiation passing through it, or wavelength shift the ambient LAr light that hits the PEN baseplate, improving the likelihood of the light being read out by the active veto system.

Table 6.3: Simulation of artificially contaminated baseplates in string 4, S4, to predict the veto efficiency of PEN baseplates in a PGT geometry.

Cuts	Background Level		
	S4.2, Si - Si	S4.3, Si - PEN	S4.4 PEN - PEN
Before Cuts	126 ± 4	98 ± 4	57 ± 3
AC Cuts	53 ± 3	39 ± 2	41 ± 2
PSD Cuts	36 ± 2	28 ± 2	30 ± 2
Light Cuts (PE<3)	5.7 ± .8	4.3 ± 0.7	3.3 ± 0.7
Remaining Background Fraction	0.156	0.155	0.111

Chapter 7

Conclusion

The elusive neutrino has provided an expansive landscape to probe and understand the physical universe. Its passive behaviour to the world around us has left us with a series of basic questions about its behavior. One very important question is the nature of the neutrino, whether it be Majorana (its own antiparticle) or Dirac (distinctly different from its antiparticle). The discovery of $0\nu\beta\beta$ decay would definitively fix the neutrino as Majorana, provide insight into how our universe was formed, and potentially determine the mass of neutrino (Section 2).

There are a number of competing technologies to measure $0\nu\beta\beta$ but one with particular promise is the measurement of ^{76}Ge decay in the LEGEND experiment. With outstanding energy resolution and extensive background reduction techniques, this experiment aims to be sensitive to a half life $T_{1/2}^{0\nu\beta\beta} > 10^{28}$ yrs. To reach this sensitivity, it is vital to be able to identify background radiation events inside and around the ^{76}Ge detectors. This is partially done by using pulse analysis in the germanium detectors, including pulse shape discrimination and particle position reconstruction. Another way to mitigate radiation is to use active materials, such as scintillators, to provide a signal when external radiation is detected, called active veto systems (Section 3).

The active veto system in the LEGEND experiment is a LAr cryostat surrounding the ^{76}Ge detectors, which acts both as a cryogen and an active material producing scintillation

light. There is an optical fiber system, attached to SiPM (silicon photo-multipliers) detectors submerged in the LAr, to wavelength shift and read out the scintillation light. This method of background identification and reduction was successfully applied by the Gerda collaboration and extended for the LEGEND-200 and LEGEND-1000 experiments.

This dissertation extends the efficiency of the active veto system in LEGEND by replacing inactive, structural components with an active material. The material selected was poly(ethylene 2,6-naphthalate) or PEN. PEN has a sustained interest as both a self veto material, and a stable component for wavelength shifting LAr light. The commercially sourced PEN was extensively characterized, as outlined in this dissertation (Section 4 and 5). These studies allowed for the understanding of whether the PEN baseplates were suitable for LEGEND-200 and beyond.

The radioactivity of the PEN material was measured using multiple methods. This included ICP-MS, HPGe counting and radon emanation measurements. Throughout these measurements, the material met or surpassed the requirement of $<\mu$Bq per part for a component to be installed in LEGEND-200 (Section 4.3).

Not only was the radiopurity of the material considered, but also its optical properties. The surface reflectivity was determined by considering the dispersion of light reflecting off of the PEN baseplate surface (Section 5.2.1). The reflectivity was measured directly using a custom made reflectivity tool and looking at the light fluctuation reflected off of the tile surface. This dispersion was determined using parameter σ_α, and a mirror was used to determine the minimum sensitivity of the instrument. PEN was found to be a specular reflector with $\sigma_\alpha = 0.46 \pm 0.07°$. The attenuation length of the PEN baseplates was also measured directly by machining small tiles out of the material produced (Section 5.2.2). Using a dual beam spectrophotometer, the light absorbance was measured through the tile and the attenuation length at the peak scintillation wavelength for PEN was determined to be $L_{\lambda=425\ nm} \sim 6$ cm, which is significantly smaller than the thickness of the tile but on the order of the tile width.

PEN must act as a self-vetoing material for low background experiments, therefore the light response of PEN is a necessary detail to understand the veto efficiency of a PEN

component. The use of multiple neutron sources allows for the measurement of the light response of PEN over a large neutron energy range, with each measurement method having its own benefits (Section 5.4). Pulse shape discrimination was used to separate gamma and neutron events occurring in the detector. This was particularly of use when using nuclear reactions at an accelerator as a source of neutrons, due to large beam-induced backgrounds. Birk's law [98] was fit to the light response of PEN and the Birk's factor and scintillation efficiency were determined to be $kB = 0.12 \pm 0.01$ mm MeV^{-1} and $S = 1.31 \pm 0.09$ MeVee MeV^{-1} respectively. With these parameters determined, it is now possible to evaluate PEN for low-background and ton-scale applications and to determine its viability in vetoing background events.

Finally, the post-Gerda test (PGT) provided a testing environment to understand how the use of PEN baseplates impacted the detectors. This LEGEND R&D effort included ∼40 kg of HPGe detectors in the Gerda geometry. Approximately 40% of the detectors were mounted with PEN baseplates and the rest were mounted with silicon baseplates. The PEN baseplates used in the PGT were machined at UTK in an effort led by myself. The aim was to try and minimize exposure to contamination while still producing components that met the tolerances demanded by the experiment. This geometry was then simulated using the LEGEND simulation framework, MaGe. These simulations produced an optical map, describing the probability of photons produced in the LAr and PEN baseplate to reach the SiPMs. For three photon sensitivity, the energy threshold for events inside the PEN baseplates is $E_{min} \sim 0.3$ MeV. Once contamination of ^{232}Th in the PEN baseplates was simulated, GAT was used to produce simulated spectra for the ^{76}Ge detectors (Fig. 6.11, 6.12, 6.13). This package allows for the application of cuts that are similar to those used in the experimental data. This simulated data were compared to Run0030 at the PGT, which looked at backgrounds in the experiment and baseline stability over 27 days (Fig. 6.15, 6.16, 6.17). Two cuts were applied to both the experimental and simulated data; an AC cut which removes events that were seen in multiple ^{76}Ge detectors and a PSD cut, which looks to remove multi-site events or events that did not occur in the bulk of the material. The rate of ^{208}Tl decay ($E_\gamma = 2.614$ keV) was calculated in both the simulated

and experimental data for the series of cuts as a method of measuring ^{232}Th contamination. Limits of ^{232}Th contamination were set to be $\sim$ 10 ppb for the PEN baseplates (Table 6.2), significantly above previously measured limits (Section 4). However, it is expected that there will be an increased sensitivity in LEGEND-200, where the mass will increase 27 times and the run time will increase 68 times. The increased photo-electron veto efficiency was estimated in a different simulation looking at how background rates around $Q_{\beta\beta}$ change with different cuts. In Table 6.3, there is a decrease outside uncertainty from detector S4.2 to S4.4. When considering the percentage reduction of background, the veto cut removes 84.1% of events from detector S4.2 and 88.9% of events from detector S4.4.

In conclusion, PEN provides a convenient, commercially available, and structurally stable active structural material that has the potential to have a strong impact on low background and other large physics experiments. This dissertation provides an extensive characterization of the PEN material, including its optical and luminescent properties. These properties were then used to understand the impact of this material in the LEGEND R&D effort, the PGT. Data from the PGT were analyzed to set upper limits on ^{232}Th contamination in the PEN baseplates and used to predict how the veto efficiency could be improved using this material. With this dissertation, there has been a framework for understanding how structural active novel materials can impact the sensitivity of the detector to new physics and how to best characterize the material to understand its impact.

Bibliography

[1] E. Aprile et al. (XENON), Phys. Rev. Lett. **119**, 181301 (2017), 1705.06655. 1, 4

[2] E. Aprile, J. Aalbers, F. Agostini, M. Alfonsi, L. Althueser, F. Amaro, S. Andaloro, E. Angelino, J. Angevaare, V. Antochi, et al., Physical Review D **103** (2021), ISSN 2470-0029, URL http://dx.doi.org/10.1103/PhysRevD.103.063028. 1

[3] Nature **568**, 532âĂŞ535 (2019), ISSN 1476-4687, URL http://dx.doi.org/10.1038/s41586-019-1124-4. 1

[4] N. Di Marco (GERDA), Nucl. Instrum. Meth. A **958**, 162112 (2020). 2, 4

[5] W. R. Leo, *Techniques for nuclear and particle physics experiments* (Springer, 1994). 2

[6] Q. R. Ahmad et al. (SNO), Phys. Rev. Lett. **89**, 011301 (2002), nucl-ex/0204008. 2, 8

[7] S. Obara, Nuclear Instruments and Methods in Physics Research Section A: Accelerators, Spectrometers, Detectors and Associated Equipment **845**, 410 (2017), ISSN 0168-9002, proceedings of the Vienna Conference on Instrumentation 2016, URL http://www.sciencedirect.com/science/article/pii/S0168900216306015. 2, 44

[8] B. Abi et al. (DUNE) (2018), 1807.10334. 2, 45

[9] M. J. Dolinski, A. W. Poon, and W. Rodejohann, Ann. Rev. Nucl. Part. Sci. **69**, 219 (2019), 1902.04097. 2, 20, 22, 27

[10] M. Auger et al. (EXO-200), Phys. Rev. Lett. **109**, 032505 (2012), 1205.5608. 4

[11] N. Abgrall et al. (LEGEND) (2021), 2107.11462. 3, 8, 30, 34, 35, 37, 45, 55

[12] S. Abe et al. (KamLAND-Zen) (2022), 2203.02139. 4

[13] P. Morrison, Scientific America **207**, 90 (1962). 6

[14] S. A. Watkins, American Journal of Physics **51**, 551 (1983), https://doi.org/10.1119/1.13201, URL https://doi.org/10.1119/1.13201. 6

[15] C. L. Cowan, F. Reines, F. B. Harrison, H. W. Kruse, and A. D. McGuire, Science **124**, 103 (1956), https://www.science.org/doi/pdf/10.1126/science.124.3212.103, URL https://www.science.org/doi/abs/10.1126/science.124.3212.103. 7

[16] G. Danby, J. M. Gaillard, K. A. Goulianos, L. M. Lederman, N. B. Mistry, M. Schwartz, and J. Steinberger, Phys. Rev. Lett. **9**, 36 (1962). 7

[17] K. Kodama et al. (DONUT), Phys. Lett. B **504**, 218 (2001), hep-ex/0012035. 7

[18] K. Krane, *Modern Physics, 3rd Edition* (Wiley, 2012), ISBN 9781118210093, URL https://books.google.com/books?id=3tobAAAAQBAJ. 8

[19] J. N. Bahcall and R. Davis, Science **191**, 264 (1976), https://www.science.org/doi/pdf/10.1126/science.191.4224.264, URL https://www.science.org/doi/abs/10.1126/science.191.4224.264. 8

[20] Y. Fukuda et al. (Super-Kamiokande), Phys. Rev. Lett. **81**, 1562 (1998), hep-ex/9807003. 8

[21] F. Suekane, *Neutrino Oscillations A Practical Guide to Basics and Applications*, Lecture Notes in Physics, 898 (Springer Japan, Tokyo, 2015), ISBN 9784431554622. 8, 10, 11, 13

[22] Z. Maki, M. Nakagawa, and S. Sakata, Prog. Theor. Phys. **28**, 870 (1962). 10

[23] B. Pontecorvo, Zh. Eksp. Teor. Fiz. **53**, 1717 (1967). 10

[24] D. of Energy, *Doe explains...The standard model of particle physics*, URL https://www.energy.gov/science/doe-explainsthe-standard-model-particle-physics. 9

[25] M. C. Gonzalez-Garcia, M. Maltoni, and T. Schwetz, Universe **7**, 459 (2021), 2111.03086. 10, 11

[26] NuFit, *NuFIT*, URL http://www.nu-fit.org/. 11

[27] S. AdriÃąn-MartÃŋnez, M. Ageron, F. Aharonian, S. Aiello, A. Albert, F. Ameli, E. Anassontzis, M. AndrÃľ, G. Androulakis, M. Anghinolfi, et al., Journal of Physics G: Nuclear and Particle Physics **43** (2016). 11

[28] P. F. de Salas, D. V. Forero, C. A. Ternes, M. Tortola, and J. W. F. Valle, Phys. Lett. B **782**, 633 (2018), 1708.01186. 11

[29] C. Rolfs, W. Rodney, and W. Rodney, *Cauldrons in the Cosmos: Nuclear Astrophysics*, Theoretical Astrophysics (University of Chicago Press, 1988), ISBN 9780226724577, URL https://books.google.com/books?id=BHKLFPUS1RcC. 13, 14

[30] N. Aghanim et al. (Planck), Astron. Astrophys. **641**, A6 (2020), [Erratum: Astron.Astrophys. 652, C4 (2021)], 1807.06209. 13

[31] W. Hu, D. J. Eisenstein, and M. Tegmark, Phys. Rev. Lett. **80**, 5255 (1998), astro-ph/9712057. 13

[32] J. Lesgourgues, *Neutrino Cosmology*. (Cambridge University Press, Cambridge, 2013), ISBN 9781139612142. 13, 14, 15, 16

[33] T. K. C. Aker, M. et. al., Nature Physics **18**, 160 (2022), ISSN 1745-2481, URL https://doi.org/10.1038/s41567-021-01463-1. 13, 14

[34] S. Mertens, J. Phys. Conf. Ser. **718**, 022013 (2016), 1605.01579. 14

[35] K. Harigaya, M. Ibe, and T. T. Yanagida, Phys. Rev. D **86**, 013002 (2012), URL https://link.aps.org/doi/10.1103/PhysRevD.86.013002. 16

[36] E. MA, Modern Physics Letters A **24**, 2161âĂŞ2165 (2009), ISSN 1793-6632, URL http://dx.doi.org/10.1142/S0217732309031776. 16

[37] S. Dimopoulos and H. Georgi, Nucl. Phys. B **193**, 150 (1981). 16

[38] S. Davidson, E. Nardi, and Y. Nir, Phys. Rept. **466**, 105 (2008), 0802.2962. 17

[39] S. Y. Khlebnikov and M. E. Shaposhnikov, Nucl. Phys. B **308**, 885 (1988). 17

[40] K. Krane, *Introductory Nuclear Physics* (Wiley, 1987), ISBN 9780471805533, URL https://books.google.com/books?id=ConwAAAAMAAJ. 17, 19

[41] A. Giuliani and A. Poves, Adv. High Energy Phys. **2012**, 857016 (2012). 18

[42] R. Arnold et al. (NEMO-3), Phys. Rev. D **93**, 112008 (2016), 1604.01710. 18

[43] R. Mohapatra et al., Rept. Prog. Phys. **70**, 1757 (2007), hep-ph/0510213. 20

[44] J. Kotila and F. Iachello, Phys. Rev. C **85**, 034316 (2012), URL https://link.aps.org/doi/10.1103/PhysRevC.85.034316. 20, 22

[45] F. T. Avignone, III, S. R. Elliott, and J. Engel, Rev. Mod. Phys. **80**, 481 (2008), 0708.1033. 21

[46] W. Maneschg, *Present status of neutrinoless double beta decay searches* (2017), 1704.08537. 22

[47] M. Agostini, G. Benato, and J. Detwiler, Phys. Rev. **D96**, 053001 (2017), 1705.02996. 22, 25, 26

[48] R. Henning, Reviews in Physics **1**, 29 (2016), ISSN 2405-4283, URL http://www.sciencedirect.com/science/article/pii/S2405428316000034. 23, 25, 27

[49] B. Bucher et al., Phys. Rev. Lett. **118**, 152504 (2017), 1703.05268. 27

[50] D. Rudolph et al., Phys. Rev. Lett. **82**, 3763 (1999). 27

[51] J. Timár et al., Phys. Lett. B **598**, 178 (2004). 27

[52] Z.-F. Lu, Y.-L. Li, J. Li, Q. Yue, and Y.-J. Li, Chin. Phys. C **36** (2012). 28

[53] N. Abgrall et al. (Majorana), Phys. Rev. Lett. **118**, 161801 (2017), 1612.00886. 28, 37

[54] *The majorana experiment*, URL https://www.npl.washington.edu/majorana/majorana-experiment. 29

[55] Proposal LNGS-P 58/18 (2018), URL http://pessina.mib.infn.it/Biblio/Biblio_Articoli/20180319Legend-200_proposal_submitted.pdf. 30

[56] V. D'Andrea (GERDA), EPJ Web Conf. **225**, 01006 (2020). 32

[57] P. Agnes et al. (DarkSide), Phys. Rev. D **93**, 081101 (2016), [Addendum: Phys.Rev.D 95, 069901 (2017)], 1510.00702. 38, 39

[58] K. Pelczar, Ph.D. thesis, Jagiellonian U. (main) (2016). 39

[59] Ji and L. Na, *Study on Preparation Process and Properties of Polyethylene Terephthalate (PET)* (2013), URL https://www.scientific.net/AMM.312.406. 42, 44

[60] *2019 preferred fiber and materials report*, URL https://store.textileexchange.org/product/2019-preferred-fiber-materials-report/. 44

[61] Y. Efremenko et al., JINST **14**, P07006 (2019), 1901.03579. 44, 45, 46, 47, 71, 72, 88

[62] C. Cuesta (DUNE), in *2019 European Physical Society Conference on High Energy Physics* (2019), 1910.10115. 44, 45

[63] E. Tiras, J. Wetzel, B. Bilki, D. Winn, and Y. Onel, Proceedings of 38th International Conference on High Energy Physics âĂŤ PoS(ICHEP2016) (2017). 44

[64] H. Nakamura, Y. Shirakawa, S. Takahashi, and H. Shimizu, EPL (Europhysics Letters) **95**, 22001 (2011), URL http://stacks.iop.org/0295-5075/95/i=2/a=22001. 44

[65] M. Sonnenschein and C. Roland, Polymer **31**, 2023âĂŞ2026 (1989). 44

[66] E. V. Anslyn and D. A. Dougherty, *Modern physical organic chemistry* (Univ. Science Books, 2008). 45

[67] Y. Efremenko et al., JINST **17**, P01010 (2022), 2110.12791. 49, 51, 80, 117

[68] M. Laubenstein, Int. J. Mod. Phys. A **32**, 1743002 (2017). 51

[69] V. B. Brudanin et al., JINST **12**, P02004 (2017). 51

[70] M. Wojcik and G. Zuzel, AIP Conference Proceedings **897** (2007), ISSN 0094-243X, URL https://www.osti.gov/biblio/21055025. 55

[71] K. L. V. B. R. D. Mary Therese Jernigan, Rodney Scott Armentrout, *Aluminum containing polyester polymers having low acetaldehyde generation rates* (European Patent 1924628A2, September 2006). 55

[72] R. S. Tipson, Analytical Chemistry **22**, 628 (1950), https://doi.org/10.1021/ac60041a002, URL https://doi.org/10.1021/ac60041a002. 57

[73] J. Scheirs and T. E. Long, *Modern polyesters: chemistry and technology of polyesters and copolyesters* (John Wiley and Sons, 2006). 58, 70

[74] N. N. D. Center, *Decay radiation for isotopes* (2013), URL https://www.nndc.bnl.gov/nudat2/. 58

[75] W.-D. G. B. H. E. H. Wolfgang Schmidt, Ulrich Thiele, *Titanium-containing catalyst and process for the production of polyester* (U.S. Patent 5656716A, Aug. 1997). 58

[76] B. Duh, Polymer **43**, 3147 (2002), ISSN 0032-3861, URL http://www.sciencedirect.com/science/article/pii/S0032386102001386. 58

[77] J. Yang, Z. Xia, F. Kong, and X. Ma, Polymer Degradation and Stability **95**, 53 (2010), ISSN 0141-3910, URL http://www.sciencedirect.com/science/article/pii/S0141391009003346. 58

[78] *Spectral database*, URL https://spectrabase.com/spectrum/2rK7An975MD. 59

[79] U. K. Thiele, International Journal of Polymeric Materials and Polymeric Biomaterials **50**, 387 (2001), https://doi.org/10.1080/00914030108035115, URL https://doi.org/10.1080/00914030108035115. 59

[80] S. M. Aharoni, International Journal of Polymeric Materials **48**, 425âĂŞ445 (2006). 59

[81] S. R. Turner, Journal of Polymer Science Part A: Polymer Chemistry **42**, 5847âĂŞ5852 (2004). 59, 66

[82] K. Jordan, D. Springfels, and D. Schubring, Nuclear Engineering and Design **286**, 89 (2015), ISSN 0029-5493, URL http://www.sciencedirect.com/science/article/pii/S0029549315000606. 66

[83] C.-A. Christofferson, personal communication. 68, 83

[84] Y. C. K. I. S. C. Y. J. H. Hyun Nam Cho, Jae Min Hong, *Process for preparing polyethylene naphthalate based polymers* (U.S. Patent 6040417A, Feb. 1999). 69

[85] R. Bilstein, *Stages to Saturn: a technological history of the Apollo/Saturn launch vehicles* (National Aeronautics and Space Administration, NASA History Office, 1996). 70

[86] O. Yano and H. Yamaoka, Progress in Polymer Science **20**, 585 (1995), ISSN 0079-6700, URL http://www.sciencedirect.com/science/article/pii/007967009500003X. 70

[87] C. Lechat, A. R. Bunsell, and P. Davies, Journal of Materials Science **46**, 528âĂŞ533 (2010). 71

[88] J. M. Stearne and I. M. Ward, Journal of Materials Science **4**, 1088âĂŞ1096 (1969). 71

[89] I. O. for Standardization, *Plastics âĂŤ determination of flexural properties*, iSO 178:2010 (2013). 71

[90] (2022), URL https://www.treborintl.com/properties-for-molded-ptfe/. 72

[91] (2022), URL http://www.memsnet.org/material/coppercubulk/. 72

[92] N. R. Overman, C. T. Overman, T. A. Kafentzis, D. J. Edwards, and E. W. Hoppe (2012), URL https://www.osti.gov/biblio/1039850. 72

[93] M. Janecek and W. W. Moses, IEEE Transactions on Nuclear Science **57**, 964 (2010). 73

[94] S. Agostinelli, J. Allison, K. Amako, J. Apostolakis, H. Araujo, P. Arce, M. Asai, D. Axen, S. Banerjee, G. Barrand, et al., Nuclear Instruments and Methods in Physics Research Section A: Accelerators, Spectrometers, Detectors and Associated Equipment **506**, 250 (2003), ISSN 0168-9002, URL https://www.sciencedirect.com/science/article/pii/S0168900203013688. 77

[95] L. Manzanillas, Y. Efremenko, M. Febbraro, F. Fischer, M. G. Corominas, B. Hackett, A. Leonhardt, B. Majorovits, and O. Schulz (2022), 2204.13747. 80

[96] B. Hackett et al. (2022), 2204.02866. 85

[97] H. Nakamura, Y. Shirakawa, H. Kitamura, N. Sato, and S. Takahashi, Nuclear Instruments and Methods in Physics Research Section A: Accelerators, Spectrometers, Detectors and Associated Equipment **739**, 6 (2014). 85

[98] L. Reichhart, D. Akimov, H. M. Araújo, E. J. Barnes, V. A. Belov, A. A. Burenkov, V. Chepel, A. Currie, L. DeViveiros, B. Edwards, et al., Phys. Rev. C **85**, 065801 (2012), URL https://link.aps.org/doi/10.1103/PhysRevC.85.065801. 85, 133

[99] *Hamamatsu photomultiplier tubes and related products*, [Online; accessed 27-March-2021], URL https://www.hamamatsu.com/resources/pdf/etd/PMT_TPMZ0002E.pdf. 88

[100] L. G. Chiang (2001), URL https://www.osti.gov/biblio/814361. 93, 94

[101] *Caen digitizer whitepaper - tools for discovery* (2020), URL https://www.caen.it/caen-digitizer-whitepaper/. 93, 95

[102] D. L. Chichester, J. T. Johnson, and E. H. Seabury (2010), ISSN 0094-243X, URL https://www.osti.gov/biblio/991879. 97

[103] V. Verbinski, W. Burrus, T. Love, W. Zobel, N. Hill, and R. Textor, Nuclear Instruments and Methods **65**, 8 (1968), ISSN 0029-554X, URL https://www.sciencedirect.com/science/article/pii/0029554X68900037. 102

[104] M. Agostini et al. (GERDA), Eur. Phys. J. C **75**, 39 (2015), 1410.0853. 107

[105] A. Domula, M. Hult, Y. Kermaidic, G. Marissens, B. Schwingenheuer, T. Wester, and K. Zuber, Nucl. Instrum. Meth. A **891**, 60585 (2018), 1711.01433. 107

[106] F. Edzards, L. Hauertmann, I. Abt, C. Gooch, B. Lehnert, X. Liu, S. Mertens, D. C. Radford, O. Schulz, and M. Willers, Particles **4**, 489 (2021), 2105.14487. 107

[107] M. Agostini et al., Eur. Phys. J. C **73**, 2583 (2013), 1307.2610. 107

[108] J. Heideman, Ph.D. thesis (2021). 110

[109] M. Boswell et al., IEEE Trans. Nucl. Sci. **58**, 1212 (2011), 1011.3827. 114

[110] C. Poole, I. Cornelius, J. Trapp, and C. Langton, IEEE Transactions on Nuclear Science **99**, 1 (2012). 115

[111] F. Edzards, Ph.D. thesis (2021), URL http://mediatum.ub.tum.de/doc/1609363/1609363.pdf. 120, 123, 125, 126

[112] F. Piastra, Ph.D. thesis, Zurich, U. (2017). 127

Appendix

A Details of PEN Machining for PGT

PEN tiles were machined from large plates produced in July production run. The PEN plates that were used are listed as follows: Tile 68 Produced at 3:50 LEGEND geometry, small optical defect due to bubble, plate touched CNC; Tile 81 Produced at 4:16 LEGEND geometry, plate not milled, CNC running 7/19/2019; Tile 89 Produced at 14:35 Oblex 25 mm geometry, edge of tile touched. PEN tiles were machined at the University of Tennessee Machine shop, using a Fryer toolroom mill CNC machine. The tiles were handled in a way to mitigate risk of contamination. Each tool and piece of equipment was cleaned and the rinse water conductivity was recorded. CNC machine was cleaned with ethanol and electronics cleaner. Nitrogen gas boil-off was blown onto the tile during machining. The machinist wore cleanroom Class 100 gloves, face mask and hairnet during machining. Both end mills and mill drills were used. Machining Procedure: Aluminum plate was bolted onto the CNC table Acrylic plates with protective paper backing was bolted onto table and machined Acrylic plates were cleaned for 24 hours Clean acrylic plates and PEN plates were bolted/sandwiched together in a laminar flow hood inside a clean room (at UTK) and transfered to the machine shop in a clean container Sandwiched plates were bolted to CNC table and holes were drilled into acrylic and PEN plate Clean stainless steel screws were bolted into sandwiched plates CNC milled out in the following order: Drill holes Mill outside of tiles Mill pockets and pocket holes Mill reduced mass regions Sandwiched plates are removed from table and placed back into clean packaging Bolted assembly was disassembled in a laminar flow hood inside a clean room at UTK and PEN tiles were handled by the edges wit ha cleaned hemostat Nitrogen boil off gas was then used to clean off PEN plates PEN tiles were then sealed in a class-100 clean bag Tiles were labelled with the following procedure: Design Num. - PEN Plate Num. - CNC Machined Num. CNC machined number gives the approximate location of where the plate was on the CNC table during machining PEN tiles were shipped in a clean plastic container covered with a thick black cloth and sent express shipping Jan 31, arriving in Germany Feb 3

Vita

Brennan Hackett was born in Plattsburgh, NY on January 16, 1994. She attended school in Austin and Dallas, Texas, until she moved to London, UK in 2007. While finishing her high school education in London, Brennan spent one year living in Changzhou, China as part of the NSLI-Y State Department fellowship. In 2013, She began her Bachelors of Science in Physics at the University of Surrey. Though it was not initially her intention, she switched to the Masters of Physics program and received a research position at Oak Ridge National Laboratory in 2016. During that time, she developed a detector array and measured background radiation temporal and spatial fields at the High Flux Isotope Reactor for the PROSPECT collaboration. After completing her Masters degree, she returned to Tennessee to pursue a PhD at the University of Tennessee at Knoxville. She worked with her academic advisor, Yuri Efremenko, and her research advisor, Michael Febbraro on developing structural active materials for the low background physics experiment, LEGEND. During her PhD she had the privilege of hosting the Women in Science Social, a DEI effort held at the Division of Nuclear Physics Conference to aid in networking and connection for women and other gender minorities in the nuclear sciences. She completed her dissertation research in the Summer of 2022.

Select publications include; L. Manzanillas et al. (2022), 2204.13747, B. Hackett et al. (2022), 2204.0286679, Y. Efremenko et al., JINST 17, P01010 (2022), 2110.12791, M. Laubenstein et al., Int. J. Mod. Phys. A32, 1743002 (2017), Y. Abraham et al., JINST 16, P07017 (2021), 2103.03232, and J. Ashenfelter et al. (PROSPECT), Phys. Rev. Lett.121, 251802 (2018), 1806.02784.

Select awards include; UTK Physics Department Fowler Marion Award (May 2022), UTK Professional Promise Award (May 2022), and ORNL Safety Award (October 2019).